TECHNISCHE UNIVERSITÄT
BERGAKADEMIE FREIBERG

Die Ressourcenuniversität. Seit 1765.

THERMODYNAMIC PROPERTIES OF INTERMETALLICS

Surfaces and Interfaces

To the Faculty of Chemistry and Physics

of the Technische Universität Bergakademie Freiberg

is submitted this

THESIS

to attain the academic degree of

Doctor rerum naturalium
(Dr. rer. nat.)

submitted

by M.Sc. Lilit Amirkhanyan

born on the 27 October 1980 in Yerevan, Armenia

09599 Freiberg
08 August 2017

To my parents for all their love and unconditionally support and for putting me through the best education possible. I appreciate their sacrifices and I would not have been able to get to this stage without them.

To my lovely daughter, who gave me strength and persistence. Who was tolerant and understanding with a lack of time ...

"Quantum theory provides us with a striking illustration of the fact that we can fully understand a connection though we can only speak of it in images and parables."

- Werner Heisenberg

Classical thermodynamics ... is the only physical theory of universal content which I am convinced ... will never be overthrown.

- Albert Einstein

Quoted in Albert Einstein and Stephen Hawking (ed.), A Stubbornly Persistent Illusion (2007), 353.

“The best thing for being sad”, replied Merlyn... “is to learn something. That is the only thing that never fails. You may grow old and trembling in your anatomies, you may lie awake at night listening to the disorder of your veins, you may miss your only love, you may see the world about you devastated by evil lunatics, or know your honour trampled in the sewers of baser minds. There is only one thing for it then – to LEARN. Learn why the world wags and what wags it. That is the only thing which the mind can never exhaust, never alienate, never be tortured by, never fear or distrust, and never dream of regretting. Learning is the only thing for you. Look what a lot of things there are to learn.”

- Merlyn, advising the young Arthur
From The Once and Future King by T.H. White.

Acknowledgements

Accomplishing a PhD thesis is not an individual experience; rather it takes place in a social context and with the support of several persons, whom I would like to thank sincerely.

First and foremost, I would like to express my sincere gratitude to my advisor Prof. Jens Kortus for giving me the opportunity to complete my PhD at the Institute of Theoretical Physics in Freiberg. I especially want to thank him for the continuous support of my PhD study and related research, for his patience, motivation, and formidable knowledge. His authority helped me at all points of the investigation and brought me to the successful end of my thesis. I could not have had a better advisor and mentor for my PhD study.

I wish to express my sincere thankfulness to the present and gone members of the Institute of Theoretical Physics for their support, whether working or non-working problems received area. The list is too long to name you all, but I thank each of you for welcoming me to your group and sharing your knowledge. I gained a lot from you.

I want to express my special appreciation to the staff of the Collaborative Research Center 920. Everyone was open for discussion at all times, allowing me to dig deeper, and to get a better understanding of upcoming issues in our research project.

Last, but not the least, I would like to thank all my coauthors, for their great corporations and intelligent discussions.

Without your support, this thesis would not have been possible.

Abstract

Currently, in the industry, it is essential to withdraw processes such as oxidation, suffixation, nitridation, carbits, etc. Therefore, remove inclusions in the metal making process and usages are growing. A strengthening steel, which will be as pure as possible is crucial. It was shown that the size, type and distribution of several inclusions in steel develop in the products because of the changes to the mechanical properties fracture.

The aim of making pure stainless steel faces the challenge of lowering non-metallic oxide inclusions and controlling the morphology, composition and size of the distribution. Significant inclusion types are defined as endogenous and exogenous non-metallic inclusions in the steel. Moreover, the process of cleaning a product could be the filtration of the metallic melts, to remove endogenous as well as exogenous inclusions. The filter surface's chemical composition, as well as the technology of filtration, can significantly affect the filtration efficiency.

The primary focus of this work is to reproduce various filter materials without any input from experimental data and investigate the interaction of ceramic inclusions with the filter walls, the surface, and interface energies as a driving force for the acceleration of inclusions. The purpose is to provide a foundation for the improvement of realistic data that can be used for further research.

The central part of the work is the study of the thermodynamic data and phase formation. The study of the thermodynamic of aluminum - based binary and ternary intermetallic phase systems are presented in this dissertation. Various thermodynamic phase descriptions exist based on phase equilibrium data and experimental thermodynamic data for aluminum - based binary and ternary intermetallic phases. Nevertheless, the thermodynamic experimental data for some intermetallic phases are missing and the empirically calculated data, for instance, using the Neumann-Kopp rule does not always give a reasonable result. The change of specific heat capacity as a result of melting will be included in the specific heat capacity curve of the intermetallic compounds, which melt at higher temperatures than pure Al. In addition to that, the phase transformations in Fe will be noted in intermetallics. Accordingly, it is vital to know the specific heat capacity of intermetallic compounds in a wide range

of temperatures, in order to have a reliable estimation of enthalpy functions to a high - temperature range.

Also, the fundamental interactions, possible chemical reactions on the filter surfaces, filter surface and interface surface energies are investigated and presented in this dissertation. The surfaces and the solid state formed interface materials which occur due to the filtration were modelled. For material in contact with a particular environment, it must be substituted by the surface or interface energy. Those energies play a principal role in defining the surface adsorption and wetting. The focus of the investigation is the characterisation of the filter materials and not the dynamics of the filter process.

All calculations were done with density functional theory (DFT) as implemented in the Quantum Espresso code, which is an approximate solution of the quantum mechanical Schrödinger equation. The inputs of this method are the systems of electronic structures. Phonon dispersion as a function of the crystal volume within the quasi-harmonic approximation was used to obtain the thermodynamic data.

The method employed for a purpose to achieve the surface energy is dependent on the bulk and vacuum slab modelling, and the calculation was implemented with DFT.

Table of contents

List of figures

List of tables

Chapter 1

Introduction

Nowadays, the interest in removing inclusions in metal making and usages are growing. In the industry, it is certainly important to avoid processes such as oxidation, suffixation, nitridation, carbits, etc. According to the literature, around 90% of fracture accidents are caused by fatigue. Therefore, it is essential to develop steel that is as pure as possible. It is known that the size, type and dissemination of different inclusions in the metal expand equipment of the mechanical properties of the cast products [20]. To achieve these goals a solid knowledge and understanding the mechanism of inclusion, the formation is essential. The goal of cleaner steel faces the challenge of lowering non-metallic oxide inclusions and controlling the morphology, composition and size of the distribution. Accordingly, there is not a single method to measure all of these characteristics accurately. The disagreement between Young's modulus and the thermal expansion of nonmetallic inclusions with the steel matrix develops the internal stresses, which lower the existing interfacial strength between inclusion and matrix [21]. At the same time, the discrepancy of deformation between nonmetallic inclusions and the matrix results in local elasticity, where fatigue cracks can be developed at the loading sites. According to Shenoy at al.[22] when a sufficient driving force is reached, propagation of these fatigue cracks results in component failure. Therefore, the implementation of ceramic foam filters has been considered since the 1970s [23, 24]. In solid iron or steel, the solubility of oxygen is essentially zero with increasing purity and lattice perfection of the metal [25]. Accordingly, any dissolved oxygen in liquid steel would be accelerated out as FeO inclusions during solidification if the steel is not deoxidised. Moreover, earlier in 1985 by Gauckler et al. [26] published their work "Industrial application of open pore ceramic foam for molten filtration" on laboratory experiments showing the relationship between the filter matrix structural characteristics, filtration parameters and filter efficiency. They also discussed numerous methods for filtering impure metal melts. It is

already accepted that there are several reasons for touch particles to adhere to the macroscopic surface of the filter.

For example:

Direct interception - when a particle hits the filter surface following its trajectory line.

Gravity forces - when a particle with a different density in the fluid leaves the trajectory line and starts to flow by gravity forces.

Attractive force - when a particle during flow can be attracted to the filter surface and could be retained. It is the attraction caused the surface energy of the filter surface.

Brownian movement - when a particle due to its random Brownian movement or caused by bombardment from the particles in the liquid, can leave the fluid and hits the internal filter surface.

Inertial force - when a particle because of by sudden changes of the trajectory line of liquid, continues its move inertia and hits the internal filter surface.

Hydrodynamic effects - as a result of a distribution of different velocities in the fluid within the filter, a particle's shape and its rotation play a role, which can also bring a particle to the point where it sticks to the internal filter surface.

In the case of aluminium filtration via ceramic foam, direct interception, internal and hydrodynamic forces are essential [26]. Therefore, it is advantageous to merge various methods together to quantify steel cleanliness in a given application [27]. Significant inclusion types are defined as endogenous[1] and exogenous[2] non-metallic inclusions in the steel. Besides, the method of cleanliness product could be the filtration of the metallic melts, to remove endogenous as well as exogenous inclusions [28]. Strangely enough, the size of the inclusion is in the order of several tens of micrometres, and they could be filtered effectively using ceramic foam filters with pores in the millimetres [29]. The endogenous inclusions are consistent with their sources, are produced during cooling and solidification of steel [30]. Is already well known for many years, that the ceramic foam filters used in metal casting application can achieve highly pure casting by removing roughly 25% of the particles within the size range of 1-100μm [31]. However, using different filter materials instead of changing the wall chemistry, such as using the active or reactive coated based filters, will lead to a higher deposition on the filter surface in addition to the filtration processes. It was found that the most common inclusions in the melt are oxides like Al_2O_3, MgO, $MgAl_2O_4$, and SiO_2 [32, 33], as well as Al_4C_3 in the aluminium based matrix [34]. Open cell ceramic filters are applicable for curtailing non-metallic inclusions in the casting of metals, which increases

[1]The inclusions, which occur in the melting and solidification process, due to the chemical reactions.
[2]The inclusions, which occur due to the contact between steel melt and furnace walls

the quality of cast parts. Subsequently, it was seen that the most non-metallic inclusions were found in the casted filters Al_2O_3 + Al_2O_3 and Al_2O_3 + spinel [35].

Interestingly, such micrometer-scale particles can be filtered from the melt using rather wide-mesh (mm) foam filters of similar materials, generally corundum. A similar process known from the metal casting called clogging, and it happens when particles in the melt deposit layers on the walls of a tundish nozzle [36]. The filters are used once for a casting time of ca. one minute.

As was already mentioned, the filter surface's chemical composition, as well as the technology of filtration, can significantly affect the filtration efficiency. The mechanisms of filtration are screen filtration, cake filtration, depth filtration and flowing in a foam filter. The effectiveness of depth filtration for molten melt was investigated by Mutharasan et. al.[37], whereby the filtration efficiency was shown to be exponentially dependent on the filter depth. Furthermore, reactive filter materials are proposed to react with the dissolved gases in the metal melt, for reducing gas impurities, as well as nonmetallic inclusions, which arise below the liquidus temperature. For the case of filter surfaces, based on active ceramic coatings, the deposition of nonmetallic inclusions on the filter is supposed to be improved considerably.

An amount of oxidic, nonmetallic inclusions also occur. Their type, shape and distribution have the greatest impact on the material properties in applications such as high-strength steels. They govern the deformation and fracture, as well as changes to the physical properties of the steel. Due to the load, stress concentrations can stem from the presence of inclusions. The categorisation of these inclusions has many varieties. As it was mentioned above, the exogenous inclusions may get into the melt e.g. due to the erosion of refractory materials amid the steel making processes. This inclusion type withstands only an insignificant part of the collectivity of inclusions. Nevertheless, endogenous inclusions are of relative importance, and they are themselves characterised by their time of origin:

Primary inclusions - formed forthwith beyond the addition of deoxidizers, moreover, the process continues, as far as the balance of deoxidation at a constant temperature is fulfilled. These reactions occur in the liquid steel, through which the inclusions most possibly accumulate ahead of the melt solidification.

A characterisation of the differently observed inclusions in aluminium deoxidised iron has been considered by Wasai et al. [20], whereby they attached the name *primary inclusions* to the group of inclusions, which are the dendritic, maple-like and polygonal.

Secondary inclusions - formed by the cooling down liquidus temperature, they are dependent on the temperature of the deoxidation reaction. These inclusion types can be barely split due to their small size into the viscose steel melt.

Secondary inclusions can be network-like, coral-like or spherical inclusions, i.e. alumina, hercynite and wustite. Besides, as secondary inclusions are observed - alumina, α-, γ-, and δ- structures, and amorphous silica inclusions. Some nonmetallic inclusions, exclusively secondary inclusions, maintain a positive influence on the steel due to their effect as grain-growth inhibitors, resulting in fine-grained steel [38].

Tertiary inclusions - formed during the cooling-down process, the oxygen decreases, and the melt progressed from the liquid to the solid state of the steel. A consequence, the solubility of the deoxidizers is enriched leading to possible new inclusions.

Quaternary inclusions - formed together with the solidified steel, which is noticeable ahead the decreasing solubility. These types of inclusions are generated during solid-state phase transformation.

The classification of the growth of inclusions follows by some order, for example *secondary inclusions* mainly grow on top of *primary inclusions*, and a *tertiary inclusion* can grow on the *secondary inclusions*. Thereby, it is hard to specify the fine *secondary inclusions* and *tertiary inclusions* [39].

According to their chemical composition, the oxidic, nonmetallic inclusions can be classified into:

- *Corundum-type*: familiar notation is Me_2O_3(e.g. Al_2O_3). This category is specifically relevance, since Al is the most common deoxidizer
- *Iron oxide-type*: note that commonly iron is partially substituted by manganese (FeO, MnO, [Fe,MnO])
- *Spinel-type*: accepted notation is $MeO{\cdot}Me_2O_3$ (generally $MgO{\cdot}Al_2O_3$, $FeO{\cdot}Al_2O_3$, $MnO{\cdot}Al_2O_3$)
- *Silicate-type*: due to the change in the ratio of oxides this kind does not have a general notation. Archetypes are: $3Al_2O_3{\cdot}2SiO_2$, $MnO{\cdot}SiO_2$, $2FeO{\cdot}SiO_2$

Referring to the point that it is hard to specify the inclusions, there is also another relevant way to analyse and categorise the oxidise, nonmetallic inclusions. In this instance, the discrimination of the particles references their specific morphology. These consist of small (0 - 5μm) or large (2 - 6μm) spherical inclusions, octahedral (2 - 4μm), small (smaller then 5μm) and large (larger then 5μm) faceted inclusions, hexagonal or trigonal (2 - 9μm) platelike inclusions, generally in a trigonal manner, dendrite consisting of pure aluminium oxide (5 - 20μm), where clusters form an open network of aluminium oxides (over 100μm), and aggregates which are faceted particles(up to a few tens of micrometers) [40].

As shown, the size of the inclusions are defined, which are taken to indicate the present inclusion type:

1. macroscopic inclusion (> 20μm - mainly exogenous inclusions or clusters of small inclusions)
2. microscopic inclusions (1-20μm - primary, secondary or tertiary inclusions)
3. sub-microscopic inclusions (< 1μm – quaternary inclusions)

As outlined above, the size of the respective inclusions has a direct influence on the fatigue strength of steel. The larger the particles, the more pronounced the fatigue strength reduction. Nevertheless, the influence of the particle is also dependent on their location. Inclusions located at the casting surface demonstrate a much higher destructive potential compared to internal inclusions [41].

Already in 1963, Schwartzwalder et. al.[42] worked on the method of making porous ceramics, whereby a polymer foam is coated with a ceramic slurry to wipe out the defects due to the squeezing process and to get a desirable wall thickness for the foam ceramic filter. An optimal thickness of foam-formed walls is 0.3mm. Currently, the quality of the ceramic foam filters is balanced by spraying coatings. As outlined above, there are "active" and "reactive" coatings. In the event of "active" coating, the same chemistry as the primary and secondary inclusions is used to remove those inclusions. In the other case, when the "reactive" coating is used, the coatings react with the dissolved inclusions in the melt gas for example with oxygen in steel melts. With this case, the small degree of ternary and quarternary inclusions are produced below the liquidus temperature. The "active" coated ceramic filters were presented for improving properties of the cast in iron and aluminium products [43].

For a broad investigation of the different filtration mechanisms, their effect and the impact of various filter coats on the filtration process, the project: Collaborative Research Center 920 (CRC 920) “Multifunctional filters for metal melt filtration - a contribution to zero defect materials” was started at the Technische Universität Bergakademie Freiberg. The aim of the CRC 920 is a contraction of non-metallic inclusions in the metal matrix by the use of filter materials as well as filter surfaces.

The purpose of this dissertation, which was conducted in the framework of the CRC 920, is to reproduce the filter materials without any input from experimental data. Of specific is the interaction of ceramic inclusions with the filter walls, the surface and interface energies as a driving force for endogenous and exogenous particles along within the "active" and "reactive" filter materials. The target is to provide a basis for the improvement of realistic

data that can be used for further investigation. The central part of the work is the study of the thermodynamic data. There are systems of crystalline phases that are still insufficiently characterised experimentally. However, the phase formations in these systems are essential for the description of the casting process of aluminum-based light alloys. The studies of aluminum-based binary and ternary intermetallic phase systems are extremely constrained. Moreover, the phase relations in these systems are complex. In the aluminum-rich alloys, even a small amounts of Fe causes the formation of intermetallic compounds. There is the particular concern to those intermetallic systems grown in consideration of several transitions between the disordered and ordered phases in the Fe-rich side [4, 44]. Various thermodynamic phase descriptions exist based on phase equilibrium data and experimental thermodynamic data. Nevertheless, the thermodynamic experimental data for some intermetallic phases are missing, on the other hand, the empirically calculated data (e.g. specific heat capacity, thermal expansion coefficient), for instance, using the Neumann-Kopp rule [45] does not always give a reasonable result. The significant disadvantage of the Neumann-Kopp approach is that the phase transformations arising in elements will be present in the intermetallic as well. For instance, the change of specific heat capacity as a result of melting will be included in the specific heat capacity curve of intermetallic compounds which melts at essentially higher temperature than pure Al. In addition to that, the phase transformations in Fe will be seen in intermetallics. Accordingly, it is vital to know the specific heat capacity of intermetallic compounds in a wide range of temperatures, to have a reliable estimation of enthalpy functions to a high-temperature range.

The thermodynamical prediction was made based on density functional theory(DFT) as implemented in the Quantum Espresso code [46]. It is the theoretical calculation, which is an approximate solution of the quantum mechanical Schrödinger equation. The atoms and their interactions are considered directly in the simulation. The results are the total interaction energy of the system, the entire electronic structure and information on the chemical bond. The DFT can calculate the complete phonon dispersion for the perfect crystal. Thus phonon dispersion is given as a function of the crystal volume within the quasi-harmonic approximation. From the entropy of the phonons it is possible to calculate the free energy, and the minimisation of the free energy at a fixed volume in yields a relationship between temperature and volume. Furthermore, from the calculated DFT total energy as a function of volume, the pressure can be obtained, so then the Gibbs energy as a function of pressure and temperature can be presented. This then brings the possibility to derive all the thermodynamic quantities. Also, the quantum mechanical forces between the atoms can be calculated. Thus forces can be used for the calculation of the elastic properties of the crystals. As commonly

found with computations, the DFT has its disadvantage. The disadvantage is the limit of the size of the systems due to the high computational cost.

In addition, the fundamental interactions, possible chemical reactions on the filter surfaces, filter surface and interface surface energies can be investigated via DFT. The modelling of surfaces and surface energy calculations with DFT methods is more complicated due to the broken periodicity in one direction. The method used for this purpose was to elongate the crystal structure unit a sufficient number of atomic layer, was achieved, and then added some thickness of vacuum. The constructions of different surfaces with these models were based on the given bulk of the material and its chemical composition. For the surface energy calculation, the main focus of the dissertation is on the Al_2O_3 structure, which is well known as a material with bad wettability by molten steel. Therefore the investigation of its different planes and their different termination can improve the understanding the filtration processes. On the other hands, the charge density investigation of the surface can give an understanding the attraction of the particles, and favourably grows on the surface.

However, the usual meaning of surface energy is a surface within a vacuum. For material in contact with a particular environment, it must be replaced by the interface energy. This energy plays a key role in describing the surface adsorption and wetting. The focus of the investigation is the characterisation of the filter materials and not the dynamics of the filter process. This theoretical work tries to elucidate fundamental interactions and possible chemical reactions at the filter surfaces. This knowledge is crucial for understanding the filter materials and provides the basis for the development of realistic simulations.

The concept of the dissertation is divided into seven chapters:

Chapter 2

Chapter 2 described the theoretical background of the methods which were used during the calculation, namely the Quantum theory within a Hamiltonian operator and the many-body problem which governed the Schrödinger equation. Its approximate solution is given via density functional theory. Furthermore, the quasiharmonic approximation is presented as a tool for the calculation of phonon dispersion as a function of the crystal volume within the quasi-harmonic approximation.

Chapter 3

Since there is a shortage of the experimental specific heat capacity data for binary and ternary phases of Al-based intermetallic systems, in Chapter 3 are presented the investigation of some of those systems. It gives more into the details about the system structures, which are under investigation for thermodynamic data. Such as, the binary η-AlFe system is (Fe_2Al_5)

and the ternary τ_4 compound from the Al–Fe–Si system (Al_3FeSi_2). The purpose is to gain data over a wide temperature range, since it is not always possible to get measured specific heat capacity of the compounds, and the empiric Neumann-Kopp rule does not always give a reasonable result. Also, the data play a significant role in CALPHAD type assessment [47].

Chapter 4

The main substance of ceramic filters is Al_2O_3. In this chapter is a discussion of interface formation between Al_2O_3 based filter and a metal melt. For Al_2O_3 crystal was considered three different phases: α or corundum stable phase and two metastable phases κ and γ of Al_2O_3. Here is shown the selected solid state reactions of corundum with iron which occur at a ceramic filter and metallic melt interface. The enthalpies were calculated as a function of pressure for several compounds in the system Al-O-Fe, which lead to the discussion of the chemical reactions concerning enthalpy differences between starting and resulting compounds. It was shown that in particular a direct reaction is not favoured, but the non-straight path between Al_2O_3 and Fe with the formation of hercynite over reactive FeO is more likely.

Chapter 5

The Al_2O_3 structure is the most highly studied metal oxides, besides, it is the ceramic with a broad range of phase transition and well known as a bad wettability by metal melts due to their ionic character. There are more than 50.000 publications which refer to Al_2O_3, through its different phases and planes surface energies. Nevertheless, there is still uncertainty of its surface and interface energy, considering Al_2O_3 as the primary matrix of the ceramic filters. A solid material's surface is its chemical interaction with the environment. The quantity used to describe the surface characteristics from a thermodynamic point of view is the surface tension or surface energy. Therefore, the study of the Al_2O_3 surface energies on several planes and different terminations would show the interactions at the surfaces based on their charged surfaces for filter materials and inclusions. Additionally, it can yield an understanding of possible chemical reactions on surface and interfaces of ceramic filter material. In this chapter presented the Al_2O_3 surface investigation for several planes within their different terminations. The surface energy is calculated via DFT.

Chapter 6

Since the solidification process occurs in the ceramic filters, the interaction along interface is also investigated. Under of the interest are Al_2O_3 with (0001) plane and Al (111) plane, as well as $MgTiO_3$ (1100) plane with $[1\bar{1}20]$ parallel to TiO_2 $(10\bar{1}0)$ plane and Al_2O_3 $(01\bar{1}2)$ plane with [1010] parallel to TiO_2 (1011) plane with $[01\bar{1}0]$ are also investigated. The

interface slab of each case war created due to the adjustment of particulate bulk structures within 1% misfit offset. The energy differences present the interface energy in particular indication.

Chapter 7

A summary of the dissertation is given in Chapter 7. The main results are highlighted along with a further outlook.

Appendix 1

Appendix 1 holds of all investigated structures the convergence values respect to the most important setting due to the Quantum Espresso [46], for all were obtained the best ratio of accuracy and numerical effort. Given as well the convergence tests for a bulk thicknesses due to the surface energy calculation.

Appendix 2

Given some inputs (Quantum Espresso) of a bulk structures, which have been used for calculations.

Appendix 3

Given some inputs (Quantum Espresso) of surface and interface structures, which have been used for calculations.

Chapter 2

Methods and theoretical background

The Hamiltonian is an operator to the total energy of the system.

In classical theory, it is defined as the sum of the kinetic and potential energies as a function of position and their *conjugate momenta*. Then, the Hamiltonian can be defined as a function of position and momenta and is given by:

$$H(\mathbf{p},\mathbf{r}) = \sum_{i=1}^{N} \frac{\mathbf{p_i}^2}{2m_i} + U(\mathbf{r_1},...,\mathbf{r_N}) \tag{2.1}$$

In classical physics, the Hamiltonian defines canonical variables and equations. The construction of the Hamiltonian formulation for a given classical system can pass to quantum theory. Suffice it to note that quantum evolution in the Heisenberg illustration is from the Hamiltonian equations through replacement of the phase-space variables by corresponding operators. Altogether, the Hamiltonian formulation leads to a self-consistent physical interpretation of a general singular theory, forming the basis for various specific instructions and addresses the quantization of particular theories [48].

The Hamiltonian formalism in the Equation 2.1 contains the Hamiltonian as a function, which maps a pair consisting of a point (q,p) in phase space and a point t in time, to a real number H(q,p,t). Also using the correspondence principle ($E \rightarrow i\hbar\frac{\partial}{\partial t}$ and $p \rightarrow -i\hbar\nabla$) the classical Hamiltonian can be rewritten as:

$$\hat{H} = \hat{T} + \hat{U} = -\frac{\hbar^2}{2}\sum_{i=1}^{N}\frac{1}{m_i}\nabla_i^2 + \sum_{i=1}^{N} U_i \tag{2.2}$$

where the $\hbar$ is the reduced Planck constant ($\hbar = \frac{h}{2\pi}$).

For describing dynamical processes, we should consider time evolution as well. The time evolution is given by the time-dependent Schrödinger equation[49]:

$$i\hbar\frac{\partial \mid \Psi}{\partial t} = H \mid \Psi\rangle \tag{2.3}$$

The solution of the Schrödinger equation is a wave function, which describes the system. In quantum physics the Ψ -wave function is a primary object which has no comprehension object in a classical world. This is an analytical quantity that contains the complete information of a quantum state. Particularly, for encrypting a many-body quantum state, an exponential amount of information is required. A Ψ - wave function characterises the information by a physical many-body system. The Schrödinger equation can neither be obtained nor claimed. The solution of the equation is based on the method of Eigen Values devised by Fourier, where any mathematical function is declared as a sum of an infinite series of other periodic functions. Finding the correct functions, which have the right amplitudes is not trivial.

In order to solve the Schrödinger equation, it requires the N-body or many-body systems problem - the theory of electrons in condensed matter in which one must use statistical concepts to describe the intrinsic properties of materials in the extensive system thermodynamic limit.

2.1 Many-Body Problem

Perhaps the many-body problem can be best defined as the study of the development of the interaction of bodies on the behaviour of the many-body system. Solving the many-body problem needs quantum mechanics since it is an issue which deals fact with very light particles. Generally, all interactions of the particles can be determined by the wave function

$$\Psi(\mathbf{x_1}, \mathbf{x_2}, ...\mathbf{x_N}, t) \tag{2.4}$$

which in turn is governed by Schrödinger equation 2.3, written out for identical particles as [50]:

$$\left\{ -\frac{\hbar^2}{2m}\sum_{i=1}^{N}\nabla_i^2 + \sum_{i>j}V(\mathbf{x_i}-\mathbf{x_j}) + \sum_i U(\mathbf{x_i}) \right\}\Psi = i\hbar\frac{\partial\Psi}{\partial t} \tag{2.5}$$

Where the first sum is kinetic energy, the second and third are the Coulomb interaction potential, where the first term corresponds to the electron-electron interaction and the second

is electron-nucleus interaction. Moreover, for electrons the interrelation should be written as:

$$V(\mathbf{x}) = \frac{e^2}{4\pi\varepsilon_0}\frac{1}{\mathbf{x}} \tag{2.6}$$

which is the Coulomb interaction potential.

The nature of quantum many-body theory resides plays in the conception of the quantum field. The quantum field is a continuous function of position, and like all variables, it is an operator, with strongly fluctuating freedom, and only becomes inevitable at the specific eigenstates [50, 51, 2]. The approach for energy for particles or *quanta* is $E = \hbar\omega$, which is the unique distinction between quantum and classical fields.

A. Einstein did this bright start in 1905, which at first showed that Planck's theory of black-body radiation could be represented regarding photons and generalised the idea of the vibrations inside matter, which now we call *phonons*. The introduction of the photons gave the potential to understand unexplained characteristics of the photoelectric effect. In 1924, Compton showed that the wavelength of an X-ray increases due to the scattering an atom electron. This effect is well explained by the idea that the scattering process is a photon-electron collision in which energy and momentum are conserved. With all this, one can come to a conclusion: an electromagnetic wave interaction with a substance occurs via *elementary indivisible processes*, in which the radiation gives the impression of particles or photons. An accomplishment of the quantum physics, in 1925, was an interpretation of the Pauli exclusion principle of the periodic table of elements [52]. In 1926, Heisenberg [53] and Dirac [54] independently pointed out that non-interacting particles can be written by the wave function, which satisfies Schrödinger's differential equation and governs the dynamics of the system in time. Moreover, the operator which describes the total energy of the quantum system is the Hamiltonian of the system.

For a free particle the momentum and energy can be written as: $p = \hbar k$, $E = \hbar\omega$. The quantum state of a particle is characterised by a wavefunction $\Psi(\mathbf{r},t)$. The result found must be a set of Eigen results. The important fact to remember is that time is simply a parameter in quantum mechanics, not an operator. Accordingly, in quantum physics, each state of a physical system is caused by only one variable, namely the wavefunction $\Psi(\mathbf{r},t)$ which is a function of the *two* variables position and time.

One of the fundamental things about an atomic system is to know their energy and, more essentially, their energy change due to movement. In the case of N particles of matter, which are given by the Pauli principle and interacting via the Coulomb interaction potential. It can be seen that the basic variable of the system would get *3N* degrees of freedom through three coordinates x, y, and z reasonably. Therefore, the solution of a problem is instantly

associated with the system. If there are N particles in the system, then it should be handled as an issue of N+ZN electromagnetically interacted particles.

Earlier in 1930, Dirac [55] wrote that the "density function", which is the one-particle reduced density matrix, altogether concludes the entire state of the particle in a way that matrices satisfy all the conditions of Heisenberg's matrix mechanics.

So the wave function depends only on the electronic coordinates. For a single electron, which is moving in a potential $v(\mathbf{r})$, the wave function from Schrödinger's equation obeys:

$$\left[-\frac{\hbar^2\nabla^2}{2m}+v(\mathbf{r})\right]\Psi(\mathbf{r})=\varepsilon\Psi(\mathbf{r}) \tag{2.7}$$

so unless there is more than one electron (i.e., one has a many-body problem) Schrödinger's equation becomes:

$$\left[(\sum_{i}^{N}-\frac{\hbar^2\nabla_i^2}{2m}+v(\mathbf{r}_i))+\sum_{i<j}U(\mathbf{r}_i,\mathbf{r}_j)\right]\Psi(\mathbf{r}_1,\mathbf{r}_2,...,\mathbf{r}_N)=E\Psi(\mathbf{r}_1,\mathbf{r}_2,...,\mathbf{r}_N) \tag{2.8}$$

where N is the number of electrons and $\mathrm{U}(\mathrm{r}_i, \mathrm{r}_j)$ is the electron-electron interaction. For a Coulomb system one has:

$$\hat{U}=-\frac{e^2}{4\pi\varepsilon_0}\sum_i\sum_I\frac{Z_I}{\mid\mathbf{r}_i-\mathbf{R}_I\mid}+\frac{e^2}{8\pi\varepsilon_0}\sum_I\sum_{I\neq J}\frac{Z_IZ_J}{\mid\mathbf{R}_I-\mathbf{R}_J\mid}+\frac{e^2}{8\pi\varepsilon_0}\sum_i\sum_{i\neq j}\frac{1}{\mid\mathbf{r}_i-\mathbf{r}_j\mid} \tag{2.9}$$

In the case of an interaction between electrons and nuclei, nucleus and nucleus, as well as electron and electron. The i, and j indices represent an electronic degree of freedom and I and J represent nuclei. In the last two terms, $i=j$ and $I=J$ should be excluded so that electrons and nuclei do not interact with themselves, and therefore the factor $\frac{1}{2}$ in these two terms has been included to avoid double counting.

By the Coulomb interaction, this is the same operator for any system of particles. Accordingly, it is the same for the kinetic energy operator:

$$\hat{T}=-\frac{\hbar^2}{2m}\sum_i\nabla_i^2-\frac{\hbar^2}{2M}\sum_I{\nabla_I}^2 \tag{2.10}$$

It is the same for any nonrelativistic system [56]. Either our system is an atom, a molecule, or a solid thus depends only on the potential $v(\mathbf{r}_i)$.

Following the previous equation, Schrödinger's equation can be written as:

$$\hat{H} = \hat{T} + \hat{U} + \hat{V}_{ext}, \tag{2.11}$$

Where $\hat{T}$ represents the kinetic energy operator, $\hat{U}$ is an electron repulsion potential energy operator, and $\hat{V}_{ext}$ is an external field which is created by the "freeze" nuclei. This approach to Schrödinger's equation can be ordered as an eigenvalue problem, by choosing a $v(\mathbf{r})$ for the system then solving Schrödinger's equation as a wavefunction Ψ. Accordingly, the eigenvalues are energies, and each eigenvalue corresponds to each eigenstate. According to the Rayleigh-Ritz eigenvalue problem [57], it is now possible to minimise the eigenvalues:

$$E_0 = \min_{\Psi \to \Psi_0} \langle \Psi \mid \hat{H} \mid \Psi \rangle \tag{2.12}$$

Every wave function yields an energy. In the case of Ψ_0 the energy is the ground state energy is E_0[1].

The quantitative theories demand approximations for moving forward. The most widely used one is the independent electron approximation. The basis of this approximation is the independent movement of each electron, except that the electrons obey the exclusion principle and each moves in some average effective potential which may be determined by the other electrons. Then the state of the system is specified by independent-particle eigenstates.

A limited amount of quantum entanglement, as well as the typicality of a small number of physical states, are then the blocks on which modern approaches build upon to solve the many-body Schrödinger's equation with a limited amount of classical resources.

2.2 The Hartree and Hartree-Fock Method

To get a suitable method to approach the analytically non-attainable solution of the many-body problem, a very useful tool is the usage of the ground state wave function, which corresponds to the energy of the system.

The Hartree-Fock (HF) or "self-consistent-field" calculation is a model based on independent particles. For N independent particles the wave function is $\Psi(\mathbf{r_1}, \mathbf{r_2}, ..., \mathbf{r_N})$, where $\mathbf{r_i}$ indicate the particle coordinates and spins. The main idea of the Hartree-Fock approach is that the energy obtained by any test wave function is different from the actual ground state function, i.e, it is higher than the actual ground state energy $E_{test} \geq E_0$.

[1] For a given set of the electrons, which are moving by the field of "freezing" nuclei, the lowest energy configuration or state is known as a ground state.

The Hartree approximation (1928) [58] is the case where the many-body wave function is taken as a product of single-particle functions, i.e.

$$\Psi(\mathbf{r_1}, \mathbf{r_2}, ...\mathbf{r_N}) = \psi(\mathbf{r_1})...\psi(\mathbf{r_N}) \tag{2.13}$$

Respectively, each $\psi(\mathbf{r_i})$ function satisfies a one-electron Schrödinger equation with a potential term emerging from the other particles.

$$\left[-\frac{\hbar^2}{2m}\nabla^2 + V_{ext} + \Psi_i\right]\psi_i(\mathbf{r}) = \varepsilon\psi_i(\mathbf{r}), \tag{2.14}$$

where Ψ_i is the Coulomb potential given by Poisson's equation

$$\nabla^2\Psi_i = 4\pi e^2 \sum_{j=1, i\neq j}^{N} |\psi_j|^2, \tag{2.15}$$

and V_{ext} is the potential due to the "frozen" nuclei.

Unfortunately, the Hartree product[2] does not completely fulfil the significant standard for wave functions. Here, the electrons are fermions. Therefore, a wave function is obliged to change sign in the case that two electrons change their places with each other. This is well-known as the antisymmetry principle. The Hartree product does not change the sign due to the exchanging two electrons, which is a severe disadvantage. Fermi enumeration can be included by the replacement of the product wave function by a single determinant function [59, 60]. So-called Hartree-Fock approximation contains three major terms

$$E_{HF} = \langle\Psi_i|\hat{H}|\Psi_i\rangle = \sum_i^N (i|\hat{h}|i) + \frac{1}{2}\sum_i\sum_j [(ii|jj) - (ij|ji)] \tag{2.16}$$

with

$$(i|\hat{h}|i) = \int \psi_i^*(\mathbf{r}_i)\left[-\frac{1}{2}\nabla_i^2 - \sum_{k=1}^{m}\frac{Z_k}{r_{ik}}\right]\psi_i(\mathbf{r}_i)d\mathbf{r}_i \tag{2.17}$$

$$(ii|jj) = \int\int |\psi_i(\mathbf{r}_i)|^2 \frac{1}{r_{ij}} |\psi_j(\mathbf{r}_j)|^2 d\mathbf{r}_i d\mathbf{r}_j \tag{2.18}$$

$$(ij|ji) = \int\int \psi_i(\mathbf{r}_i)\psi_j^*(\mathbf{r}_j)\frac{1}{r_{ij}}\psi_j(\mathbf{r}_i)\psi_i^*(\mathbf{r}_i)d\mathbf{r}_i d\mathbf{r}_j \tag{2.19}$$

The first term presents the kinetic energy and the nucleus-electron interactions, where $\hat{h}$ denotes the single particle contribution of the Hamiltonian, and the two following terms

[2]The Hartree product is a wavefunction given as a combination of wavefunctions of separate particle wavefunctions. For case of two particles: $\Psi(\mathbf{r}_1, \mathbf{r}_2) = \psi(\mathbf{r}_1)\psi(\mathbf{r}_2)$.

correspond to electron-electron Coulomb interactions and exchange integral, respectively [61, 62].

Hartree-Fock approximation leads to a nonlinear "$\psi_i^{HF}(\mathbf{r})$" exchange of terms in the Schrödinger equation and the second nonlocal term under the sum, which is so-called Fock's potential [63]. Generally, HF approximation is used to resolve a time-independent Schrödinger equation for a many-body system (electrons, atoms, molecules) as described in the Born–Oppenheimer approximation[3]. So the "self-consistent field" method is a nonlinear method as an iteration introduced by the HF. The assumption of the HF approximation has a problem like the general many-body wave function, that can not be given as a single determination. Accordingly, the HF approximation does not correctly incorporate electronic correlation [64].

2.3 Density Functional Theory

The Density Functional Theory (DFT) was invented on the 1960s. DFT is a powerful and modern approach to the substance. Nowadays DFT applies for calculations of e.g. the binding energy, band structure of solids, thermodynamic properties. The fundamentals of the DFT is to represent the system of electrons of interaction by way of its density and not by its many-body wave function. The DFT reduces the problem of the ground state calculation in a local external field to the solution of the Hartree - like the one-electron equation [65–67]. The DFT shows that ground state within various properties of the system of electrons among an external field may be driven from information of the electron density distribution $n(\mathbf{r})$.

The DFT explicitly acknowledged the nonrelativistic Coulomb system dissimilarities by their potential $v(\mathbf{r})$ and delivers a formalism for dealing with the universal operators $\hat{T}$ and $\hat{U}$ [68]. With the help of replacing the product wave function by a single determinate function, the known Hartree-Fock approximation can be obtained, which leads to a nonlocal exchange term in the Schrödinger equation.

The DFT had built in an idea, that later on the many-body wavefunction $\Psi(\mathbf{r}_1, \mathbf{r}_2, ..., \mathbf{r}_N)$ would be replaced by a function which only depends on the electron density.

$$n(\mathbf{r}) = N \int d^3 r_2 ... \int d^3 r_N \Psi^*(\mathbf{r}_1, \mathbf{r}_2, ..., \mathbf{r}_N) \Psi(\mathbf{r}_1, \mathbf{r}_2, ..., \mathbf{r}_N) \tag{2.20}$$

This approach vastly reduces the degree of the problem. Instead of solving the $3N$ specified problem now only three functions are considered. The Ψ ground state wave

[3]The splitting of the nuclei and electrons into separate mathematical problems is the Born-Oppenheimer approximation. In the solid, nuclei appear only as a term of a potential $v(\mathbf{r})$ acting on the electrons.

function is a unique function of n_0 [65]. The Hohenberg-Kohn theorem is an important basis of the DFT.

$$\Psi_0 = \Psi[n_0] \tag{2.21}$$

Overall, the ground state energy is a function of n_0

$$E_0 = E[n_0] = \langle \Psi[n_0] | \hat{T} + \hat{V} + \hat{V}_{ext} | \Psi[n_0] \rangle, \tag{2.22}$$

where the external potential $\hat{V}_{ext}$ is

$$V_{ext} = \int V(\mathbf{r}) n(\mathbf{r}) d^3 r \tag{2.23}$$

There is an alternative principle for $n(\mathbf{r})$ regarding the density

$$E[n(\mathbf{r})] \geq E_0[n_0(\mathbf{r})] \tag{2.24}$$

where for degenerate ground states can be obtained by $E[n] = E_0[n]$. Therefore, it is not possible to find an initial density that leads to the ground state energy E_0. In 1976, Levy-Leblond proved that one can obtain the the energy functional $E[n(\mathbf{r})]$ as a minimum of all wave functions leading to the electron density $n(\mathbf{r})$ [69]:

$$E[n(\mathbf{r})] = \min_{n \to n_0} \langle \Psi | \hat{T} + \hat{U} + \hat{V}_{ext} | \Psi \rangle \geq E_0 \tag{2.25}$$

where $\hat{T}$ and $\hat{U}$ are universal functionals, and $\hat{V}_{ext}$ is the called non-universal functional since it depends on the system itself.

The evaluation of Equation 2.25 can be given as:

$$E[n(\mathbf{r})] = F[n(\mathbf{r})] + \int n(\mathbf{r}) v(\mathbf{r}) d\mathbf{r}, \tag{2.26}$$

where $F[n(\mathbf{r})]$ is

$$F[n(\mathbf{r})] = \min_{\Psi \to n} \langle \Psi_0 | \hat{T} + \hat{U} | \Psi \rangle. \tag{2.27}$$

At this point quickly, the ground state wave functions from the Equation 2.25 can be given by:

$$E[n(\mathbf{r})] = \langle \Psi | \hat{T} + \hat{U} + \hat{V}_{ext} | \Psi \rangle = E_0 \tag{2.28}$$

Thereby can be given the minimisation algorithm in order to obtain the ground state energy:

$$E_0 = \min_n E[n(\mathbf{r})] \tag{2.29}$$

This minimisation approach separates the set of occupied orbitals ψ_i, and the set of nuclei coordinates R_I. The advantageous of the minimization of the energy functional will produce the ground-state density $n_0(\mathbf{r})$ as well as obtain the ground state E_0, if one can provide the $F[n(\mathbf{r})]$ functional. But finding the $F[n(\mathbf{r})]$ is not so straightforward. Therefore one needs to have suitable approximations.

2.4 Kohn-Sham equations

The ground given by the Hohenberg-Kohn density-functional is not very useful in actual calculation. In 1965, Kohn-Sham [66] had the idea for an interacting system onto a system of non-interacting electrons. In order to derive the ground state energy within the charge density

$$E[n(\mathbf{r})] = T[n(\mathbf{r})] + \int n(\mathbf{r}) V_{ext}(\mathbf{r}) d\mathbf{r} + E_{ee} \tag{2.30}$$

The first term in Equation 2.30 defined as the kinetic energy of a non-interacting gas within $n(\mathbf{r})$ density. The second term is the interaction with the external potential, including the electron-nuclei interaction - Hartree potential energy. The last term is the electron-electron interaction which can be written as:

$$E_{ee}[n(\mathbf{r})] = \frac{1}{2} \int \frac{n(\mathbf{r}) n(\mathbf{r}^{'})}{|\mathbf{r} - \mathbf{r}^{'}|} d\mathbf{r} d\mathbf{r}^{'} + E_{xc}[n(\mathbf{r})] \tag{2.31}$$

The integral term is the electron-electron interaction and the second term is the exchange-correlation energy, which is non-classical electron interaction energy and also represents the difference between the kinetic energies of the interacting and non-interacting systems [68].

Substituting Equation 2.31 into Equation 2.30 and constructing of the Euler-Lagrange equations for the interactions [70]

$$\delta E[n^{'}(\mathbf{r})] \equiv \int \delta n^{'}(\mathbf{r}) \left[v_{eff}(\mathbf{r}) + \frac{\delta}{\delta n^{'}(\mathbf{r})} T_S[n^{'}(\mathbf{r})]|_{n^{'}(\mathbf{r}) = n(\mathbf{r})} - \varepsilon \right] d\mathbf{r} = 0 \tag{2.32}$$

with

$$v_{eff}(\mathbf{r}) \equiv v(\mathbf{r}) + \int \frac{|n(\mathbf{r})|}{|\mathbf{r} - \mathbf{r}^{'}|} d\mathbf{r} + v_{xc}(\mathbf{r}) \tag{2.33}$$

where $v_{xc}(\mathbf{r})$ is the derivative of

$$v_{xc}(\mathbf{r}) \equiv \frac{\delta}{\delta n'(\mathbf{r})} E_{xc}[n'(\mathbf{r})]|_{n'(\mathbf{r})=n(\mathbf{r})} \tag{2.34}$$

It is important to note here that the system of non-interacting particles moving in an external potential $v_{eff}(\mathbf{r})$ and for the case of finding the ground-state density $n(\mathbf{r})$ brings the solution of a single-particle Schrödinger's equations:

$$\left[-\frac{1}{2}\nabla^2 + v_{eff}(\mathbf{r})\right] \psi_i(\mathbf{r}) = \varepsilon_i \psi_i(\mathbf{r}) \tag{2.35}$$

for single-particle "$\frac{1}{2}N$" states $|\psi_i>$ and ε_i energy, the density adapted as:

$$n(\mathbf{r}) = 2\sum_{i=1}^{N/2} |\psi_i(\mathbf{r})|^2. \tag{2.36}$$

The factor 2 arises due to a spin degeneracy since the assumption here is that there are only single occupied orbitals. For non-interacting particles the kinetic energy $T_s[n]$ is:

$$T_s[n] = -\sum_{i=1}^{N/2} \int \psi_i^*(\mathbf{r}) \nabla^2 \psi_i(\mathbf{r}) d\mathbf{r} \tag{2.37}$$

Considering the Kohn-Sham potential assumes the density in order to solve these equations self-consistently, the Schrödinger equation calculates a set of orbitals from which a new density is constructed. This process is repeated until the input and output densities are the same. It is not difficult to achieve convergence to the ground-state minimum due to the convex nature of the density-functional [71].

For the non-interacting system, the energy is the sum of one electron's eigenvalues:

$$\begin{aligned} 2\sum_{i=1}^{N/2} \varepsilon_i = T_s[n] + \int n(\mathbf{r}) v_{eff}(\mathbf{r}) d\mathbf{r} = T_s[n] + \int \frac{n(\mathbf{r}) n(\mathbf{r}')}{|\mathbf{r}-\mathbf{r}'|} d\mathbf{r} d\mathbf{r}' + \\ + \int n(\mathbf{r}) V_{xc}(\mathbf{r}) d\mathbf{r} + \int n(\mathbf{r}) V_{ext}(\mathbf{r}) d\mathbf{r} \end{aligned} \tag{2.38}$$

The difference between the non-interacting system and the interacting system is the twice-counted Hartree energy and over-counts the exchange-correlation energy. Accordingly, the interacting energy is:

$$E = 2\sum_{i=1}^{N/2} \varepsilon_i - \frac{1}{2} \int \frac{n(\mathbf{r}) n(\mathbf{r}')}{|\mathbf{r}-\mathbf{r}'|} d\mathbf{r} d\mathbf{r}' + \int n(\mathbf{r}) V_{xc}(\mathbf{r}) d\mathbf{r} \tag{2.39}$$

The direct Schrödinger equation for non-interacting orbitals requires computational expenses which adjust the system size N to the diagonalize the Hamiltonian or orthogonalize the orbitals. The self-consistent equation is not a real Schrödinger equation, and the Hamiltonian itself depends on the eigenvalue problem.

The Equation 2.35 is called the Kohn-Sham equations. The self-consistent solution is a loop of the Kohn-Sham equations repeated until the change in the total energy within two consecutive iteration steps is smaller than a given $\Delta\varepsilon$ so called energy convergence. The loop is shown in the Figure 2.1

For the charge density, the efficient mixing (Equation 2.40) algorithm is another crucial step in achieving a self-consistent interaction. The primary quantity $R[n_{in}(\mathbf{r})]$, requires the minimization of the change density residual vector. There are two major methods [72]. One of them, the linear mixing or steepest-descent mixing method, is based on the addition of a certain amount of R to the current input charge density,

$$n_{in}^{i+1}(\mathbf{r}) = n_{in}^{i}(\mathbf{r}) + AR[n_{in}^{i}(\mathbf{r})] \tag{2.41}$$

This method normally is a wholly slow approach. The hypothesis here is that $R[n_{in}(\mathbf{r})]$ can be linearized around its root $n_{sc}(\mathbf{r})$,

$$R[n(\mathbf{r})] = -\mathbf{J}(n(\mathbf{r}) - n_{sc}(\mathbf{r})), \tag{2.42}$$

Then the convergence depends only on the eigenvalue spectrum of the Jacobian matrix $\mathbf{J}$. The linear mixing approach analysis was done by Dederichs and Zeller [73, 74].

The next approach is the Palay mixing [75], where the input charge density and residual vectors are supplied in a way that in each step a new optimal input charge density is given as a linear combination of the input charge densities of all previous steps,

$$n_{in}^{opt}(\mathbf{r}) = \sum_{i} \alpha n_{in}^{i}, \tag{2.43}$$

where the optimal α_i [76] is given by

$$\alpha_i = \frac{\sum_i A_{ji}^{-1}}{\sum_{kj} A_{kj}^{-1}}, \qquad A_{ij} = \langle R[n_{in}^{j}] | R[n_{in}^{i}] \rangle \tag{2.44}$$

So one can give:

$$\Delta n^{i}(\mathbf{r}) = n_{in}^{i+1}(\mathbf{r}) - n_{in}^{i}(\mathbf{r}) \Delta R^{i} = R[n_{in}^{i+1}] - R[n_{in}^{i}] \tag{2.45}$$

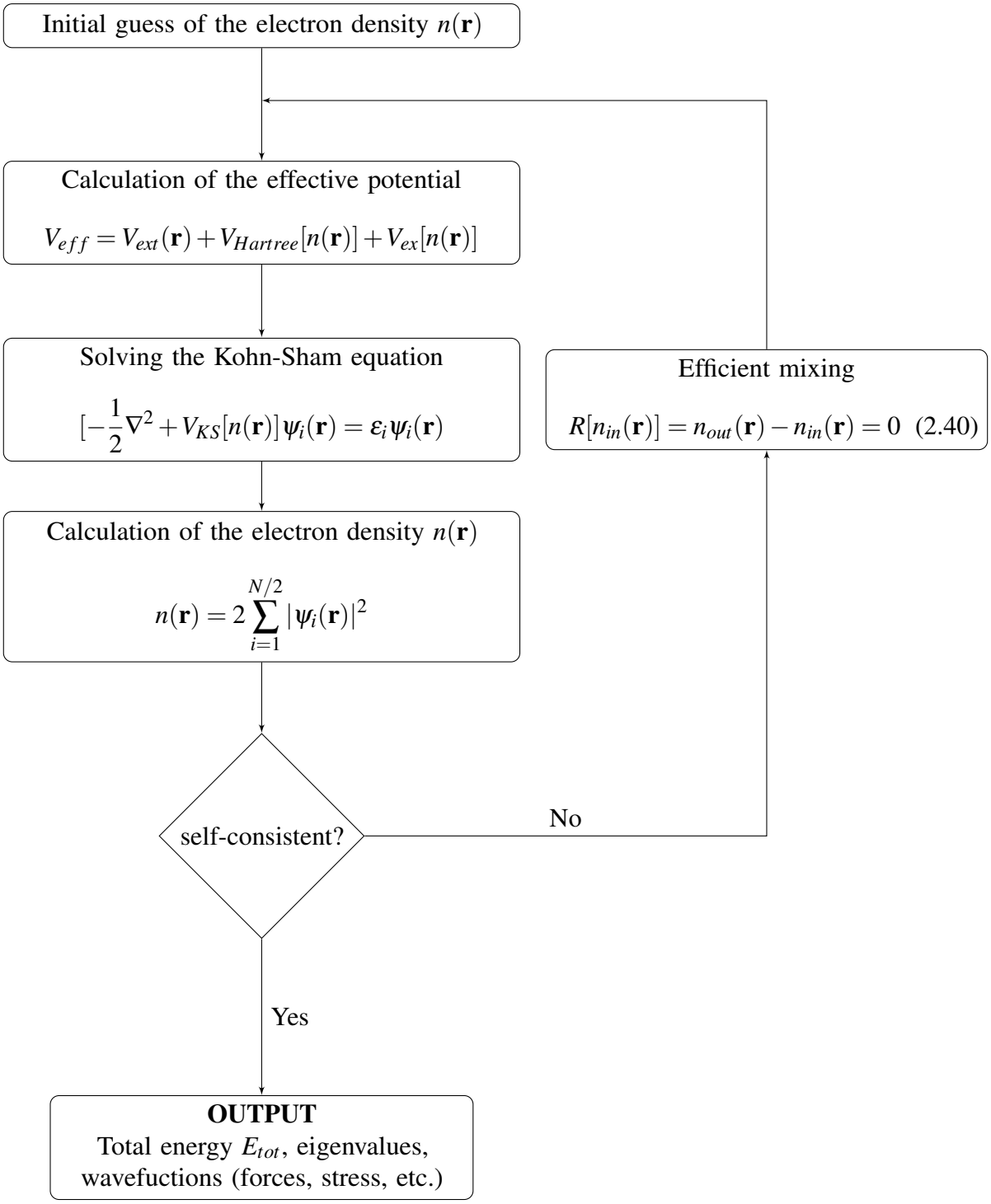

Figure 2.1: Diagram of interaction used within DFT calculations. The convergence criterion $\Delta\varepsilon$ depends on the solving problem.

Subtracting the Equation 2.41 for i and $i+1$ interaction and multiplying on the left hand side with $\mathbf{J}^{-1}$ yields $\mathbf{J}^{-1}|\Delta R^i\rangle = -|\Delta\rho^i\rangle$

2.5 Exchange-Correlation Functionals, Pseudopotentials

The following section explores the numerical approaches. So far, the Kohn-Sham equation Equation 2.35 did not require any approximations. It is provided with the identical ground state density of the fully interacting system onto a subsidiary non-interacting system..

As noted above, the kinetic energy in the Kohn-Sham equation is not the *true* kinetic energy. It is used formally to define the exchange-correlation energy as [77, 78]:

$$E_{xc}[n(\mathbf{r})] = T[n(\mathbf{r})] - T_s[n(\mathbf{r})] + E_{ee}[n(\mathbf{r})] - E_H[n(\mathbf{r})], \tag{2.46}$$

where $T_s[n(\mathbf{r})]$ and $E_{ee}[n(\mathbf{r})]$ are the exact kinetic and electron-electron interaction energy respectively.

Objectively, this term is clarified as containing the deposits to the system energy of comprehensive correlation and exchange. The interpretation above is such that it confirms that the Kohn-Sham formulation is exact. Nevertheless, the actual form of it is not known. That is where the approximate functionals come, which are based on the electron density to characterising this term. There are two general approximations (in various forms): the local density approximation (LDA) [68], and the generalised gradient approximation (GGA) [79].

The simpler approximation is the LDA, in which it is assumed, that the point the exchange-correlation energy E_{ex} at the point $\mathbf{r}$ is simply equal to the exchange-correlation energy in the homogeneous electron gas, which has the same electronic density at the point $\mathbf{r}$.

$$E_{xc}[n(\mathbf{r})] = \int \varepsilon_{xc}(\mathbf{r}) n(\mathbf{r}) d\mathbf{r}, \tag{2.47}$$

The exchange-correlation potential V_{xc} can be written as:

$$V_{xc} = \frac{\delta E_{xc}[n(\mathbf{r})]}{\delta n[\mathbf{r}]} = \frac{\partial [n(\mathbf{r})]\varepsilon_{xc}(\mathbf{r})}{\partial n(\mathbf{r})}, \tag{2.48}$$

where

$$\varepsilon_{xc}(\mathbf{r}) = \varepsilon_{xc}^{hom}[n(\mathbf{r})] \tag{2.49}$$

The Equation 2.49 assumes that the exchange-correlation energy is entirely local. The variable ε_{xc}^{hom} is given by Perdew and Zunger [80]. It is based on the quantum Monte-Carlo

calculation on homogeneous electron gases for a given discrete densities by Ceperley and Alder [81].

The LDA approximation cannot improve the exchange-correlation energy caused by inhomogeneities in the electron density. Based on this assumption, the outstanding success of the approximation is surprising. Substantially, it appears [82] that because of the concern of the LDA to the sum rule, that at the point **r** one-electron is excluded from the immediate vicinity of a given electron.

The GGA approach comprehends the effects of inhomogeneities by including the gradient of the electron density. The GGA exchange-correlation functional can be written as:

$$E_{xc}^{GGA}[n(\mathbf{r})] = \int n(\mathbf{r})\varepsilon_{ex}^{hom}[n(\mathbf{r})]F_{xc}[n(\mathbf{r}),\nabla n(\mathbf{r})]d\mathbf{r} \tag{2.50}$$

where $F_{xc}[n(\mathbf{r}),\nabla n(\mathbf{r})]$ is included as the enhancement factor. In contrast to the LDA approximation, there is no particular form for the GGA approximation, indeed many achievable deviation are possible [82–85], each corresponding to the accuracy of the various factors. The GGA approximation benefits in reducing the effects of overbinding found in the LDA approximation [86], and is significantly more successful when applied to molecules.

The pseudopotential method in term of the orthogonalised planewave (OPW) method [87] has been applied in this work. The valence wavefunctions were expanded using a basis composed of planewaves which were orthogonalised to the core states. The elegance and effectiveness of pseudopotentials have considered, and the following intentions have instructed the evolution:
1. The pseudopotential should be as soft as possible, expecting that it should able to represent the valence pseudo-wavefunctions using as few planewaves as possible.
2. The pseudopotential should be as transferable as possible.
3. The charge density using the pseudo-wavefunctions should reproduce the valence charge density as accurately as possible. In the planewave pseudopotential approach, the Hamiltonian is substituted by a pseudo-Hamiltonian, that is constructed to reproduce the original eigenvalue spectrum in the valence region as well as the wavefunctions outside some distance of the nucleus.

2.6 Lattice Dynamics and Harmonic Approximation

As previously mentioned, the DFT works best on the "freezing" nuclei, therefore not all the physical properties can be gained from ground state theories. This is also true for thermal properties, which are of interest to this study, such as the effects dependent on

the temperature, like thermal expansion, phase transitions, etc. The Thermodynamic data can be used to predict the equilibrium products of the decompositions. Furthermore, the thermodynamical predictions can be useful in mechanistic studies because of the evidence that observed primary reaction products differ from those identified as being most stable and can be used in formulating the reaction mechanism.

The study of the jointed atomic vibrations in a crystal is lattice dynamics. In 1930 Tamm [88] introduced the concept of phonons through the observation of particle-like atomic vibrations energies in a crystal, similar to the wave–particle duality in quantum mechanics. Since that time, lattice dynamics has become a significant branch of condensed matter physics and for the comprehension the thermal properties of crystalline solids [89, 90]. The lattice dynamics based on the Bohn-Oppenheimer or adiabatic formalism, which assumed that the electronic wave functions, change adiabatically via the nuclei motion. The lattice dynamics associate only with the nuclei motions. The crystal potential energy for the small displacements of the atoms u from their equilibrium positions can be given as a Taylor expansion. The extension remains upon the second derivative, which is called harmonic approximation. The simplest case is a linear chain of atoms, each with the same mass m, within a distance a_0

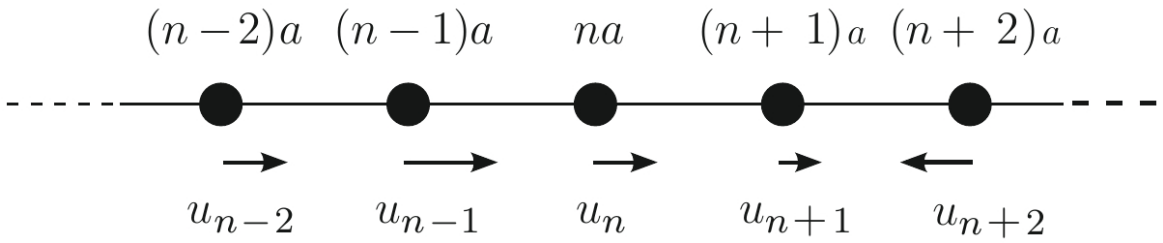

Figure 2.2: Longitudinal displacements in a one-dimensional monoatomic lattice. The equilibrium positions $t_n = na$ are indicated by circles; the displacements u_n at a given instant are indicated by arrows [1]

The energy between two neighbours at a distance of r is $E_0(a)$, the total energy of a chain of N atoms becomes:

$$E = NE_0(a) \tag{2.51}$$

and the Taylor series can be given as:

$$E(x) = NE_0 + \sum_{s\geq 1} \frac{1}{s!} \frac{\partial^s E_0}{\partial u^s} \sum_n (u_n - u_{n+1})^s \tag{2.52}$$

The distances between two displaced atom is $r = a + (u_n - u_{n+1})$. Since **r** is the equilibrium position, the first derivative of E_0 is zero, which means that the $s = 1$ expansion in the Taylor series [91] will vanish. As the displacement is small in comparison to the atomic distance the quadratic in u is dominant. The energy of this system is the same as the energy of a set of harmonic oscillators, hence this approximation called *harmonic approximation*.

Within the harmonic approximation in case of small displacement ($u << a$), the total crystal energy becomes

$$E_0^{(harm)}(u_n) = E_0(0) + \frac{1}{2}\sum_{nn'} D_{nn'} u_n u_{n'} \tag{2.53}$$

and the second derivatives of the ground state energy $E_0(u_n)$ is classified at the equilibrium.

$$D_{nn'} = (\frac{\partial^2 E_0}{\partial u_n \partial u_{n'}})_0 \tag{2.54}$$

The *interatomic force constants* is $D_{nn'}$. The *dynamical matrix D* is formed with the $D_{nn'}$ interatomic force constants [1], and its diagonalisation produces the *normal vibrational modes* or *phonon states* of the system under investigation. In the harmonic approximation, it can be given by

$$F_n = -\frac{\partial E_0^{harm}}{\partial u_n} = -\sum_{n'} D_{nn'} u_{n'} \tag{2.55}$$

The energy Equation 2.53 for the linear chain, in the matter of interaction between nearest neighbours within the elastic force of spring constant K can be written by

$$E_0^{harm} = \frac{1}{2} C \sum_n (2u_n^2 - u_n u_{n+1} - u_n u_{n-1}) \equiv \frac{1}{2} K \sum_n (u_n - u_{n+1})^2 \tag{2.56}$$

From the Equation 2.54, is clear that the D matrix is real and symmetric.

Now the considered classical equation of the motion of the n-th particle in the chain with mass m in the position $R_n = na + u_n$ under the F_n force will be

$$m\ddot{u}_n = -\sum_{n'} D_{nn'} u_{n'}, \tag{2.57}$$

where $n = 1, 2, ..., N$. The solution of Equation 2.57 suggests being in the form of waves, which are periodic in space and time [91]

$$u_n(t) = Ae^{i(qna - \omega t)}, \tag{2.58}$$

where the A is an amplitude of the displacement, and it is the same for all sites. Substituting Equation 2.58 into Equation 2.57 and recasting the equation, it can be written as

$$m\omega^2(q) = D(q), \tag{2.59}$$

where

$$D(q) = \sum_{n'} D_{nn'} e^{-iq(na-n'a)} \tag{2.60}$$

All of this can be addressed a general lattice dynamic of a three dimensional crystal with N unit cells, $\mathbf{d}_1, \mathbf{d}_2, ..., \mathbf{d}_N$ positions of the atoms and with $\mathbf{t}_N$ translation vectors. According to the adiabatic approximation, the nuclei are fixed in the positions $\mathbf{t}_N + \mathbf{d}_N + \mathbf{u}_N$ and the energy of the electronic-nuclear system is $E_0(\mathbf{u_n})$ [1, 3, 2].

For the nuclei vibrations the classical equation from Equation 2.57 is

$$m\ddot{u_n} = -K(2u_n - u_{n+1} - u_{n-1}) \tag{2.61}$$

As we already know, the solution of the Equation 2.61 should be given as a wave function that is periodic in a space and time.

$$u_n(t) = Aexp^{i(qna-\omega t)} \tag{2.62}$$

By direct substitution from Eqs.2.59 - 2.60 yields

$$-m\omega^2 = -K(2 - e^{iqa} - e^{-iqa}) = -4Ksin^2\frac{1}{2}qa \tag{2.63}$$

The dispersion relation for normal modes is thus

$$\omega = \sqrt{\frac{4K}{m}}|sin\frac{1}{2}qa| \tag{2.64}$$

It is illustrated, that the spectrum of vibrational frequencies falls in a range of zero to $\omega_{max} = \sqrt{\frac{4K}{m}}$. The solution which is equal to zero for small q is called the *acoustic branch*. It resembles the distribution of acoustic waves through the crystal. The clarification that is ω_{max} at q = 0 is termed the *optical branch*. It is this kind of the vibrations which are possible to connect to vibrations in an electromagnetic field [3].

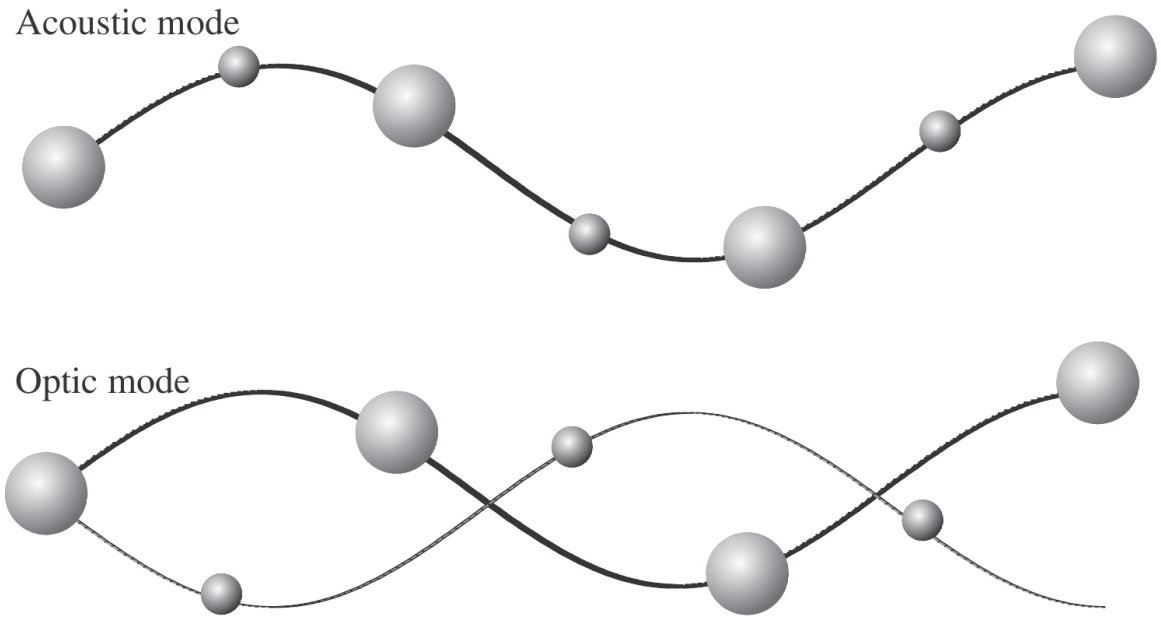

Figure 2.3: Exaggerated transverse atomic motions in a one-dimensional diatomic crystal for an acoustic mode (motions of different types of atoms are in phase) and an optic mode (motions of different types of atoms are out of phase). [2]

2.7 Phonons and Heat Capacity

Historically, the study of the heat capacity of solids was one of the significant successes of quantum theory. Within classical statistical mechanics, interpretation of the heat capacity for insulators at room temperature is sufficient but it is unsuccessful at low temperature, and it entirely fails for metals. It is supposed that metals should have considerably higher heat capacity than insulators due to their more free electrons, but in reality, metal's heat capacity is similar to an insulator at room temperature [3].

We discussed the lattice vibrations by midpoints of the classical equations of motion. In the harmonic approximation, the Hamiltonian [1] of the Equation 2.56 becomes

$$H = \sum_n \frac{1}{2m} p_n^2 + \frac{1}{2} K \sum_n (2u_n^2 - u_n u_{n+1} - u_n u_{n-1}), \tag{2.65}$$

where u_n and p_n are the coordinate and conjugate moment of the nucleus at the n-th site. Thus it can be defined as

$$p_q = \frac{1}{\sqrt{N}} \sum_{t_n} e^{+iqt_n}(p_n, u_q) \frac{1}{\sqrt{N}} \sum_{t_n} e^{-iqt_n}(p_n, u_n) \tag{2.66}$$

The collective operators are defined as linear combinations of the dynamic variables of all the nuclei, with appropriate phase factors, for example, $(\pm iqt_n)$ as suggested by the Bloch form. The expression of the original Hamiltonian regarding the new collective displacements and conjugate momenta will be

$$H = \sum_q [\frac{1}{2m} p_q p_{-q} + \frac{1}{2} m\omega_q^2 u_q u_{-q}] \tag{2.67}$$

The minus sign here means that the Hermitian conjugates of collective operators of wavenumber q are the linear combinations of wavenumber $-q$. In the Equation 2.67 the $\omega^2(q)$ is

$$\omega^2(q) = \frac{K}{m}(2 - e^{-iqa} - e^{iqa}) = \frac{4K}{m} sin^2 \frac{qa}{2} \tag{2.68}$$

It is shown that coupled harmonic oscillators within the linear chain and the uncoupled normal modes of the corresponding frequency given above agree with Equation 2.68.

The explanation of the temperature-dependent specific heat capacity for solids was made by A. Einstein, where the key idea was to solve a problem using quantum theory. The energy of a harmonic oscillation is quantised, assuming that the solid's vibrations are represented by independent harmonic oscillators where all have the same frequency.

$$E_0 = \frac{1}{2}\hbar\omega, \tag{2.69}$$

is also called the *zero-point energy* and corresponds motions at $T = 0K$ [2]. The energy of the vibration can be converted by integral units of the phonon energy $\hbar\omega$. Energy of each vibrational mode is:

$$E = \hbar\omega \left[\frac{1}{2} + n(\omega, T)\right], \tag{2.70}$$

where $n(\omega, T)$ is the number of phonons with frequency ω at temperature T, and it is called the *phonon number* [2]. The number of phonons substantial in the thermal equilibrium at any temperature $n(\omega, T)$ is given by the Bose-Einstein distribution

$$n(\omega, T) = \frac{1}{e^{\frac{\hbar\omega}{k_B T}} - 1} \tag{2.71}$$

The most familiar of these quanta is applied to light, where they are called photons. A single wave of atomic oscillation is similarly quantised; the quantum, in this case, is called a phonon [3, 1]. Consider a crystal composed of N unit cells with frequency $\omega = \omega(\mathbf{q}, p)$ [1],

where $\mathbf{q}$ has N allowed values in the Brillouin zone, and p operate over $3v_b$ (v_b is a basis of atoms in the unit cell), the harmonic phonon energy of the crystal is [91]:

$$E = \sum_{\mathbf{q},p} \hbar\omega(\mathbf{p},q)[\frac{1}{2} + n(\omega,T)] = \sum_{\mathbf{p},q} \hbar\omega(\mathbf{p}.q)[\frac{1}{2} + e^{(\frac{\hbar\omega(\mathbf{p},q)}{k_B T} - 1)^{-1}}] \tag{2.72}$$

This function is given for a constant volume the internal energy, as the harmonic model does not allow for thermal expansion. For a constant volume, the heat capacity [91] is

$$C_V(T) = \left(\frac{\partial E}{\partial T}\right)_V = \sum_{\mathbf{q},p} \hbar\omega(\mathbf{q},p)\frac{\partial n(\omega,T)}{\partial T} = \sum_{\mathbf{q},p} k_B \left(\frac{\hbar\omega(\mathbf{q},p)}{k_B T}\right)^2 \frac{e^{\frac{\hbar\omega}{k_B T}}}{e^{[\frac{\hbar\omega}{k_B T} - 1]^2}} \tag{2.73}$$

Equation 2.73 allows the numerical calculation of the lattice heat capacity of the crystal, in the case of know phonon dispersion $\omega(\mathbf{q},p)$. At high temperature, namely $k_B T \gg \hbar\omega$, E and C_V with simplicity become equal to $3NZk_B T$ and $3NZk_B$ respectively, Z is the number of atoms in the unit cell, and N is the number of unit cells in the crystal. At low temperatures is shows an exponential behaviour, whereas the experiments show a power law behaviour $C \propto T^3$. At sufficiently low temperatures, almost all the oscillators are in their ground state. At the high-temperature limit, the thermal energy is more extreme than the distribution between the energy levels $\hbar\omega_E$ and the quantised nature of the problem is irrelevant.

2.8 Phonon free energy, density of states (DOS) and entropy

For phonons given by Bose-Einstein relation, the free energy of the phonons can be obtained with help the partition function. So for $3N_A$ oscillators the energy [3] is

$$\langle E \rangle = 3N_A \left(\frac{1}{e^{\frac{\hbar\omega}{k_B T}} - 1} + \frac{1}{2}\right)\hbar\omega \tag{2.74}$$

For a three-dimensional solid the thermal energy for a set of oscillators, where the frequencies given by Equation 2.68 and the zero point energy $\frac{\hbar\omega}{2}$ is neglected since it does not promote to the heat capacity, is given by

$$\langle E \rangle = 3\int_0^{\omega_D} \frac{\hbar\omega}{e^{\frac{\hbar\omega}{k_B T}} - 1} d\omega, \tag{2.75}$$

where ω_D in the highest phonon frequency in the material. The factor 3 appears from the three possible wave polarisation for a delivered ω. If, there is a frequency interval like $\omega_1 + d\omega$ then $\omega_2 + d\omega$ and it should be included by a weighting factor $g(\omega)$ in the integral. The $g(\omega)$ called as the *density of states*. In the integral, the the upper limit ω_D should also be established.

$$\langle E \rangle = 3 \int_0^{\omega_D} \frac{g(\omega)\hbar\omega}{e^{\frac{\hbar\omega}{k_B T}} - 1} d\omega \tag{2.76}$$

In the case of optic modes, the force is constant, and the density of states has no particular shape. Nevertheless, regarding acoustic modes, there is an exact dependence of frequency and wave vector as $q \to 0$, as $\omega = cq$, where c is an average velocity of sound, and q is the modulus of the wave vector. The number of wave vectors with values between q and $q + dq$ is given by $g(q)dq$ and the two distribution functions become

$$g(\omega)d\omega = g(q)dq \tag{2.77}$$

The $g(q)$ is a straightforward approach to consider the distribution of individual wave vectors across a lattice grid. In a crystal that consist of N unit cells with total volume V, the unit cell volume is V/N. The volume at the Brillouin zone is $V_{BZ} = (2\pi)^3 N/V$. Since the defined crystal contains N unit cells, there are N wave vectors in one Brillouin zone, and of the number of wave vectors per unit volume is $N/V_B Z = V/(2\pi)^3$. The number of wave vectors in a shell of radius q and thickness dq is equal to

$$g(q)dq = \frac{V}{(2\pi)^3} 4\pi q^2 dq \tag{2.78}$$

Substituting $q = \frac{\omega}{c}$ and $dq = \frac{d\omega}{c}$ will yield [2]

$$g(\omega)d\omega = 3\frac{V}{(2\pi)^3} 4\pi \left(\frac{\omega}{c}\right)^2 \frac{d\omega}{c} = \frac{3V\omega^2}{2\pi^2 c^3} d\omega \tag{2.79}$$

The noticeable outcome of this result is that $g(\omega) \propto \omega^2$, which means the limitation for $g(\omega)$ when $\omega \to 0$ for all crystals.

In thermodynamics, the Debye model was developed in 1912 [92] for estimating the phonon contribution to the specific heat in a solid. It concerned the vibrations of the lattice as phonons in a box and as non-interacting quantum harmonic oscillators. The specific heat from the Debye theory via energy can be expressed as

$$F(\omega) = \int g(\omega)\hbar\omega \left[\frac{1}{2} + \frac{1}{e^{\frac{\hbar\omega}{k_b T}} - 1}\right] d\omega \tag{2.80}$$

It goes without saying that in normal mode coordinates, the linearized lattice vibrations are equivalent to $3N$ independent harmonic oscillators, where each oscillator corresponds to a different normal mode.

$$\int g(\omega) d\omega = 3N \tag{2.81}$$

Considering all, the isobaric heat capacity C_p cannot be derived that easily using only the phonon density state $g(\omega)$. It requires a theory which represents the volume expansion dependent on the temperature. This can be done if one considers a set of different volumes and searches for the minimum in the Gibbs free energy G [2].

$$G(T,p) = \min_V [E_0(V) + F_{vib}(V,T) + PV] \tag{2.82}$$

The starting point is the equilibrium structure at zero pressure and temperature $T = 0K$. The volume increases which corresponds to the energy increment, but the majority of vibrational frequencies will decrease.

The free energy can be defined as the sum of the inner energy and the electronic and vibrational degrees of freedom contributions.

$$F(T,V) = E_0(V) + E_{el}(T,V) - T \cdot S_{el}(T,V) + F_{vib}(T,V) \tag{2.83}$$

$$F_{vib}(T,V) = k_b T \int D_{ph,V}(E) ln(1 - e^{-\frac{E}{k_b T}}) dE \tag{2.84}$$

This way the gain in energy is counterbalanced by an increase in entropy with a subsequent contribution of $-TS$ to the free energy. Thus a temperature which this new volume corresponds to the minimum of the overall free energy will be reached. The basis of the *quantum harmonic approximation* (QHA) that the temperature dependence of the phonon frequencies is only related to the volume of a crystal, since the anharmonic part is in general due to the thermal expansion. The specific heat capacity at constant pressure is obtained by

$$C_p(T) = T(\frac{\partial S}{\partial T})_p = -T \left(\frac{\partial^2 G(T,p)}{\partial T^2}\right)_p \tag{2.85}$$

The entropy is the first derivative of the Gibbs free energy. As there is no pressure in the DFT calculation, the Gibbs free energy $G(T,p)$ is equal to the Helmholtz free energy, which is

$$F(V,T) = E_0(V) + F_{vib}(V,T). \tag{2.86}$$

An estimation of Equation 2.82 yields the dependencies of $V_{min}(T)$ and $F_{min}(T)$, and also the thermal expansion

$$\alpha_v(T) = \frac{1}{V_{min}(T)} \left(\frac{\partial V_{min}(T)}{\partial T} \right)_p \tag{2.87}$$

Considering that the volume depends on temperature, the bulk modulus[4] can be given as

$$B_T = B(V_{min}) = -V_{min} \left(\frac{\partial p}{\partial V} \right)_T = V \left(\frac{\partial^2 F(V,T)}{\partial V^2} \right)_T \tag{2.88}$$

The moderate bulk modulus is

$$B_0 = B(V_{min}) \tag{2.89}$$

2.9 Electrons and Heat Capacity

Until now, only the contributions to the specific heat capacity from vibrations within the solid, but there is contribution from the electrons were considered. The electrons contribution to the specific heat capacity depends on the system itself. The electrons bring more deposit in the case of low temperature, and in the case phonons cover up the high-temperature range. The conduction of electrons can be treated as an ideal gas. However, the concentration of such electrons in a metal far outstrips the concentration of particles in a conventional gas. Therefore, it is not unexpected that conducted electrons cannot normally be analysed using classical statistics, but in fact, they are directed to Fermi-Dirac statistics. The predictable way to calculate the electron's contribution on the specific heat capacity is to calculate the heat capacity for a free electron then multiply by the number of free electrons N in the system. However, this approach was found to be certainly high for solids [93]. The ground state is the state of the N-electron system at absolute zero, and it returns to the standard problem in the case when the temperature is increased. The solution is given by the Fermi-Dirac distribution function, which is the probability that an orbital with energy ε will be occupied [3].

[4] Bulk modulus, is a qualification that characterises the elastic properties of a solid when it is under pressure. Under the pressure a material decreases its volume, which rebounds to its preliminary volume when the pressure is removed.

$$f(\varepsilon) = \frac{1}{e^{\frac{\varepsilon-\mu}{k_b T}} + 1}, \tag{2.90}$$

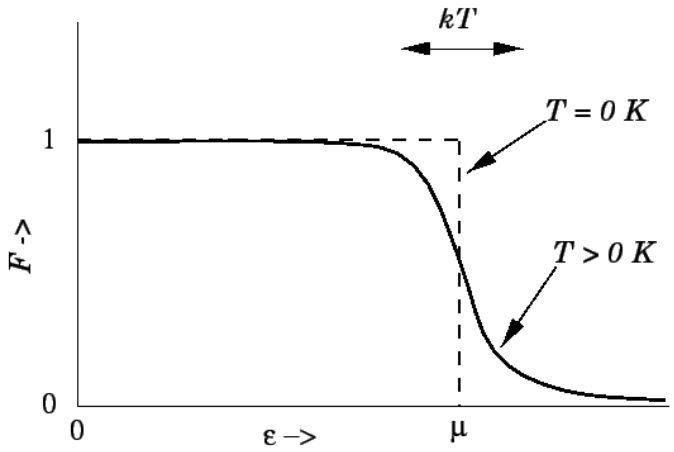

Figure 2.4: The illustration of the Fermi-Dirac distribution function. The transition region in which F goes from a value close to unity to a value close to zero corresponds to an energy interval of order kT, centred on $\varepsilon = \mu$.

The μ is a function of the temperature and it is the chemical potential, and it is chosen for each particular problem in such a way that the total number of particles in the system is correct and equal to N. At $T = 0K$ the $\mu = \varepsilon_F$. The distribution function $f(\varepsilon)$ in case of $T \to 0$ chanes from 1(filled) to 0(empty) at $\varepsilon = \varepsilon_F = \mu$ (see Figure 2.4). The high energy tail of the distribution is the part where $\varepsilon - \mu \gg k_b T$; here the exponential term is dominant in the denominator, so $f(\varepsilon) \cong e^{(\frac{\varepsilon-\mu}{k_b T})}$. This limit is denominated the Boltzmann or Maxwell distribution [93].

Let us calculate the Fermi energy μ_0 for gas at $T = 0K$. For each particle the energy can be related to its momentum $\mathbf{p} = \hbar\mathbf{q}$ so

$$\varepsilon = \frac{p^2}{2m} = \frac{\hbar^2 k^2}{2m}, \tag{2.91}$$

where k is the de Broglie wave-vector. At $T = 0$ all quantum states with energy less than the Fermi energy μ_0 are filled. The Fermi energy correlates to a Fermi momentum $p_F = \hbar k_F$ such that [3]

$$\mu_0 = \frac{p_F^2}{2m} = \frac{\hbar^2 k_F^2}{2m}, \tag{2.92}$$

and k_F is called the Fermi wave vector.

Suppose there are N electrons in the enclosed volume, such that the conduction electron density is $n = \frac{N}{V} = \frac{N}{L^3}$. Since there can be two electrons per state, it makes the $N/2$ states. Per unit volume of **k** - space there are $(2\pi)^{-3}V$ permitted translational states. In **k**-space the volume of the sphere with radius k_F is $(4/3)\pi k_F^3$, which indicates that the Fermi sphere of radius k_F has $(4/3)\pi k_F^3$ translational states. Therefore, the total number of occupied states is:

$$2\frac{V}{(2\pi)^3}\left(\frac{4}{3}\pi k_F^3\right) = N. \tag{2.93}$$

Equation 2.93 can be presented as

$$k_F = \left(3\pi^2\frac{N}{V}\right)^{1/3}. \tag{2.94}$$

Accordingly, the de Broglie wavelength corresponding to the Fermi energy λ_F can be given by:

$$\lambda_F \equiv \frac{2\pi}{k_F} = \frac{2\pi}{(3\pi^2)^{1/3}}\left(\frac{V}{N}\right)^{1/3}, \tag{2.95}$$

At $T = 0$ all quantum states are occupied if $\lambda \equiv 2\pi/k > \lambda_F$ and if $\lambda < \lambda_F$ is empty.

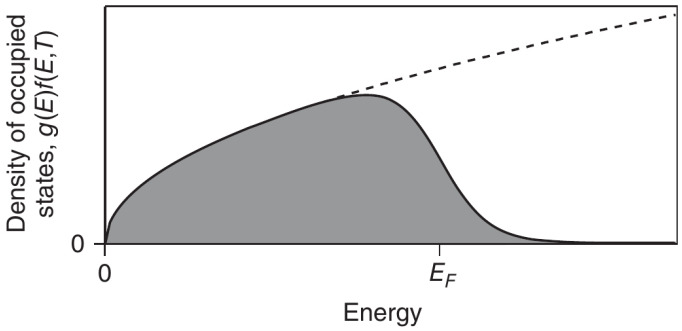

Figure 2.5: Density of occupied states $g(E)f(E,T)$ [3].

The Fermi energy from the Equation 2.92 at $T = 0K$ becomes:

$$\mu_0 = E(N) = \frac{\hbar^2}{2m}\left(3\pi^2\frac{N}{V}\right)^{2/3}. \tag{2.96}$$

For the metals at room temperature $\mu_0 \gg kT$.

From Equation 2.96 the *density of states* of electrons can be calculated, which is the energy-dependent number of available states per energy interval dE [3].

$$g(E) = \frac{dN}{dE} = \frac{V}{2\pi^2}\left(\frac{2m}{\hbar^2}\right)^{\frac{3}{2}} E^{\frac{1}{2}} \tag{2.97}$$

Until now, the condition at $T = 0$ was considered, but any composition of temperature will bring the excitation from the ground state of electrons. The occupation probability is given by the Fermi-Dirac distribution Equation 2.90

After all, the *density of occupied electron states* at a given energy and temperature can be accomplished by multiplying the density of states $g(E)$ with the Fermi–Dirac distribution $f(E,T)$ Figure 2.5.

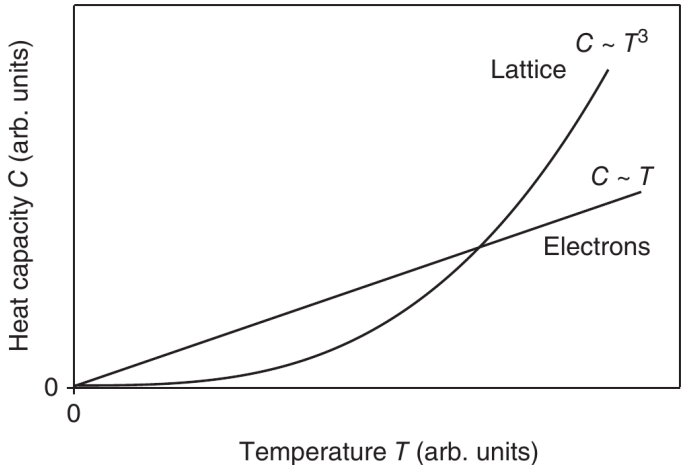

Figure 2.6: Sketch of the electronic and lattice contributions to the heat capacity. At sufficiently low temperatures, the electronic contribution dominates [3].

In the case of solids, the temperature growth can only be thermally excited for a slight fraction of the electrons. Consequently, a contribution to the heat capacity is, in fact, only possible for the electrons near the Fermi energy. The number of electrons is on the order of $k_b T g(E,F)$. If the mean thermal energy of these electrons is $3k_bT/2$, the total thermal energy is

$$\langle E \rangle = \frac{3}{2} k_b T g(E_F) k_b T \tag{2.98}$$

The heat capacity is

$$C = \frac{\partial \langle E \rangle}{\partial T} = 3k_b^2 T g(E_F) \tag{2.99}$$

So, the heat capacity is proportional to the density of states at the Fermi energy $g(E_F)$, since only the electrons close to the Fermi energy can participate in thermal excitations. Figure 2.6 illustrates that at low temperature, the lattice vibrational contribution vanishes

compare to the low-temperature electronic contribution and via version in case of high temperature.

2.10 Elastic properties

Elastic properties were calculated within the Lagrangian theory of elasticity [94], where a solid is viewed as a homogeneous, anisotropic elastic medium and the strain-stress is represented as:

$$\eta = \varepsilon + \frac{1}{2}\varepsilon^2, \tag{2.100}$$

$$\tau = det(1+\varepsilon)(1+\varepsilon)^{-}1 \cdot \sigma \cdot (1+\varepsilon)^{-1} \tag{2.101}$$

The ε in Equation 2.100 and σ in Equation 2.101 accordingly represent the strain tensor and stress tensor, where the $(\cdot)$ indicated a tensor product. Afterwards, the elastic tensor can be obtained by the deformation of the unit cell and calculation of the corresponding stress tensor as a function of strain. The results in the linear elastic regime were calculated using the Elastic tool provided by Golesorkhtabar et al. [95].

Chapter 3

Thermodynamics and material properties

3.1 Intermetallics

Intermetallic materials are the short term for the intermetallic phases, or compounds obtained by combining various metals, and they comprise numerous categories of materials. The intermetallics are compounds of metals, even though their crystal structures are not the same as the constituent metals, and include the ordered alloys [96]. During the last few decades interest in intermetallics has increased enormously due to their applications at high temperature, and a new class of structural materials of intermetallics are now under the extensive investigation. The atomic ordering in the intermetallics should afford a higher deformation resistance at high-temperatures [97]. The intermetallics have been found to be brittle material, but it was also found that various intermetallics are often used for strengthening the second phases in the conventional alloys [98]. This is what makes the intermetallics promising in their application as a structural material at high temperatures. Some intermetallics used for alloy systems that have a low melting temperature, and the applications pertain to the exceptional hardness and wear resistance of the intermetallics, together with their metallic properties. The importance of the complex investigation of intermetallics crystal structures, generally restrictive stoichiometry limits, and the limitations imposed by the equilibrium phase diagrams were reviewed by Westbrook et.al. [99].

The intermetallics are materials that possess the characteristica of both metals and ceramics, and usually, they possess long-range-ordered crystal structures. This mixing bond type provides the mechanical properties that are somewhere between those of metals and ceramics. Al-Fe based intermetallics have known since the 1890's [100]. Al-Fe intermetallics

are being developed as the structural materials for engineering alloys. These materials exhibit outstanding resistance to corrosion in oxidant environments at high temperature through the formation of slow growing, and they have low-density [97]. The oxidation resistance of Al-Fe based intermetallics depends on the chemically stable alumina. Examination of the Fe-Al-O system phase stability determined that alumina, even with a low partial pressure of oxygen, will form within Fe alloys [101]. Additionally, Al-Fe systems entail a considerable commercial interest, since Fe is regularly present at significant levels (0.2 - 1wt.%) as an impurity in Al raw material, because of the solidification process.

The thermodynamic properties of solid comprise a large rang of properties. But the ones most acknowledged are specific heat, phase transitions, thermal expansion, and thermal conductivity. In this chapter, the focus will be on the thermodynamic properties of different intermetallics like η - Fe_2Al_5, ε - Fe_5Al_8 and τ_4 - Al_3FeSi_2.

3.2 Al-Fe binary systems

The aluminium-based intermetallic alloys are mostly present in the transition metals. Recently, there has been high interest in such alloys because of their complex crystalline structures and their compounds, which have the significant technological use. The experimental resolution of their phase diagram is a difficult process, given the existence of many phases within small composition ranges. Also, most structures usually have large unit cells, and many of them are fundamentally disordered, exhibiting mixed or partially occupied sites.

Ab-initio first principle calculations can help resolve some uncertainties in the phase diagrams, but this approach has its own challenges particularly because of structural disorder, since DFT requires the realisations of particular site occupancy. Another difficulty that stands in front of DFT is the large unit cells.

The Al-Fe systems are the prototype of the binary magnetic alloys based on a *bcc* structure [102]. There is also interest from a theoretical point of view, because of several transitions between the disordered phase A2 (SG #229, $Im\bar{3}m$) and the ordered phases B2 (SG #221, $Pm\bar{3}m$) and $D0_3$ (SG #225, $Fm\bar{3}m$) in the Fe-rich side, e.g. $A2 \leftrightarrow B2$, $A2 \leftrightarrow D0_3$ and $D0_3 \leftrightarrow B2$ [4, 44]. See Table 3.1 and Figure 3.1.

The most commonly used assessment [103] of the thermodynamic databases has not been published collectively, and compared the with experimental data. Also, the two-sublattice model used can describe only the B2 ordered but not $D0_3$ phase. As reported by Sundman [4], there have been several modifications to improve various features, but without proper documentation or publication. The interest in those particulate phases came from the believe that the theoretical calculation via DFT can bring forth the fundamental thermodynamic

Phase	Label in Figure 3.1	Structure report	Space group	Prototype
Liquid	Liquid			
fcc	A1	A1	$Fm\bar{3}m$	Cu
bcc	A2(pm) or A2(fm)	A2	$Im\bar{3}m$	W
AlFe	B2(pm)	B2	$Pm\bar{3}m$	CsCl
$AlFe_3$	$D0_3$	$D0_3$	$Fm\bar{3}m$	$BiFe_3$
Al_8Fe_5	Al_8Fe_5	$D8_2$	$I4\bar{3}m$	Cu_5Zn_8
Al_2Fe	Al_2Fe		$P1$	$FeAl_2$
Al_5Fe_2	Al_5Fe_2		$Cmcm$	
Al_13Fe_4	Al_13Fe_4		$C2/m$	

Table 3.1: Phases and structures

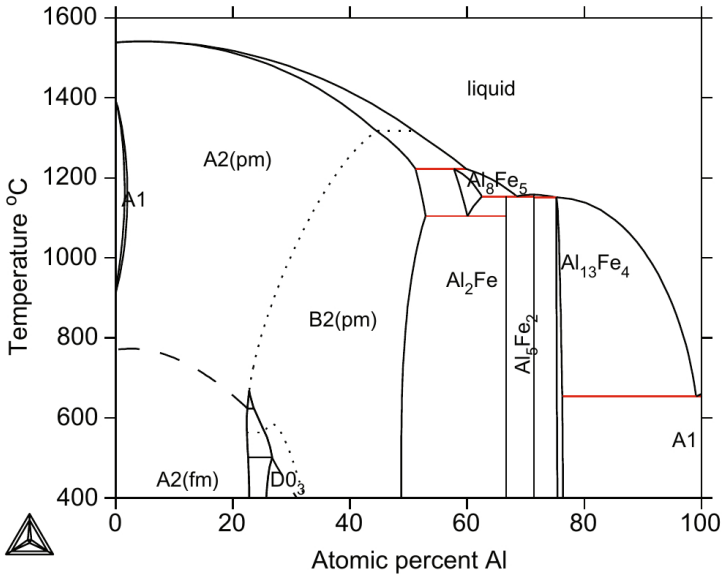

Figure 3.1: The calculated Al-Fe phase diagram from the current assessment. The lines representing the second-order transitions between the chemically ordered states are short dashed and those between the ferromagnetic and paramagnetic states are long dashed [4].

properties of intermetallics. This, in turn, would help build a foundation for a new CALPHAD type assessment of the Al-Fe system [8, 104]. The Al-Fe system is also a key system in the thermodynamic description of Al-Fe-Si [105].

3.2.1 η - Fe_2Al_5

The η - Fe_2Al_5 structure has been presented by Burkhardt et al. [5] and Schubert et al. [106]. Experimentally, it was found that the η - Fe_2Al_5 structure is orthorhombic with a space group (SG #63, *Cmcm*) and has partially occupied lattice sites. The structure of η

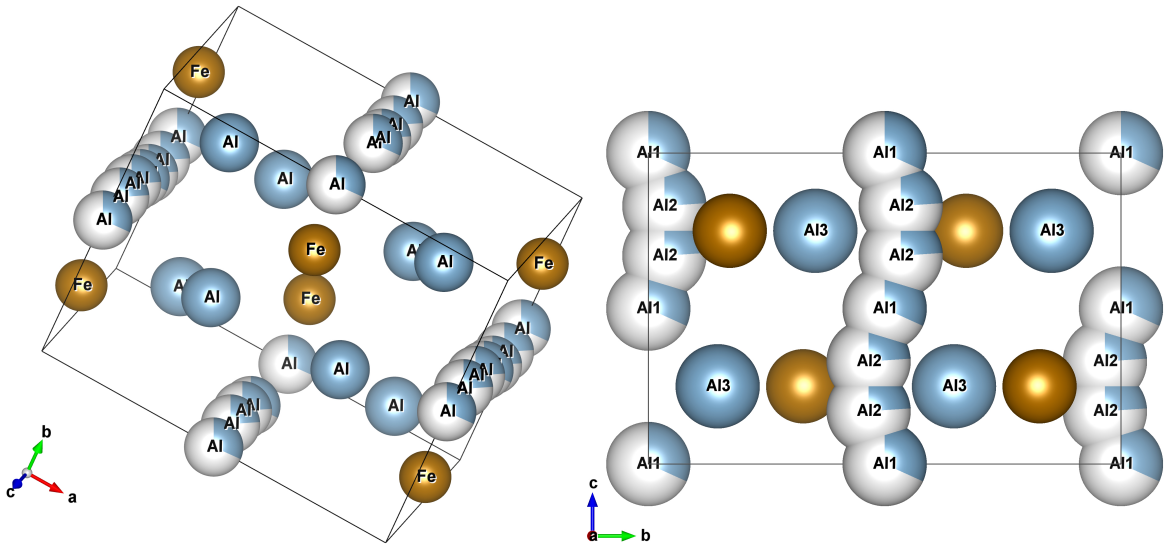

Figure 3.2: The η - Fe_2Al_5 experimentally determined structures. On the left is the structure given by Burkhardt [5], on the right is the structure from the ICSD [6] database. This structure was found with the help of X-ray and electron diffraction methods and shows two channels of partially occupied aluminium sites running parallel to the c-direction, resulting from the diffusion of the Al atoms. There are two distinguishable Al-sites Al1 and Al2 with occupancies of 0.32 and 0.24 respectively. The Fe and Al3 sites are fully occupied [7].

- Fe_2Al_5 in the presented papers [5, 106] have sites partially occupied by Al in the c-axis direction as shown in the Figure 3.2, which leads to the chemical composition of $Al_{5.6}Fe_2$ and the cell parameters had been found to be a = 7.6559 Å, b = 6.4154 Å, c = 4.2184 Å, V = 207.19 Å^3 and $\alpha = \beta = \gamma = 90^o$.

Furthermore, this type of structure cannot be considered as an input for DFT, e.g. for the QUANTUM ESPRESSO code [46]. Certain atomic positions are required from DFT. For those types of structures, an idealised structure model should be found, with full occupied lattice sites. Therefore, a set of possible structures with the Al_5F_2 composition had been selected. The modelled structures obtained by deleting some partially occupied atomic positions and making the remaining ones full. The entire modelling of the structure was carried out via the full optimisation calculations, known as cell parameters and atomic positions optimisation. All structures were found to end up with the same atomic positions and had only slight difference in total energy [7]. The selected approximate structure, which was used to carry out the specific heat capacity calculation, had the lowest total energy with monoclinic structure (SG #12, $c2/m$) and lattice parameters a = 4.2093 Å, b = 7.3784 Å, c = 6.4773 Å, V = 200.92 Å^3, $\alpha = 92.863^o$ and $\beta = \gamma = 90^o$ [13]. The presented cell-parameters

show a break in symmetry. The Wyckoff positions for an optimised structure is given in Table 3.2.

		x	y	z
Al(1)	2a	0.0000	0.0000	0.0000
Al(2)	8j	0.1825	0.6561	0.2550
Fe	4i	0.0000	0.3383	0.2412

Table 3.2: The optimised Wyckoff positions of η - AlFe (SG #12, $C2/m$ unique axis b cell choice 1) obtained from the density-functional-theory calculations [13].

As per usual practice, the most important setting values were tested for convergence with different pseudopotentials, local density approximation (LDA) [107] and generalised gradient approximation (GGA) [108]. The single-electron Kohn-Sham states were calculated on a k-point grid of $3 \times 4 \times 5$ points and the valence electron wave functions were extended in a plane wave basis, with a cutoff energy of 80 Ry. The effective potential was reached in reciprocal space on a grid with a cutoff frequency equivalent to 400 Ry in a case of GGA pseudopotential, and $4 \times 4 \times 6$ of k-points within 50 Ry energy cutoff for LDA pseudopotential were found to be reasonably accurate. Further, a degauss value of 0.001, and an ecutrho energy of 400 Ry were used in all subsequent calculations [7]. The settings that have been tested in any calculations are presented in Appendix A.2 with all their meanings, along with some convergence tests for k-point grid and cutoff. More details can also be found in the "pw.x" documentation of the QUANTUM ESPRESSO package [108]. Afterwards, the pwtools package was employed [109] to obtain the complete thermodynamical calculations by creating nine $2 \times 2 \times 2$ supercells. The full relaxation mechanism was repeated for a different volume in the range of -1 to 5% compared to the relaxed volume, since, as a result of this volume change, the atoms were not located in their equilibrium positions [7]. Then, the slight displacement of the single atomic position of each supercell was created by the phonopy code. Overall, 14 displacement structures were sufficient, if there was no broken symmetry. From the QUANTUM ESPRESSO employed force calculation, the phonon DOS could be obtained.

3.2.2 ε- Fe_5Al_8

Within the Al-Fe intermetallic binary system exists a high-temperature phase denoted as ε, which occurs in the Al-Fe system with about 58-65 at. % Al, with a hitherto unknown crystallographic structure. The ε phase exhibits a stable high-temperature phase at 1368 - 1504 K [9]. Study of the ε-FeAl intermetallic phase structure theoretically is advantageous

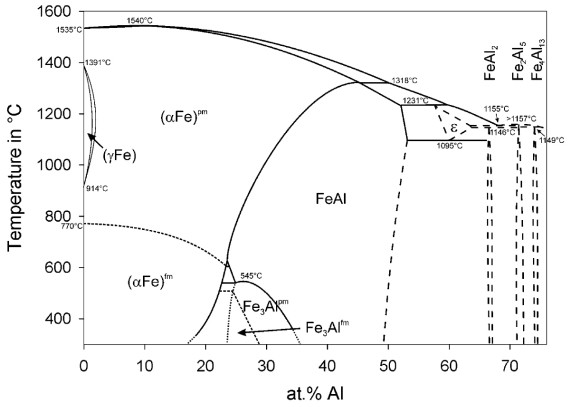

Figure 3.3: Phase diagram of the Fe-Al system showing the phase field of the high-temperature 3 phase near 60 at. % Al [8].

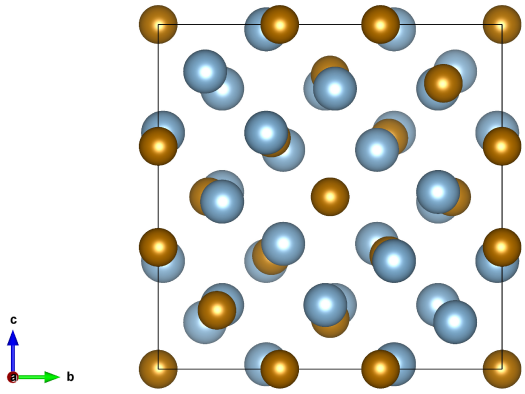

Figure 3.4: Crystal structure of ε - Al_8Fe_5 [9]: projected along (001) net plane. Drawing were done with VESTA [10].

because of the difficulties regarding the examination of the high-temperature structures experimentally. The phase formula for ε-FeAl is Fe_5Al_8, in the $I\bar{4}3m$ (SG #217) space group, structure designation $D8_2$ [8] with 52 atoms in the unit cell. The unit cell parameters represented as a = b = c = 8.9756 Å with $\alpha = \beta = \gamma = 90^o$. Although several crystallography structures were proposed for ε-AlFe, Vogel et. al. [9] found a ε phase formula as a Fe_5Al_8 at 1390 K via high-temperature neutron diffraction measurement, with 59.4 ± 0.6 at. % Al. It is appropriate for the Fe-rich boundary of the homogeneity range of the Fe_5Al_8 phase. The lattice parameter of Fe_5Al_8 becomes 3 times *FeAl* (B2) cubic structure at the same temperate [9]. The Fe_5Al_8 phase is known as a phase which forms from phases FeAl and $FeAl_2$.

The thermodynamic calculation was carried out with the same method as previously presented for η - Fe_2Al_5, where the single-electron Kohn-Sham states were calculated on a k-point grid of $4 \times 4 \times 4$ points. The valence electron wave functions were appended in a plane wave basis with a cutoff energy of 90 Ry. In the case of GGA pseudopotential and the productive potential was expanded in reciprocal space on a grid with a cutoff frequency equivalent to 450 Ry. These are the values which were achieved after the convergence tests. The degauss value was given as $1E-5$. After the full optimisation of cell parameters and atomic positions the structure space group remains the same as was presented by Vogel et.al. [9] ($I\bar{4}3m$, SG #217). Since the structure has 52 atoms in a unit cell, the creation of a $2 \times 2 \times 2$ supercell structure would give a large cell containing almost 432 atoms. With that amount of atomic numbers, the calculation via DFT is not reasonable due to its high cost. Therefore, in the case of the ε-Fe_5Al_8 phase, the thermodynamical calculations were accomplished by creating $1 \times 1 \times 1$ so-called supercells, which were used for the phonon calculations at the

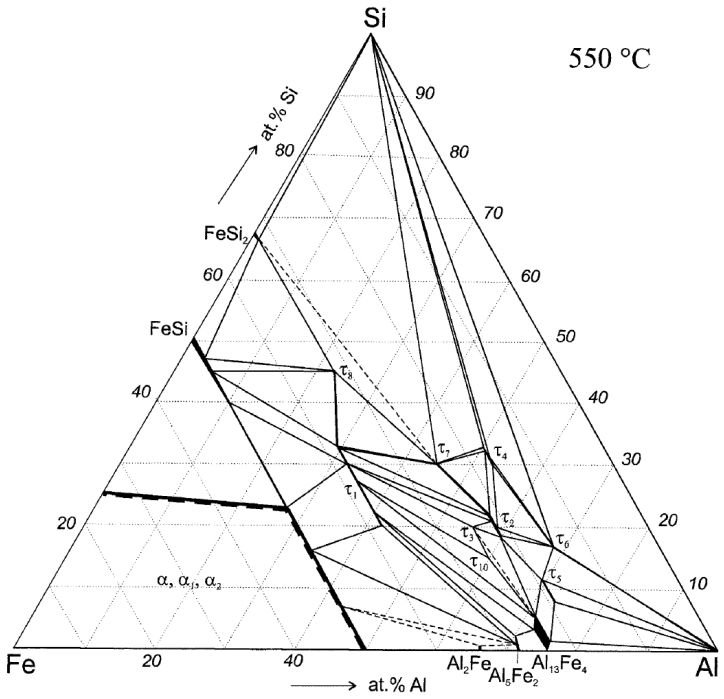

Figure 3.5: Isothermal section for 550^oC (note: phase boundaries shown are schematic only) [11].

gamma points. Ten displacement structure have been set up for ten different volumes with the corresponded space group. The change of the cell volume was in the range of -15 to 5 %. Following the QUANTUM ESPRESSO employed force calculation the phonon DOS could be obtained. As mentioned above, the η - Fe_2Al_5 is the high-temperature stable phase. Therefore, the imaginary frequencies in the case of volume pressed structures are more stable than from the expanded volume structures.

3.3 Al-Fe-Si ternary systems - τ_4 phase

Takeda [110] performed the first comprehensive study of phase equilibria of the entire Al-Fe-Si ternary system. Thermodynamic properties for ternary alloys were also investigated by measuring the heat of formation of solid alloys [111, 112] and the standard heat of formation of ternary intermetallics [113–115]. Furthermore, thermodynamic modelling of the ternary system has also been carried out by the CALPHAD method [116–119], where simple analytical functions describe the Gibbs energies of the relative phases.

The thermodynamic description of Du et al. [120] contains ten ternary compounds, and later Marker et. al. [105] found the eleven ternary phases. Nonetheless, experimental data on

the specific heat capacity of the intermetallic phases in the Al-Fe-Si system are missing. In these cases the thermodynamic data is commonly expressed the Neumann-Kopp rule [45], which is based on the extensive collection of experimental data on specific heat capacity for solid substances. The law is formulated as follows: each element in the state of compounds has essentially the same specific heat capacity as it has in its free state.

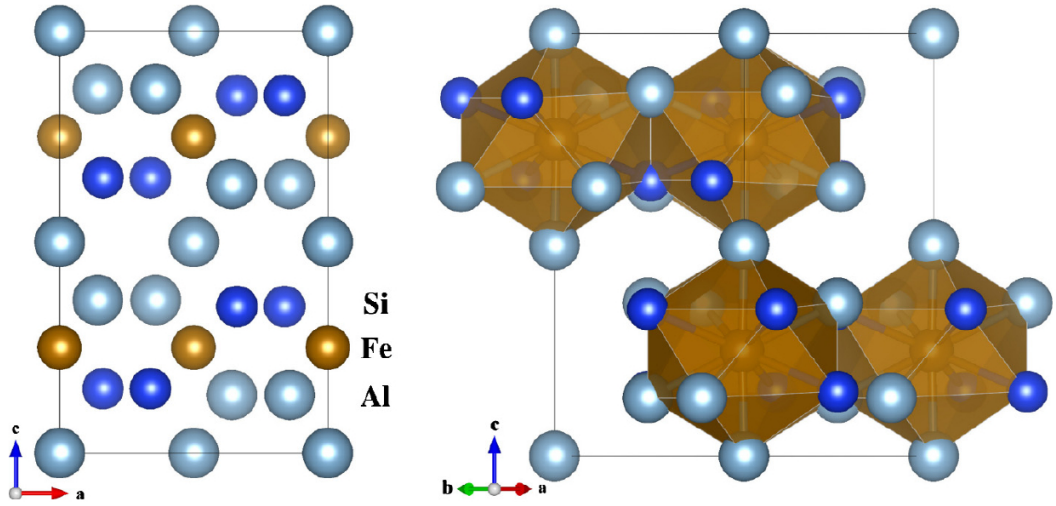

Figure 3.6: Crystal structure of τ_4 - Al_3FeSi_2: projected along (010) net plane (left), showing the ordered distribution of Si (dark) and Al (light). On the right side, the coordination polyhedra with Fe in the centre are outlined. With lines are drawn the unit cell edges. Drawings were done with VESTA [10]. [12]

Panday and Schubert [121] determined the crystallographic structure for the ideal composition Al_3FeSi_2 in the τ_4 phase. The investigation was followed by Gueneau et al. [122], who indicated superstructure reflections. The structure was reinterpreted as orthorhombic with space group *Pbcn* and lattice parameter $a = b = 6.061$ Å, $c = 9.525$ Å and $\alpha = \beta = \gamma = 90^o$ (see Figure 3.6). The atomic distances between Fe-Al/Si are 2.38 Å and 2.85 Å, where the short ones belong to the tips of the bipyramids. The Al-Si distances range between 2.66 Å and 2.72 Å. In Al_3FeSi_2, the Si exhibits metallic bonding, which is highly different from the diamond-type structure, where Si presnts as a covalent semiconductor [12]. After full optimisation of the structure cell-parameters and atomic position the obtained structure had $a = 6.06112$ Å, $b = 6.05789$ Å, and $c = 9.46554$ Å, with $\alpha = \beta = \gamma = 90^o$ in the space group *Pbcn* (SG #60).

Along with DFT thermodynamic data the calculation of the τ_4 phase gives a broad range of temperature data. In contrast, the measurement is restricted to a narrow temperature interval. For this purpose the Quantum ESPRESSO code was used the PAW pseudopotentials [123] supplied with the program. For this structure, were used settings with a cutoff energy

of 80 Ry, a cutoff frequency equivalent to 280 Ry, and a $11 \times 11 \times 7$ k-points grid. The PBE [124] GGA exchange-correlation functional is employed. The crystal structure parameters are optimised to first obtain their equilibrium values. Then the density functional perturbation theory (DFPT) [125] as implemented in Quantum ESPRESSO is used, to calculate the vibrational properties of the compounds for several different unit cell volumes. The phonon dispersion relation for each volume is calculated for a k-point grid of 72 points in the Brillouin Zone. Applying the calculated phonon density of states (DOS) $D_{ph,V}(E)$ for each value, and lattice vibrations free energy can be calculated from statistical quantum mechanics [126]. The phonon DOS for τ_4 structure is obtained through a quasiharmonic approximation method over the volume change in a range of 10% compared to the relaxed volume. In total, ten structures were considered. For each volume, the temperature dependence of the free energy is given by Equation 2.83.

3.4 Results and Discussion

As was mentioned above, there is a shortage of experimental specific heat capacity data for binary and ternary phases of Al-based intermetallic systems and the Neumann-Kopp rule does not always give consistent results. However, DFT calculations could be used to extrapolate thermodynamic functions in CALPHAD type modelling. Therefore, the above-discussed structures were investigated to achieve a specific heat capacity and results were compared with the experimentally measured specific heat capacity via differential scanning calorimetry (DSC).

On the assumption of quantum mechanics, in particular density functional theory (DFT), it is possible to calculate $F(T,V)$ (Equation 2.83) from first principles. The free energy $F(T,V)$ is a fundamental quantity in thermodynamics that can be used to calculate other thermodynamical properties. Nowadays, within the framework of Hohenberg, Kohn and Shame [127] based DFT is implemented in numerous computer programs for calculations within periodic boundary conditions.

The free energy can be defined as the sum of the inner energy and the electronic and vibrational degrees of freedom contributions.

The electronic energy $E_{el}(T,V)$ is a modification of the temperature independent DFT total energy using the Fermi distribution, and it depends on temperature and the Fermi energy E_F. The assumption here is that the existence of lattice vibrations does not affect $E_{el}(T,V)$ and $S_{el}(T,V)$ and calculated these terms for the undisturbed lattice. The free energy is a minimum at thermodynamical equilibrium. As a result, the volume for fixed T temperature can govern of finding the minimum of F(T,V) and consequently $F_{min}(T,V)$ can

be reconstructed [2].
Here, $E_0(V)$ is the total electronic energy at $T = 0\ K$ for a DFT calculation at a given volume V. The thermal excitation of the electrons are described by $E_{el}(T,V)$. The $S_{el}(T,V)$ is the corresponding entropy of the electron gas and $F_{vib}(T,V)$ describes the phonon contribution to the free energy in Equation 2.83. The minimum free energy F_{min} and the corresponding volume V_{min} are found for each temperature. The thermophysical properties of interest can then be obtained from temperature and volume derivatives of the free energy $F(T,V_{min})$. The specific heat capacity c_p is given by Equation 2.85. Afterwords, can be reached the volumetric thermal expansion coefficient by Equation 2.87 and bulk modulus by Equation 2.88.
Whenever practical, such derivatives were assessed analytically. In the DFT calculation, the plane-wave and potential cutoff were separately adjusted to each free-energy contribution to guarantee converged results.

3.4.1 Results of η Fe_2Al_5 structure

As discussed above, η - Fe_2Al_5 structure in the literature is given with partially occupied sites of atomic positions. Therefore, the DFT calculation required an approximated structure, which was created by removing some of the partially occupied sites and completely filling the remaining lattice sites.

$$C_{ij} = \begin{bmatrix} 236.1 & 56.4 & 93.9 & 0 & 0 & 0.7 \\ 56.4 & 243.9 & 52.2 & 0 & 0 & 1.5 \\ 93.9 & 52.2 & 246.7 & 0 & 0 & 1.5 \\ 0 & 0 & 0 & 56.4 & 9.1 & 0 \\ 0 & 0 & 0 & 9.1 & 85.0 & 0 \\ 0.7 & 1.5 & 1.5 & 0 & 0 & 108.8 \end{bmatrix} \tag{3.1}$$

The calculated thermal expansion coefficient and bulk modulus are shown in Figure 3.9 for η - Fe_2Al_5 structure.

Compared to the orthorhombic structure suggested by Burkhardt et al. [5] the structure obtained from the variable cell optimisation has lower symmetry. The spacegroup #12 requires 13 independent elastic constants which are shown in equation 3.1 in GPa using the Voigt notation for the elastic force constant tensor. According to Voigt notation the bulk modulus is $B_V = 125.7 GPa$ and the shear modulus is $G_V = 85.0 GPa$ at $T = 0K$.

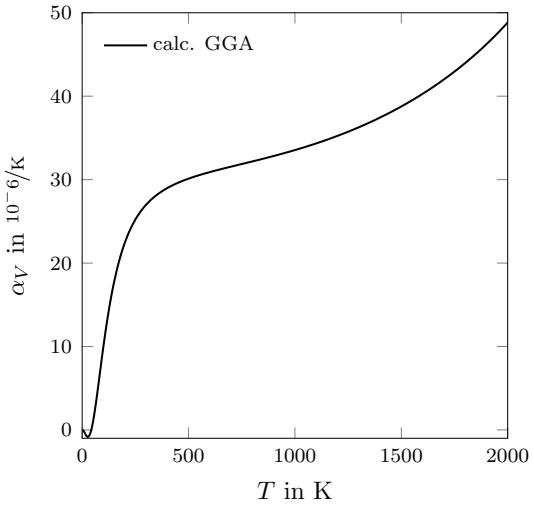

Figure 3.7: Calculated volumetric thermal expansion coefficient of Fe_2Al_5 between 0 K and 2000 K after equation (2.87).

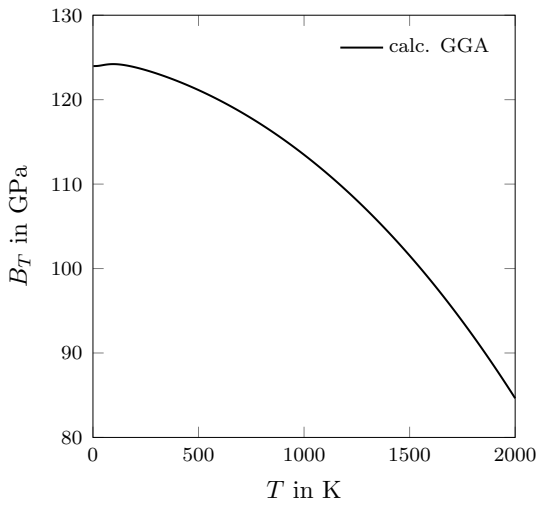

Figure 3.8: Calculated bulk modulus of Fe_2Al_5 between 0 K and 2000 K after equation (2.88).

Figure 3.9: The pictures were presented by Zienert [13].

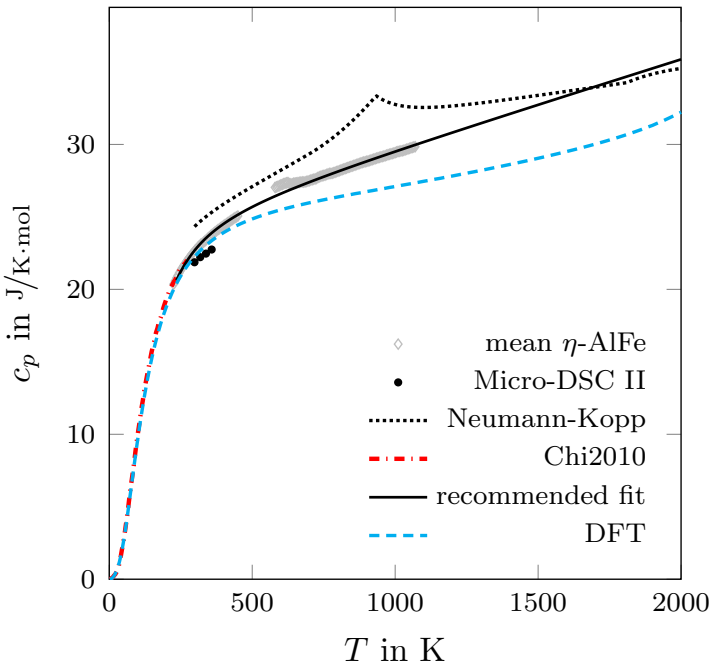

Figure 3.10: Recommended experimental determined heat capacity in comparison to the experimental data by Chi et al. [14] and the heat capacity obtained from DFT calculations [13].

The Figure 3.10 shows that this approach works very well for the prediction of heat capacity at low temperatures down to 460 K. As high temperatures, the disordered structure stabilises as a result of partial occupation. Therefore, the prediction from DFT shows a slightly less heat capacity than experimentally measured. However, the calculation of thermophysical properties was performed up to 2000 K, which is above the melting point of η - Fe_2Al_5 (1431 K).

3.4.2 Results of ε Al_8Fe_5

In the case of ε - Al_8Fe_5, the thermodynamical properties were obtained with respect to the phonon frequency calculation at the *gamma* point. The calculated energy-volume curve and the phonon density of state are shown in figures (Figure 3.11, 3.12). The ε - Al_8Fe_5 structure represent a kind of behaviour where one can see that the structure likes to be under pressure. This conduct may be explained because of the fact, that the ε - Al_8Fe_5 structure is a high temperature structure. Nonetheless, the DFT calculation is done at T = 0 K.

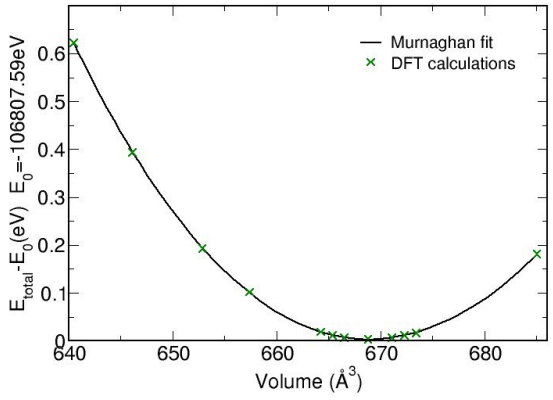

Figure 3.11: Energy-volume curve for ε - Al_8Fe_5. The line is calculated from Murnaghan equation fitted to the calculated DFT data.

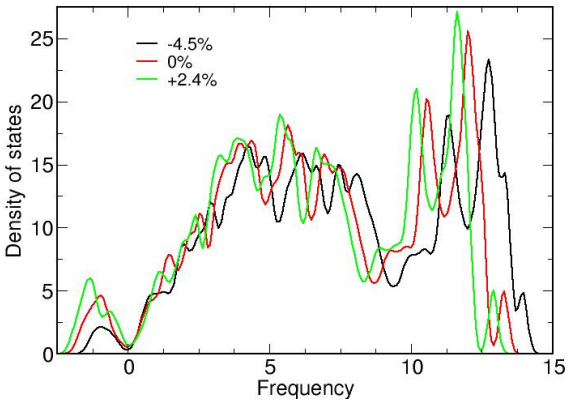

Figure 3.12: Phonon density of state (DOS) of ε - Al_8Fe_5.

The DOS (Figure 3.12) shows that the negative imaginary part in phonon frequency become smaller in the compressed structure compared to an optimised-minimum volume and the expanded volume. The obtained bulk modulus is $B_0 = 152.46GPa$, and the optimized volume is $V_0 = 668.93\text{Å}^3$.

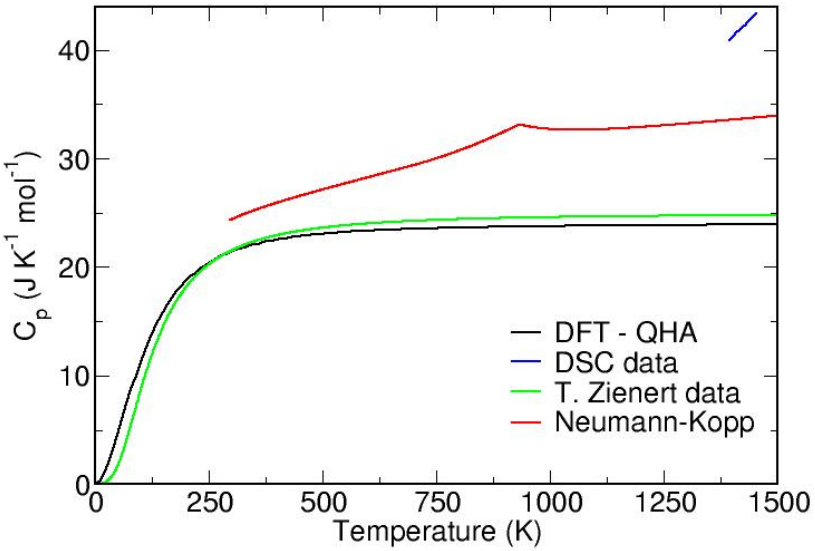

Figure 3.13: Specific heat capacity in comparison to the experimental data via DSC and the specific heat capacity obtained from DFT calculations. The green line is the calculated specific heat capacity by T. Zienert code and the red line corresponds to the calculated heat capacity using Neumann-Kopp rule.

The specific heat capacity obtained from the DFT calculation seems to be reasonable. Although the DSC experimental result of the specific heat capacity, in its short temperature range, is almost twice higher than one calculated from DFT. Besides, it has a sharp increase shape. This behaviour corresponds to the response of the material when it has a phase transition or nears to its melting point. The estimated result of Neumann-Kopp is between two results from DFT and DSC. In the Figure 3.13 present a predicted thermodynamic calculation by the code from T. Zienert (subproject A03). The ε - Al_8Fe_5 is present at 1370 K [9, 8] and it was noted that the specific volume and cubic lattice parameters depend on the temperature increase nearly linear. In the case of the DFT calculation there is an unusual attitude of volume expansion, which can be explained by its short temperature range existence.

$$C_{ij} = \begin{bmatrix} 82.4 & 130.1 & 130.1 & 0 & 0 & 0 \\ 130.1 & 82.4 & 130.1 & 0 & 0 & 0 \\ 130.1 & 130.1 & 82.4 & 0 & 0 & 0 \\ 0 & 0 & 0 & 17.2 & 0 & 0 \\ 0 & 0 & 0 & 0 & 17.2 & 0 \\ 0 & 0 & 0 & 0 & 0 & 17.2 \end{bmatrix} \tag{3.2}$$

The calculated elasticity tensor of ε - Al_8Fe_5 is shown in equation 3.2 in Voigt notation. The unit of the matrix entries is GPa in Voigt notation and as a consequence of the space

group #217 (cubic structure) the independent elastic constants are three. Due to the condition of stability in crystal systems [128] one can see as well instability is presented in C_{ij} via $(C_{11} - C_{12} < 0)$.

3.4.3 Results of τ_4 Al_3FeSi_2 structure

The calculated Al_3FeSi_2 elasticity tensor is shown in the equation 3.3, in Voigt notation. The matrix entries are in GPa unit. The estimated numerically error is indicated in parentheses. Symmetry-equivalent entries (e.g. C12 and C21) were calculated individually, resulting in some differences. However, these differences fall well with the given error ranges. Moreover, the variations between unconnected matrix entries are small. Accordingly, the bulk elastic tensor corresponds to the hexagonal or even cubic materials. From the elastic stiffness tensor, an approximate value for the bulk modulus of an isotropic body can be calculated. Using the method according to Reuss [129], obtained a shear modulus of $G = 54$ GPa, a Poisson ratio of $\nu = 0.22$ and a bulk modulus of $B_0 = 187.5$ GPa.

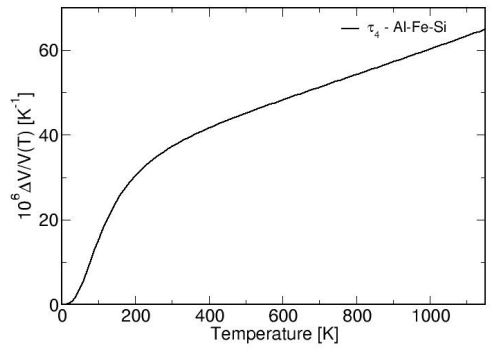

Figure 3.14: Thermal volume expansion coefficient $\alpha = \Delta V/V$ of Al_3FeSi_2, as calculated by the quasiharmonic approximation at 300 K, $\alpha = 37 \times 10^{-6}$ K^{-1}. [12]

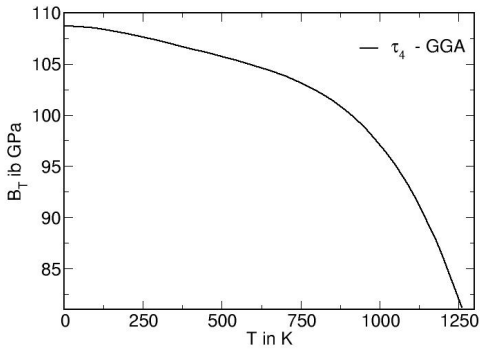

Figure 3.15: Calculated bulk modulus of Al_3FeSi_2 between 0 K and 1300 K.

$$C_{ij} = \begin{bmatrix} 315.3 & 151.9 & 198.5 & 0 & 0 & 0 \\ 151.9 & 210.9 & 136.6 & 0 & 0 & 0 \\ 198.5 & 136.6 & 351.2 & 0 & 0 & 0 \\ 0 & 0 & 0 & 50.2 & 0 & 0 \\ 0 & 0 & 0 & 0 & 49.1 & 0 \\ 0 & 0 & 0 & 0 & 0 & 51.2 \end{bmatrix} \tag{3.3}$$

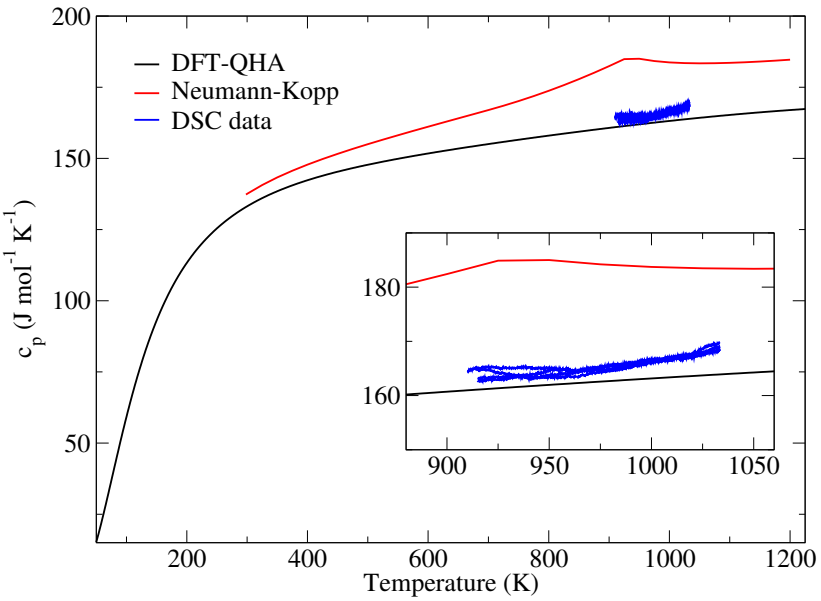

Figure 3.16: The c_p of τ_4 - Al_3FeSi_2 calculated using DFT-QHA (black), and the Neumann-Kopp rule (red). Several DSC measurements in the temperature range 930-1030 K, blue lines, in magnification [12].

No experimental data are available for the thermal expansion coefficient, but the calculated value falls within the expected order of magnitude. The calculated c_p and DSC measurements are in good agreement at high temperature (900-1000 K) and represent a substantial improvement over the application of the Neumann-Kopp rule with elemental data. Although between 300-600 K temperature range the N-K rule is in good agreement with the DFT-QHA calculation, though there are substantial differences around 900 K. The Neumann-Kopp rule is unsuccessful completely qualify the heat capacity. In particular, the matter of melting constituents, which undermine the Neumann-Kopp c_p at high temperature, is avoided by the DFT calculations. Applying these data in phase diagram calculations will improve the assessment of the Fe-Al-Si system.

It was shown that such calculations could be used for extrapolation of thermodynamic functions in a CALPHAD type modelling. In spite of the possible composition dependence of the experimentally determined heat capacity of the disordered Al-Fe phases, where a heat capacity valid in the short temperature range. The theoretical method is approved to use in a CALPHAD type modelling via ignoring the order/disorder transformation. Without further information about the nature of this particular structural change, no reliable CALPHAD prediction of that reaction can be made. For example, it is not always clear if this type of transformation is first or second order.

Chapter 4

Hercynite formation in a solid state reaction at the Al_2O_3-iron interface

The phase formations within a system can be discussed in terms of the thermodynamical properties. On the other hand, one can examine surfaces and interfaces, which are the most favourable for the filter systems under investigation. In this chapter presented the discussion of the formation of hercynite at the interface of the ceramic Al_2O_3 based filter and a metallic melt uses the DFT calculations. In particular, a direct interface reaction of a ceramic and a metallic melt is not favoured. However, an indirect reaction likely occurs resulting in the formation of hercynite because of reactive FeO. Studies of used ceramic filters have recorded captured oxide, and iron particles on the ceramic filter surfaces. In particular, they have seen the formation of spinel $FeAl_2O_4$ (hercynite) [29]. To achieve a high filtration efficiency, the particles from the melt need to be rather strongly attached to the filter surface, which often occurs by sintering processes. Arc-melting experiments have producing hercynite from iron and alumina [130]. Here, shown the selected solid state reactions of corundum (Al_2O_3) with iron which may occur at a ceramic filter and metallic melt interface calculated. The enthalpy as a function of pressure for several compounds in the Al–O–Fe system considered. This allows the discussion of chemical reactions in relation to the enthalpy differences between the starting and resulting compounds. The enthalpy calculation was done for structures like FeO, $FeAl_2O_4$, Fe_2AlO_4 and $FeAlO_3$. The calculation for Al_2O_3 structure is included for its three different phases α, κ, γ. A precondition for quality steel is to necessary reduce the oxygen content in the melt. A long-known way to achieve this is the addition of aluminium or silicon to the melt, which forms very stable oxides. These oxides are later enclosed as small particles in the steel matrix [20]. Such particles can, however, also enhance crack formation, and lower the steel quality. An efficient filter should remove the particles from the melt by attaching them to the filter surface, not just attractig them. The formation of the

spinel phase could provide a substantial contact between the filter surface and loose particles on top of it.

4.1 Crystal structures

4.1.1 Al_2O_3

The stable phase of Al_2O_3 is corundum (α - Al_2O_3), which has a rhombohedral space group symmetry R$\bar{3}c$. There are six metastable phases of Al_2O_3. The thermal transformation of the primary substance to the corundum phase includes an evolution of several metastable phases. For instance, between *Gibbsire* substance to corundum there are two metastable phases $\chi \rightarrow \kappa$, the *Boehmite* phase transitions through $\gamma \rightarrow \delta$ to corundum, and the *Bayerite* first transitions appears from $\eta \rightarrow \theta$ metastable phases before becoming corundum. Metastable phases can form under favourable conditions.

The κ - Al_2O_3 structure is orthorhombic in the space group P$na2_1$ [131], which applies to the structure type of $FeAlO_3$. That is significant since κ - Al_2O_3 could be predisposed to Fe substitution. The γ - Al_2O_3 is a defect spinel structure with aluminium vacancies in space group $Fd\bar{3}m$.

All Al_2O_3 phase structures can be character used by layers of Al-O polyhedra with different stacking sequences. The stable corundum accommodates only Al-O octahedra, whereas γ and κ accordingly octahedra and tetrahedra crystal type. The links between the various polyhedra also describe the different crystal structures. In corundum, some polyhedra share corners (1 shared atoms), others have shared edges (2 shared atoms), and others have full shared faces (3 shared atoms). In the case of κ and γ metastable phases, only corners and edges (2 shared atoms) are shared. For a model of the γ - phase, it is substantial to know the location of the vacancies. A DFT study [132] concludes that the lowest energy structures contain vacancies at octahedral sites and this model is presented in the particular calculation.

4.1.2 FeO

FeO is a ferrous oxide which contains Fe^{2+} and has the mineral name 'wuestite'. Wuestite forms exclusively under compressing conditions. Otherwise, iron oxides form as Fe_2O_3 ('hematite') and Fe_3O_4 ('magnetite') compounds. Under normal conditions its composition is not stoichiometric, because of the formation of Fe^{3+} [133]. Steel casting due to the low concentrations of oxygen. The formation of Fe^{3+} [20], is frequently found in forming a fcc rock-salt type crystal structure. The low-temperature phase is reportedly antiferromagnetic [133].

In this calculations, antiferromagnetism is introduced through symmetry lowering and the model is fully stoichiometric. The result is, in accord with experiments, an antiferromagnetic metal.

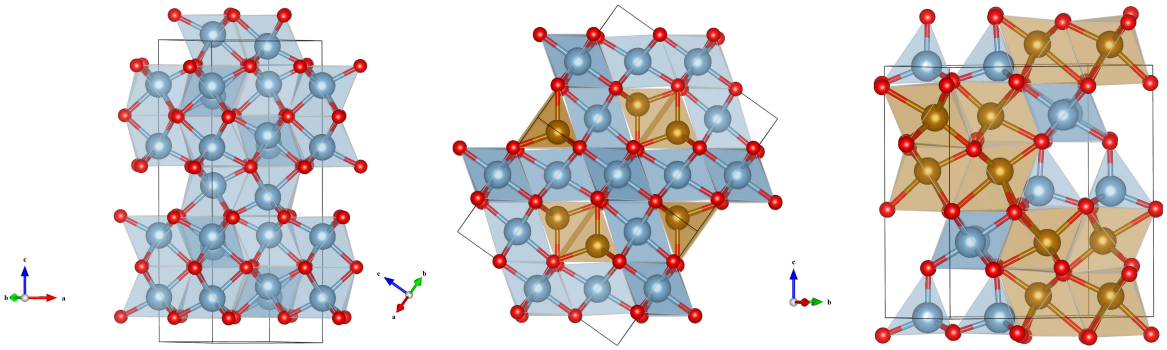

Figure 4.1: Three of the discussed alumina and Fe-alumina structure types, with the layered structure and coordination polyhedra emphasized. Left: corundum, middle: spinel ($FeAl_2O_4$), right: $AlFeO_3$ [15].

4.1.3 Al-Fe oxides

The spinel $FeAl_2O_4$ reportedly forms during the filtering process [134], and it has a mineral name 'hercynite'. The chemical composition specifies Fe in oxidation state +2. Fe prefers the tetrahedral and Al the octahedral sites of the spinel. A small degree of site disorder is expected [135]. The modelled structure has ideally ordered sites and ferromagnetism is included for Fe. It is found to be a metallic conductor.

The spinel structure Fe_2AlO_4 has the sites exchanged, which is an unlikely situation because Al favours the octahedral sites [136]. However, high Fe concentration might encourage Fe_2AlO_4 formation. In Walsh et al. [136], Fe_2AlO_4 is proposed as an inverse spinel, while in the conforming calculation assumes a normal spinel structure, as found in the literature [137].

As a second mixed oxide the complex material $FeAlO_3$ was considered. It crystallises in the orthorhombic space group $Pna2_1$ [138]. It also presented as ferromagnetic and associated with multiferroic behaviour [139]. This phase is isostructural with κ - Al_2O_3. Consequently, Fe is in oxidation state +3 here. Unlike in $FeAl_2O_4$, Fe prefers an octahedral coordination in this compound, while the Al sites are either an octahedral or tetrahedral environment. There is the high complication. Therefore, the crystal has not been an optimise, and the magnetism was carried out due to the antiferromagnetic approximation.

Formation of $FeAlO_3$ in the solid state is unlikely because its melting temperature is below that of iron. In fact, of all compounds discussed here, only Al_2O_3 and hercynite are solid above the melting temperature of iron.

The bcc ferromagnetic ground-state structure considered for Fe. If Al_2O_3 decomposes, it is likely that Al dissolves in the steel melt. Thus include an intermetallic AlFe compound. AlFe crystallises in the primitive cubic CsCl structure type. This material is reported as paramagnet [140]. Because the magnetic moment of iron should not be neglected, it is modelled here as an antiferromagnet.

4.2 Results and Discussion

The DFT calculations were done using the WIEN2k Linear Augmented Plane Wave package [141]. The atomic core electrons are included in the calculations using a basic set of local atomic orbitals. The core orbitals were restrictive to a preset muffin-tin radius around each atom site. The valence orbitals can extend outside that radius, where they expand in a plane-wave basis. All orbitals with energy above a separation energy threshold are defined as valence electrons. Additional local basis functions within the muffin-tin radius help to enhance their description in the near-core region.

The cutoff energy for the plane-wave basic functions was adjusted so that $R_{MT}k_{max} = 8$. The muffin-tin radii had to be reduced such that no overlap can occur during the energy-volume calculations. In most cases the identical values were used. An exception has to be made for the orthorhombic phases, which have a higher packing density than other structures. The total energy converges at a level of 5 meV for each phase have been achieved for a chosen k-point grid. The PBE-GGA [124] exchange-correlation energy was applied here. In Fe-containing phases, the magnetism accounted for using a scalar spin-dependent electron density.

The total energy minimum was searched by modifying the crystal volume and computing the corresponding energy. The space group symmetry was fixed, but the atomic sites were refined whenever it was computationally feasible. Since $FeAlO_3$ has a complex structure, we made an initial structure relaxation using the pseudo-potential DFT code Quantum Espresso [46] but then fixed the geometry.

The calculated energy-volume data were fit to a Birch-Murnaghan equation of state (4.1) for solids [142] using the utilities of the WIEN2k package.

$$E(V) = E_0 + \frac{9V_0B_0}{16}[(\frac{V_0}{V})^{\frac{2}{3}} - 1]^3B_0' + [(\frac{V_0}{V})^{\frac{2}{3}} - 1]^2[6 - 4(\frac{V_0}{V})^{\frac{2}{3}}] \tag{4.1}$$

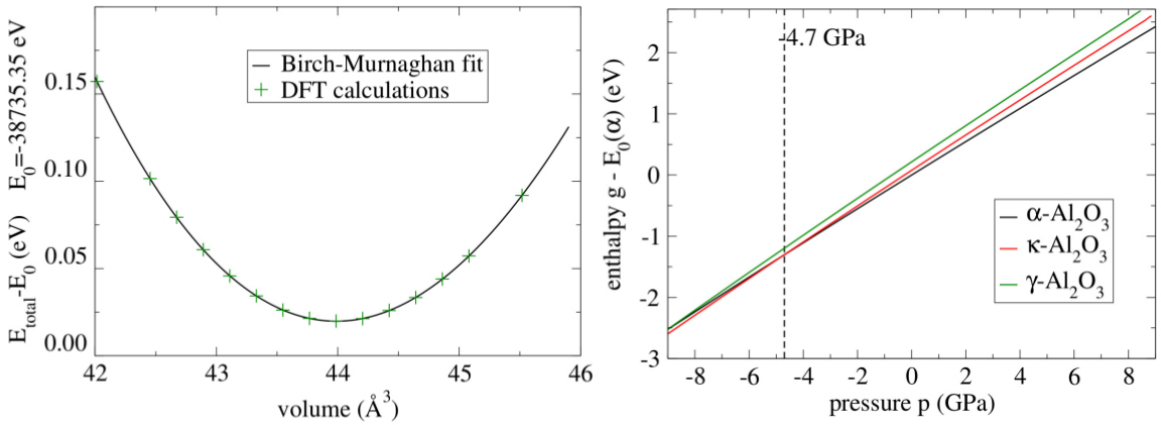

Figure 4.2: Left: Energy–volume curve for corundum. The values correspond to one formula unit of Al_2O_3. The line is calculated from the Birch–Murnaghan equation fitted to the calculated DFT data. Right: Enthalpy g(p,T=0) for α, γ and κ - alumina. [15]

This equation applies strictly only for cubic materials. However, it is often also used for other materials. In all cases discussed here, the standard deviation of the fit is below 10^{-5} eV for 15 calculated volume points. The Birch-Murnaghan equation thus describes the determined volume-energy dependence fairly well. The Figure 4.2 shows the fit determines the four parameters of the equation: the isotropic bulk modulus B, its pressure derivative $\partial B/\partial p$ and the equilibrium volume V_0 and total energy E_0.

The minimum total energy E_0 represents the thermodynamic free enthalpy $F(V, T = 0)$ at 0 K. The pressure-dependent Gibbs enthalpy $G(p, T = 0)$ can be calculated by Eq. 2.82 and the $p = -\partial F/\partial V$, where is taken the Birch-Murnaghan energy (4.1) as F.

	Structure	B (GPa)	V_0/f.u. (Å^3)	$\partial B/\partial p$
α - Al_2O_3	Rhombo.	230	44.0	4.2
γ - Al_2O_3	Monoc. C	210	47.6	4.1
κ - Al_2O_3	Orthor. P	199	46.5	4.0
$FeAlO_3$	Orthor. P	170	50.5	4.1
$FeAl_2O_4$	fcc	189	69.6	4.1
Fe_2AlO_4	inverse-spinel	170	71.4	4.2
FeO	NaCl	172	20.2	4.2
Fe	bcc	199	11.3	5.4
FeAl	CsCl	175	23.7	4.1

Table 4.1: Calculated DFT data: V_0 is the equilibrium volume at zero pressure per formula unit from the DFT calculation and data found in the literature, B is the bulk modulus.

Table 4.1 shows the data resulting from the DFT calculations. The found experimental values are compiled in Table 4.2.

	GGA DFT		Experiment	
	B (GPa)	V_0/f.u. (Å^3)	B [GPa]	V_0/f.u. (Å^3)
α - Al_2O_3	243.4	42.8 [143]	258	42.5 [144]
κ - Al_2O_3	224	45.2 [143]	–	49.3 [145]
$FeAl_2O_4$	–	–	191	66.0 [146]
FeO	169	19.7 [147]	154	19.9 [148]
Fe bcc	185	11.6 [149]	166	11.8 [150]
FeAl	181	23.9 [151]	138	24.6 [152]

Table 4.2: Theoretical and experimental data found in the literature.

The calculated elastic properties such as B are usually too high when lattice defects and the microstructure play a significant role. The carried out bandgap is smaller than the experimental value because the DFT does not determine the excitation energy precisely. The difference between calculated and experimental volume is related to the type of included exchange-correlation approximation. For GGA, the calculated volume is expected to be too high. In turn, experimental volumes may include temperature and impurity effects. Although the correspondence to experimental data is thus in most cases not exact, the comparison to other DFT calculations delivers an excellent model for material behaviour.

The calculated properties of the alumina phases collected in Table 4.1. There is a notable difference in the volume per formula unit, V_0. The stable corundum has the lowest volume. It has been observed in coatings of κ - Al_2O_3 produced by a CVD process, that the transformation to the α-phase causes a compression of the material, which leads to the formation of cracks [153].

The total energy differences to corundum are small: 0.08 eV for κ and 0.22 eV for γ. From κ - to γ - Al_2O_3, the total energy increases along with V_0, and the band-gap decreases. The other properties differ by only 10 - 20 percent. Thus the enthalpy-pressure curves Figure 4.2 of all phases are close together.

The calculated phase transformations between α, γ and κ occur at negative pressure, *i.e.* expansion of the lattice. This condition could be achieved through *chemical pressure*, for instance, caused by vacancies that stretch the surrounding lattice. Similarly, thermal expansion widens the lattice. The significant effects of thermal motion are, however, not included in calculations. Although this is in principle possible at least in approximation, many computations needed so far beyond the estimates presented here.

The experimental observations indicate phase formations on the filter surface. Using the calculated total energies, the energy differences between several possible phases in their ground state calculated. This difference is determined by the energy gain from chemical bonding only because thermal effects are not included. The considered reactions shown

#	Reaction	ΔE (eV)	ΔE_c (eV)	ΔV (Å^3)
1.	Al_2O_3 + 2 Fe ↔ $FeAlO_3$ + FeAl	3.6	4.6	8.8
2.	Al_2O_3 + 5/4 Fe ↔ 3/4 $FeAl_2O_4$ + 1/2 FeAl	2.1	2.0	6.6
3.	Al_2O_3 + 11/4 Fe ↔ 3/4 Fe_2AlO_4 + 5/4 FeAl	4.3	4.3	9.7
4.	Al_2O_3 + 3 FeO ↔ 2 $FeAlO_3$ + Fe	-1.8	-0.2	7.1
5.	Al_2O_3 + FeO ↔ $FeAl_2O_4$	-0.2	-0.5	5.4
6.	Al_2O_3 + FeO + 2 Fe ↔ Fe_2AlO_4 + FeAl	2.8	2.5	8.5
7.	Al_2O_3 + 5 FeO ↔ 2 Fe_2AlO_4 + Fe	-3.2	-4.4	9.5
8.	Al_2O_3 + 5 Fe ↔ 3 FeO + 2 FeAl	8.9	9.4	7.6

Table 4.3: Energy differences ΔE for Reactions $A \leftrightarrow B$ calculated as: $\Delta E = E_B - E_A$ using the equilibrium zero pressure total energy from DFT calculations. Negative values indicate preference of the B side. In ΔE_c, the heat of fusion is included for the presumably liquid phases (Fe, FeAl, FeO, $FeAlO_3$). $\Delta V = V_B - V_A$ is the volume difference of the ground state phases [15].

in Table 4.3 of Al_2O_3 with Fe (rows 1 - 2, 8), and with FeO (rows 3 - 4). The energies are calculated per formula unit of Al_2O_3 to make them comparable. Two Fe-Al oxides are considered as reaction products.

Only the reaction of Al_2O_3 with FeO results in an energy gain, producing hercynite or $FeAlO_3$. Although it is even larger for $FeAlO_3$, this compound does crystallise only below the melting point of iron. The reason for the energy gain here seems to be the instability of FeO, which shown in the last row of Table 4.3, the formation of FeO and Al_2O_3 are directly compared. As far as know, FeO is not a component of the melt. Instead, can be considered FeO as an approximation for oxygen dissolved in the iron melt.

The possible oxygen sources are, first, solute gas and second, dissolution of Al_2O_3. This oxygen sources should only deliver a minuscule concentration of oxygen in the melt, for the addition of extra aluminium is dedicated to binding oxygen by forming Al_2O_3. The incorporation of dissolved Al_2O_3 in hercynite would be equivalent to the unfavourable reaction in row 8. Therefore, the formation of hercynite needs extra oxygen from external (non-alumina) sources.

Replacing corundum by the metastable alumina phases adds the energies calculated in section 4.1.1 to the alumina side. The shifts of energy balanced slightly to the other side. If metastable phases are present on the filter surfaces, they will be the preferred reaction sites. However, the overall change in energy is too small to modify the energy balance in Table 4.3 significantly.

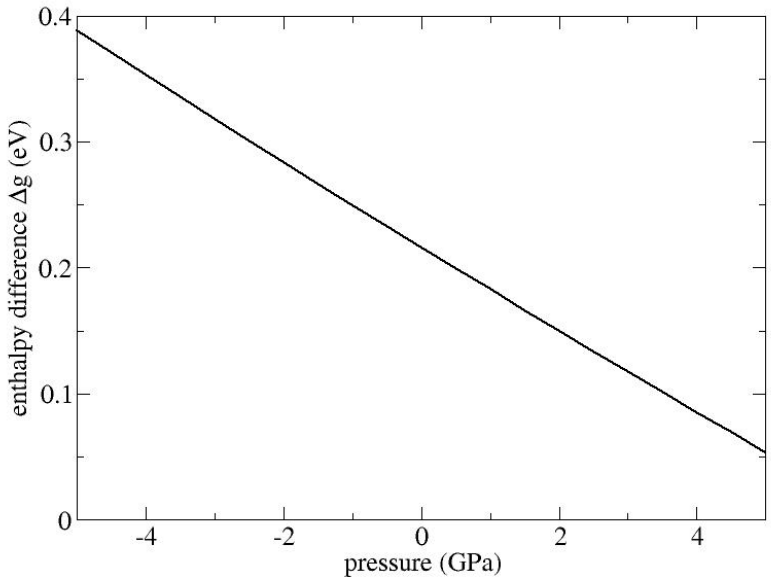

Figure 4.3: Enthalpy g(p,T=0) for the reaction $Al_2O_3 + FeO \leftrightarrow FeAl_2O_4$.

The Table 4.3 also contains information about the change in volume for each of the reactions at zero pressure. The negative values indicate that all reactions cause expansion. As can be seen from the $g(p)$ plot of a reaction shown in Figure 4.3, increasing pressure lowers the energy gain, thereby destabilising hercynite.

Results show that the formation of the hercynite ($FeAl_2O_4$) phase beginning from alumina (Al_2O_3) and Fe is not precisely possible in thermodynamic equilibrium. The experimental reports, finding hercynite on the surface of alumina filters for steel melts desire another explanation. The simplest possibility includes oxygen enrichment of the melt from the air or the melting process. Additional oxygen will react with alumina forming hercynite. By replacing Al with Fe^{3+}, this compound can also contain higher-oxidised Fe, which may form at high oxygen concentrations.

Other formation paths could rely on non-equilibrium conditions. One possibility would involve different solution reaction constants: if the solubility of hercynite was smaller than that of Al_2O_3, it could be formed around all Al_2O_3 surfaces in contact with the melt. Still another option is the diffusion of Fe into the alumina lattice and subsequent phase formation during quenching. This scenario appears likely because the alumina and Fe-alumina phases share common crystal structures, with Fe replacing Al. If diffusion enabled phase formation, one would expect more Fe replacement to be found in the rhombohedral corundum (as in sapphire). Also, diffusion and cooling could result in $FeAlO_3$, having a higher energy gain than hercynite.

For the filter process discussed, a certain degree of phase formation is necessary to act as 'glue' between the filter surface and adhering particles. Also, the binding of oxygen in chemical reactions is desirable. The filter process itself seems not to be correlated strongly with the filter material involved.

Chapter 5

Examination of the surface energy of α-Al_2O_3

The investigation of the original substance's surface phenomena is of great importance in filtration processes since the surface of the filters due to the filtration process are always in contact with the alloy melt. Therefore, the study of Al_2O_3 surfaces is essential for this project. Earlier in 1830, C.F. Gauss represented the idea of surface energy. Later in 1877, W. Gibbs characterised surface energy phenomena by the fundamentals of classical thermodynamic theory. Then Lord Rayleigh (formerly named I. W. Strutt) proved the existence of waves located at the surface of continuous elastic media. The problem of minimising the surface energy of a finite anisotropic solid to find its equilibrium shape was solved by G. Wulff (1901). The development of surface chemistry continued by I. Langmuir, who inspired W.L. Bragg in 1913 to discover the crystalline nature of various surfaces. I. Langmuir advanced a theory of heterogeneous catalysis and adsorption kinetics, and besides, he supplied a model of thermionic emission. The breakthrough in the study of crystal surfaces as a subject of crystal growth was developed by I. N. Stranski (1928) and M. Volmer (1939). At the beginning of the 1950's, there were already many publications on this subject. However, progress in the understanding of surface physics was hampered by several problems until recently. These problems are mainly due to the structural and chemical characterization of surfaces. The chapter presents only Al_2O_3 crystal surfaces, excluding study alloys or insulator surfaces.

Essential aspects of material sciences and engineering depend on the crystal structure, which defines its intrinsic material properties. Techniques, for instance, X-ray diffraction (XRD), and Transmission Electron Microscopy (TEM) are based on crystallography. Accordingly, a concept of the basics of `crystal structures`[1] is of paramount importance.

[1] Crystal structure - periodic arrangement of atoms: definite repetitive pattern

The crystalline structure is an orderly and periodic arrangement of atoms. It is characterised by sharp transition temperature called the melting point of the liquid. The lowest energy state of a solid is the crystalline state [154]. The unit cell of each crystal structure is the smallest structure which repeats itself over whole crystal structure. Widespread types of unit cells are faced-centred cubic (FCC), body-centered cubic (BCC) and hexagonal close-packed (HCP). The lattice parameters parallelepipeds are defined by the lattice vectors. The orientation of a plane in the lattice is specified by *Miller indices*. Miller indices, which are named as *(hkl)*[2], are a notation to describe certain crystallographic planes and an infinite set of equivalent planes in a material. The interplanar spacing is the perpendicular distance between two successive planes in a family {hkl}, which is commonly indicated as d_{hkl}. The general formula is given as:

$$d_{hkl} = \frac{1}{\sqrt{\frac{h^2}{a^2} + \frac{k^2}{b^2} + \frac{l^2}{c^2}}} \tag{5.1}$$

For the cubic system, when all of the faces of the cube are equivalent, the indices are the same in any plane. Nevertheless, in the case of the hexagonal system, which corresponds to the Al_2O_3 structure, the different planes have different inter-planar spacing. The six prism faces for example have indices (1 0 0), (0 1 0), ($\bar{1}$ 1 0), ($\bar{1}$ 0 0), (0 $\bar{1}$ 0), (1 $\bar{1}$ 0), which are not same. To address this, a fourth axis (a_3) opposite to the vector sum of a_1 and a_2 is used, and an appropriate fourth index i is used, defined ($hkil$) where $i = -(h+k)$.

5.1 Surface and Surface Energy

The α-Al_2O_3 surfaces are highly studied metal oxide surfaces which has the wide variety of technological applications and gives us the conception to investigate it as a prototype material for more fundamental studies. It is a ceramic with a broad range of phase transitions. Ceramics, due to their ionic character, have a poor wettability by metal melts, and particularly α-Al_2O_3 is used for filtration without pressure. The goal is to control the processes that take place during filtration at the α-Al_2O_3 surfaces and to obtain a quantitatively qualitative understanding of the nature of interaction with adsorbates due to the filtration process.

At first, one has to discern between a real surface and the cleavage plane. A surface that can be derived directly from the crystal structure may be formed only by cleaving the crystal. Then, the new boundary has to be included to cause the relaxation of surface atoms. Cleaving a crystal means cutting it along a crystal net plane. In contrast to that, the propagation of cracks in a material usually follows weak points such as grain boundaries or lattice faults.

[2]Lattice directions are in direct space and are denoted by [ ] brackets. Directions of a form (also called family) denoted by {} brackets are the lattice planes that have the same characteristics.

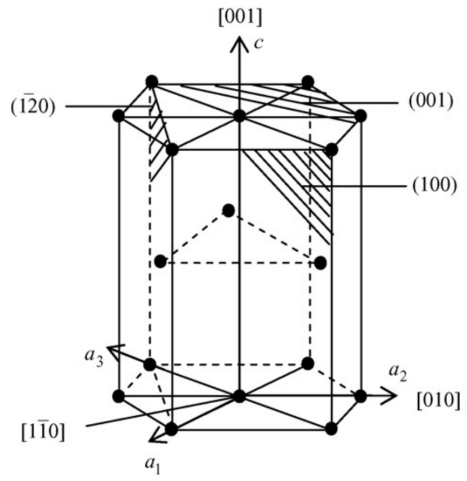

Figure 5.1: Bravais lattices of hexagonal system where $a = b \neq c$ $\alpha = \beta = 90^o$ and $\gamma = 120^o$ [16].

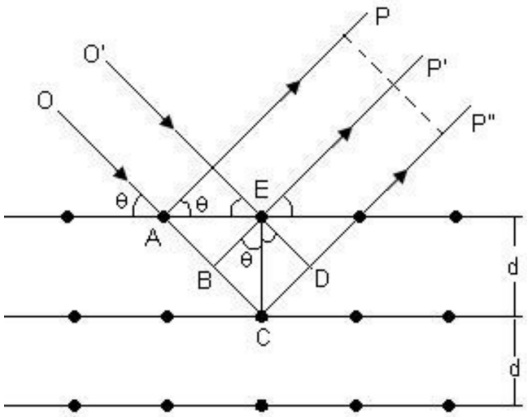

Figure 5.2: Equidistant parallel planes of atoms with the inter-planer spacing d_{hkl} [17].

In all cases where the surface is in contact with the environment, the chemical composition of the surface and the outside are interdependent. In addition, the atomic structure of the surface can adapt to the environment by reconstruction, which is driven by surface diffusion. The resulting surface structure is, in general, a superstructure of the bulk crystal. The chemical medium can cause a separation of the surface composition from the bulk, as well as adsorption on the surface. If the diffusion rates through the surface are high, then the volume region with altered chemical composition may also grow into the crystal.

So far, none of the parameters listed are directly proportional to the calculated surface energies. For instance, the elastic modulus (Young's modulus) perpendicular to the surface is isotropic for all (hk0) lattice planes in the hexagonal cell, but the surface energies are not. Surprisingly, the number of broken bonds has no simple regular relation to the surface energy. However, several authors have presented expressions for different types of crystal surfaces. The idea of those methods is that each surface atom has neighbouring atoms. Therefore, there are attractive interaction forces. Atoms on the surface often perceive a net force pointing toward the inside of the bulk. Particularly, it can be considered that a surface atom has higher potential energy than one from bulk. The energy differences should be overcome in the case when one wants to bring an atom from bulk on the surface. Accordingly, this energy difference is called the surface energy (γ). For a given surface orientation, γ represents the energy per unit area due to the certain oriented surface. A straightforward approach to roughly estimate the surface energy is to determine the number of broken bonds, which appear via creating a surface area (A) by cutting a crystal lengthwise along a particular

crystallographic plane and multiplying it with the energy per bond. This kind of approach appears to be valid for covalently bonded crystals, which considers no long-range interactions have to be taken into account. The theoretical determination of the surface energies of the clean surfaces often arise from DFT calculations [155–159]. The experimental determination of the absolute surface energy value is difficult, and as a result, it remains a challenge. There are methods for theoretically estimating the surface energy from broken bonds. In 1993 Desjonquères and Spanjaard [160] described the surface energy and broken bond connection for pure metals and semiconductors. They consider the surface regions about 20 Å around the last atomic plane, i.e., including the first three or four atomic layers since beyond the examined region the electronic density on the vacuum side substantially vanishes and attains its bulk behaviour on the solid side. In equation (5.2) Desjonquères and Spanjaard [160] express the surface energy as:

$$\gamma = \left(1 - \sqrt{\frac{z_s}{z_b}}\right) E_B \tag{5.2}$$

where γ is surface energy, E_B is binding energy, z_s the coordination number of surface atoms and z_b the coordination number of the atom in bulk.

Haiss [161] considered materials with covalent bonds as a single element material structure, and he represented the surface energy by:

$$\gamma = \left(1 - \frac{z_s}{z_b}\right) E_B \tag{5.3}$$

Later Jiang et. al. [162] assumed that the surface energy contains not only the first nearest neighbour interactions but also the next-nearest neighbour interactions. Equations 5.2 - 5.3 should be rewritten for metals:

$$\gamma = \left(\left[2 - \frac{z_s}{z_b} - \sqrt{\frac{z_s}{z_b}}\right] + \beta\left[2 - \frac{z_s^{'}}{z_b^{'}} - \sqrt{\frac{z_s^{'}}{z_b^{'}}}\right]\right) \frac{E_B}{2+2\beta} \tag{5.4}$$

where the prime denotes the next nearest neighbour's coordination number of surface atom $z_s^{'}$, in the bulk $z_b^{'}$ and β shows the total bond strength ratio between the next-nearest neighbour and nearest neighbour.

The prediction of crystal morphology from structural data can give an understanding of the crystal growth. Hartman and Perdok [163] put forward a theory that the morphology of a crystal governed by chains of strong bonds running through the structure. These chains define within stable forces which lead to the growing of crystal and its morphology. Consequently, can be assumed that the growth rate of any (hkl) plane, which determined by those forces, is

directly proportional to its binding energy. Hartman and Bennema [164] offered arguments to justify this assumption and use the binding energy of (hkl) to produce a surface energy:

$$\gamma = \frac{NE_{bind}d_{hkl}}{2V} \tag{5.5}$$

in which N represents the number of formula units, V is a primitive unit cell volume and d_{hkl} corresponds the interplanar spacing of the lattice plane (hkl).

Above presented equations 5.2, 5.3, 5.4 and 5.5 do not work in the case of Al_2O_3. As known, the Al_2O_3, which is under investigation as a substance of filters, has mixed covalent and ionic bonds and the percentage of the type of bonds depends from the alumina's and oxygen's electronegativities.

DFT surface energy calculations are, often the most reliable method. The first calculations of surface energies via DFT were done by Needs [165] for the Al (111) and (110) plane using a supercell with a nine layer thick slab and with six layers of vacuum. To obtain the surface energy γ per unit area, the following equation was used:

$$\gamma = \frac{1}{2A}\left[E_s - \frac{N_s}{N_b}E_b\right] \tag{5.6}$$

Where A represents the surface area, E_b is the free energy of primitive unit cell (bulk) and E_s refers to the energy per supercell with relaxed or unrelaxed atomic positions, as appropriate.

In a method introduced by Liu et.al. [166], one calculates the surface energy from the DFT results using the total (inner) energy $U(S = const., V = const.)$ for a given slab geometry. In their example, slabs of Al_2O_3 with different terminations were studied. The starting point is the free enthalpy for ($T = 0$, $p = 0$) and the Gibbs-Duhem relation:

$$G(\sigma, N) = U(N) - \sigma A \tag{5.7}$$

$$G = \sum_i N_i d\mu_i = -SdT + Vdp \tag{5.8}$$

where N_i in the number of moles of component i and $d\mu_i$ the slight increase in the chemical potential for given component.

$$\sigma = \left(U - \sum_i N_i\mu_i\right)A^{-1} = (U + SdT + VdP)A^{-1} \tag{5.9}$$

It also seems reasonable to subtract the total bulk energy for the bulk part of the slab. Then, the balance for the free enthalpy is:

$$G_{surf} = (U - E_{bulk}) - \sigma A = \mu_{ad} N_{ad} \tag{5.10}$$

If no adsorbed atoms are present, $N_{ad} = 0$ and it follows:

$$\sigma A = (U - E_{bulk}) \tag{5.11}$$

for the "bulk-composition" surface. This formula is frequently used for DFT calculations of surface energies. With adsorbed atoms, their chemical potential is needed. In thermodynamical equilibrium, the μ of each element is the same in all phases. In the case of Al_2O_3 in equilibrium with gaseous oxygen, the chemical potential for oxygen can be approximated by the formula for the ideal gas:

$$\mu_{O_2} = \mu^0_{O_2} + RTln(p_{O_2}/p) \tag{5.12}$$

Where $\mu^0_{O_2}$ is the binding energy of the oxygen molecule. This energy is determined from a mixture of experimental and theoretical values [166]. The formation energy of some oxides calculated with DFT have been compared with measurements [167]. It was found that the DFT values need to be corrected by a constant shift because of the inaccuracy of the calculated oxygen binding energy. A database with calculated formation energies applying such a correction is available on the internet (www.materialsproject.org). Interface formation is thus modelled as a process in two steps: first, a surface with bulk composition is formed, and then a reaction with the environment changes the composition. If Al_2O_3 is dissolved at the surface, its formation energy thus adds to the energy balance. Consequently, the Al-depleted surface obtains the highest surface energy at ambient conditions.

The bulk energy is calculated according to the number of Al atoms in the slab [168]. This method is reasonable because the environment does not contain Al and it is expected that Al does not leave the crystal. But in actively oxygen-depleted surfaces, the surface is made from a layer of Al. In this case, the Al surface layer has surely a different binding energy than in the bulk. The bulk energy subtraction thus fixes the Al binding energy to a wrong value. Consequently, the Al-terminated surface obtains a large surface energy, and the oxygen termination is found as favourable.

However, there is one point in the method discussed above that remains doubtful. For example, it does not explain why "bulk composition" surfaces along different crystal orientations or with different termination have different surface energies. Moreover, it is not

possible to discuss how the stability of these surfaces is controlled by the outside chemistry. The main problem is the method used for subtracting the bulk energy. The bulk energy can be constructed from the sum of the chemical potentials and the formation energy of Al_2O_3.

5.1.1 Calculation of surface energies via DFT

The calculation of the Al_2O_3 surface energy was done using slabs with sufficient thickness of bulk and vacuum via QUANTUM ESPRESSO code [46]. The total energy of different planes and various termination of the (0001) plane were taken in to account for the surface energy. Assuming that the bulk and surface energy are the same for slabs with different termination and n, m are the number of formula units in the slab, the surface energy contribution will be S':

$$S' = mE_n - nE_m \tag{5.13}$$

Afterwards, dividing S' into the two times multiple the surface area the surface energy can be obtained.The differences in the calculated bulk energies depend on the slab thickness. These differences are caused by displacements of atoms in the inner part of the slab and should disappear for larger slab thickness. The slight differences in the relaxed in-plane lattice constants are another indication of this problem.

5.2 Analysis of surface geometry of corundum - α Al_2O_3

The crystal structure type and its atomic arrangement of characterising α-Al_2O_3 - corundum have been given as a rhombohedral, D^6_{3d} - space group symmetry system. It is a highly insulating material characterised by mixed ionic and covalent bonding with a large band gap energy [169]. Each Al atom is encircled by six oxygen atoms, where each three of these are six oxygens at the corners of equilateral triangles. The symmetry of crystal structure of Al_2O_3 is threefold, and the oxygen ions have what can be considered as hcp stacking, with the Al^{3+} ions occupying two-thirds of the octahedral interstices (balancing the charge).

At each lateral triangle, which has the triangle side length equal 2.5 Å, at its corners sites O atom bonded to an Al atom by strong Al - O 1.85 Å bond. In the case when the triangle side length is 2.8 Å and three other oxygen with weak 1.97 Å bonds [170]. In Al_2O_3, the polyhedral has to share a triangle with the shared O at the corner of it. These types of the bonds have long bond length 1.97 Å. And next three oxygens make up the non-shared or free triangle, and the bond length has 1.85 Å.

The energy-band at the Brillouin zone shows the lower valence band from -36.4 eV up to the -26.9 eV [170], which is 9.5 eV wide. It corresponds to the O *2s* orbits (there is a

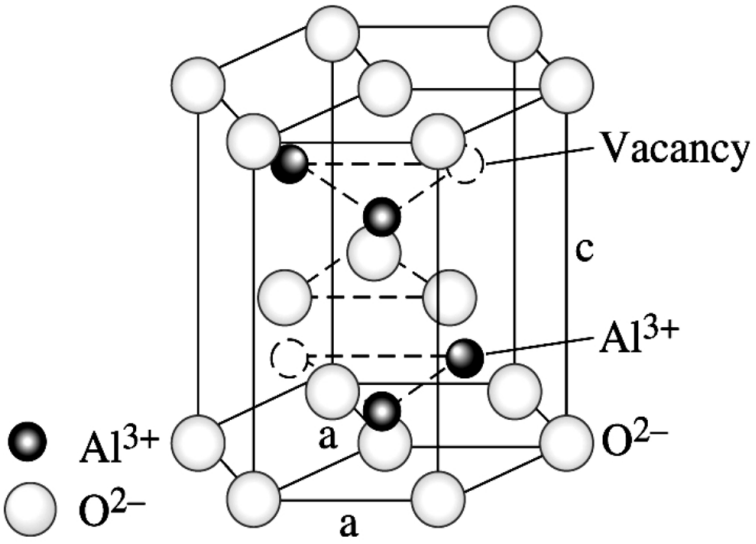

Figure 5.3: Corundum structure of α-Al_2O_3 which presents O in hcp and Al in 2/3 of the octahedral interstitial sites. It is perhaps the most widely used ceramic.

transition from the O *2s* lower valence band to the conduction band), and the lowest two bands formed from the combined bonds of Al 3*s* and O 2*s* orbits. The transfer of electron corresponds to transfer from oxygen to Al [170, 169]. Below at the -20 eV valence band, a maximum arising from the O *2s* lower valence band. The region between the upper and lower valence bands is referred to as an ionising gap. The hybridization of Al-O states can be seen in the upper valence band. The lower oxygen in *2s* bands are mixed Al and O ionic bands. These hybridised Al-O bonding orbital represent the covalent bonding in Al_2O_3 [169].

The pattern of the atoms or lattice points surrounding an atom or lattice point is unique for each crystal structural units and its modified rigid-ion model. This pattern represented a crystal structure called *coordination polyhedra*. The Al_2O_3 - corundum crystal structure is composed entirely of AlO6 octahedra. The alumina ions are in four- (Al(4)), five- (Al(5)) and sixfold (Al(6)) coordination. In the hexagonal unit cell, like α-Al_2O_3, number of atoms are twelve corner atoms $\times \frac{1}{6}$ shared by six unit cells + two face atoms $\times \frac{1}{2}$ + 3 interior atoms, in total six atoms. The stoichiometric primitive unit cell (bulk) contains 30 atoms.

A solid material's surface interacts with the environment. The quantity used to describe the surface characteristics from a thermodynamic point of view is the surface tension or surface energy. However, the usual meaning of surface energy is that of a surface in a vacuum. For material in contact with a particular environment, it must be replaced by the interface energy. This energy plays a key role in describing the surface adsorption and wetting.

In this chapter, several planes of α-Al_2O_3 are examined, using a density functional pseudopotential method. The calculation was done in the form of a slab within periodic

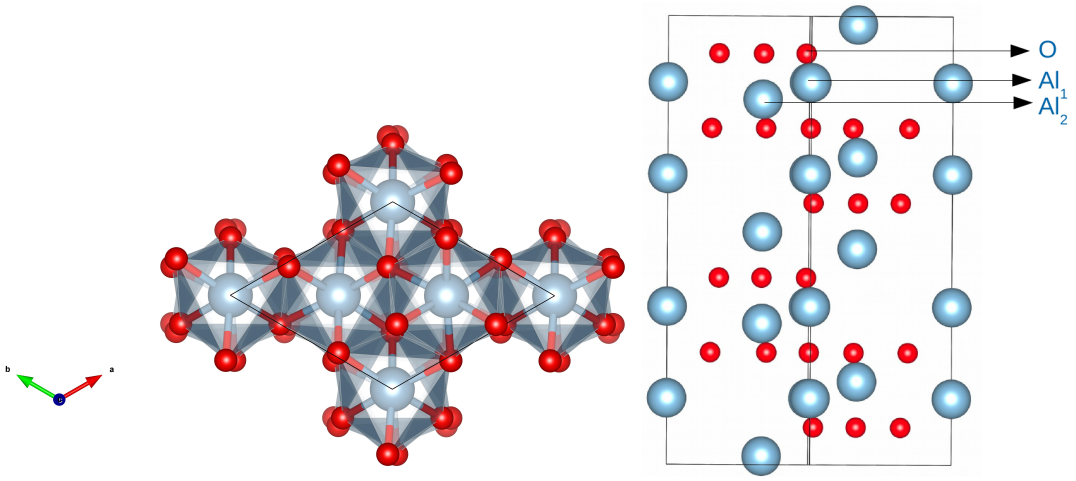

Figure 5.4: Top and lateral view of α-Al_2O_3 structure (0001) plane. The right hand side also illustrats the different atomic layers, which are present in the structure.

boundary conditions, consisting of up to nine layers of the stoichiometric Al_2O_3 units. Five different planes were examined and for two of them, various terminations of the surface calculated. The relaxations of the atomic positions were obtained. The main properties can be obtained from one calculated parameter and a good knowledge of material crystallography. The protected surface energies are in good agreement (less than 7% difference) with the results calculated by DFT with the slab-vacuum-slab method.

5.2.1 α Al_2O_3 (0001) plane

Here is given the examine of the surface plane (0001) - α - Al_2O_3 without considering reconstruction and adsorption effects. The model hence has the same atomic structure as the corresponding crystal net plane, but the atomic positions are allowed for relaxation. The (0001) surface plane of α - Al_2O_3 is well defined and assigned to the layered crystal structure perpendicular to the net plane. In chemical terms, it can be terminated by either an Al, O or a mixed Al/O layer. A six parallel (0001) planes of oxygen ions are required to build the Al_2O_3. By cleaving along the net plane, one can obtain either a symmetric single-Al and double-Al layer termination or the unsymmetric Al/O termination (see Figure 5.4). The symmetric single Al termination has been studied by many authors [171–174]. At this surface, the atomic relaxation in a vacuum causes an the inward displacement of the top layer, and the result is almost a mixed surface. The DFT treatment of a charged surface can be simplified by including an Effective Screening Medium (ESM) method, which is a classical charge model into the DFT calculation with using open boundary conditions (OPC) [175, 46].

Unsymmetric Al/O

The long-range electrostatic interaction between two separated surfaces in a supercell is compensated, but the additional potential causes a static potential shift along the slab. In this case, the optimisation of the atomic positions cause a displacement of all ions due to the electrostatic field of this potential, and the bulk structure is changed. This effect seems to decline with increasing slab thickness. It will occur for all kinds of unsymmetric surface slab models, which exhibit a change of the electrostatic potential in the vacuum region.

However, if the surface charges are compensated by the adsorbed molecules, then the internal and external fields may show a different character.

Symmetric single-Al and double-Al

For the single-Al surface model, it is known that it exhibits strong relaxation within the near-surface layers. The top Al is displaced toward the lower oxygen layer strongly, so that the equilibrium surface almost has a mixed Al-O character. This surface is formed by dividing an Al double layer. In Figure 5.5, the result of unrelaxed calculations of the total energy versus layer distance for the three terminations is shown. The crystal corresponds to the minimum at 0 deformations. The stress in a direction perpendicular to the plane is plotted as well, but these values depend strongly on the slab thickness. However, both the total energy and stress-strain diagrams show that the unsymmetric surface is the less favourable cleaving plane.

The surface - state bands of the ideal α-Al_2O_3 (0001) surface are produced mainly by the Al orbitals. The energy positions of these bands are strongly dependent upon Al-O distance and the effective charge of the surface aluminium. The bonds, which connect the surface aluminium to oxygen at the second layer, are found to have a considerable covalent character. It is expected that the spectrum of the A1(2p) core region can yield valuable information regarding the bonding at the surface. This result is within good agreement of the conclusion which was given by Ciraci et.al. [170], who claimed that the top Al atoms are covalantly bonded with the oxygens in the two layers below.

5.3 Results and Discussion

5.3.1 Surface energy

DFT calculations of surface energy were performed for various Al_2O_3 slabs with different surface orientations and terminations. A summary of the different planes geometries with

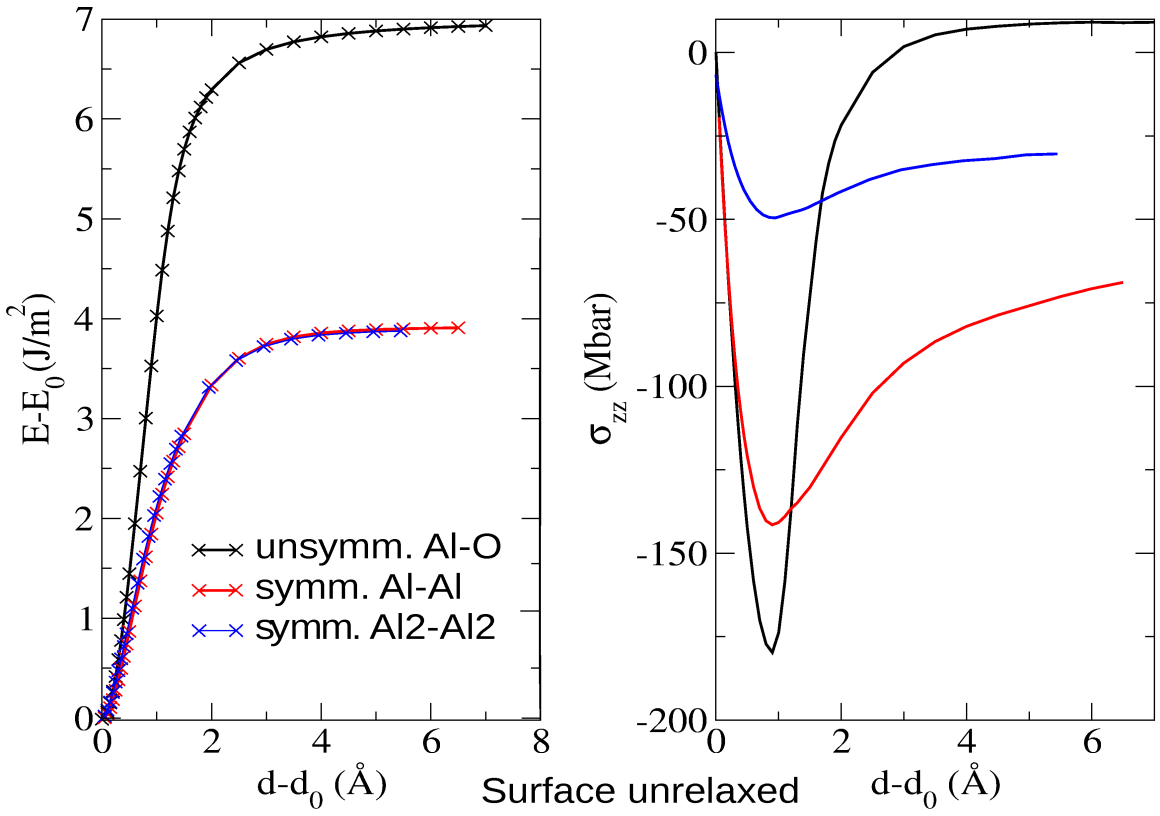

Figure 5.5: Comparison of unrelaxed symmetric-Al, double-Al and unsymmetric Al/O total energy versus layer distance is shown on the left hand side. The stress directed perpendicular to the plane is shown in the right hand side.

the calculated surface energies are given in Table 5.1. The results from the calculations are in good agreement with literature [176, 177, 166]. Based on the DFT calculations by I. Manassidis et. al. [176] provided the surface energies of the α - Al_2O_3 for (0001), $(10\bar{1}0)$ and $(11\bar{2}0)$ planes. The surface energies are 1.76 [J/m^2], 1.86 [J/m^2] and 1.4 [J/m^2] respectively. Second DFT (GGA) based calculation by Y. Liu [166] exhibited the surface energies of (0001) as 1.59 [J/m^2] and $(11\bar{2}0)$ as 1.88 [J/m^2]. In the case of Al_2O_3, the surface termination and composition affects the surface energy drastically, whereas the effect of the surface orientation on surface energy is weak.

In general, the discussion of the Al-O polyhedra seems the most natural choice for characterising the surface. In bulk corundum, only AlO6 octahedra are present, but at the surface, they have broken apart due to the constraints of a lattice planar surface and the required atomic ratio of O/Al atoms. This procedure results in distorted polyhedra for the unrelaxed surfaces given in the Table 5.2. However, on relaxation, this picture may change

Plane	A (Å^2)	BB	BB/A	O_{def}	O_{def}/A	O/Al	BO	γ [J/m^2]
0001	19.75	6	0.30	3	0.15	3/1	1	1.5
$01\bar{1}2$	61.75	15	0.24	6	0.097	12/8	2	2.1
$11\bar{2}0$	109.61	24	0.22	9	0.082	9/12	12	1.8
$10\bar{1}0$	74.95	12	0.16	6	0.080	6/6	4	1.6
$01\bar{1}4$	102.25	24	0.23	12	0.117	36/18	6	2.0 [166]
$11\bar{2}3$	45.12	10	0.22	3	0.066	28/14	6	2.25 [166]
$22\bar{4}3$	88.53	16	0.18	8	0.090	10/8	12	2.77 [178]

Table 5.1: Surface plane, A is surface area, number of broken bonds BB, broken bonds per area BB/A, number of oxygens missing to complete the AlO6 octahedra O_{def}, missing oxygen per area O_{def}/A, surface atomic density in the surface layer O/Al, the number of broken octahedral BO, surface energy γ.

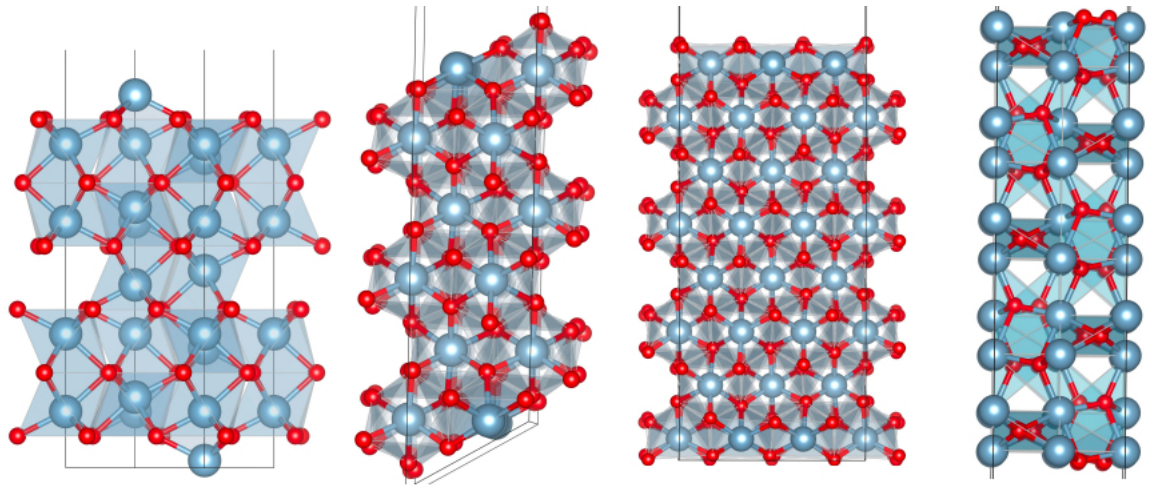

Figure 5.6: The illustration of the side view of α - Al_2O_3 planes: (0001), ($10\bar{1}2$), ($11\bar{2}0$), ($11\bar{2}2$).

drastically. Most of the quantities are well-defined, but the O/Al ratio and the surface atomic density depend on the way of assigning atoms to the surface.

For instance, in the case of the (0001) surface, the relaxation deforms the AlO3 to an almost planar configuration which releases nearly half of the initial surface energy. This is probably also the reason why the next layer on top of this surface during crystal growth is Al.

Surface	Dist. Polyhedra	per surface area($1/Å^2$)
0001	AlO3	0.05
$10\bar{1}0$	AlO4	0.06
$11\bar{2}0$	AlO5	0.11
$01\bar{1}2$	AlO5	0.08
$01\bar{1}4$	AlO4	0.06
$11\bar{2}3$	AlO3 +AlO5 1:2	0.07
$22\bar{4}3$	AlO3 +AlO5 3:2	0.07

Table 5.2: The distorted polyhedra sites per surface area of unrelaxed bulk structures.

The AlO5 polyhedron is a square pyramid (plane + apex atom), which seems to be less favourable than the AlO3 plane. However, discussing the $(11\bar{2}3)$ and $(22\bar{4}3)$ surfaces, it appears incorrect: here the admixture of more AlO3 meets with an increase in the surface energy. In this context, it would be useful to compare the relaxed surface structures. The AlO4 non-planar coordination also seems to be unfavourable, and its relaxed structure needs to be inspected. It appears that the distances and arrangement of the oxygen atoms do not allow a regular tetrahedron here.

The relaxation itself could be affected by the next-nearest neighbours because in Al_2O_3 these are usually atoms of the same element, which would repel each other. Likewise, the surface atomic density could be an indicator of the magnitude of the relaxation.

Other quantities related to the polyhedral are the density of distorted polyhedra on the surface and the surface density of oxygen needed to complete all open octahedra (Table 5.2).They are connected via the number of shared edges and corners on the surface, and thus are also related to the number of broken bonds. At least in the first case, the (0001) surface marks the minimum of the list. For the other surfaces, the polyhedra density behaves irregularly.

Results in the surface energies given in Table 5.3 results. The results from the calculations are in good agreement with literature [179]. Other methods for determining the binding energy to the surface should be considered, for example, the use of interatomic forces.

Termination	Surf. En. [Ry]	Surf. En. [J/m^2]
Al-Al	0.281	1.5
Al2-Al2	0.206	1.1
O3-O3	2.125	10.2

Table 5.3: Surface energy for different terminations of Al at (0001) in approximation

5.3.2 Binding Energy

The binding energy at the surface can be described as the difference between bulk cohesive energy and the surface energy, both per atom. By removing one atom from an infinite surface, this binding energy is obtained, because the change in the surface energy is insignificantly small. In approximation, the binding energy between a surface atom and the adjoining layer can be used as the surface binding energy. In this case the interaction with other surface atoms is neglected and the value can be interpreted as an approximation to the adsorbtion energy of an atom on a specific surface.

#	E (Ry)	E_{bind} (eV)
Al_2O_3 bulk	-204.603	37.5
Al ads. on Al_2O_3 Al surf.	-39.39	2.2
O ads. on Al_2O_3 2Al surf.	-41.86	9.9

Table 5.4: The DFT calculated binding energies of the α - Al_2O_3, Al and O.

Essentially this means that the calculated total slab energy should depend linearly on the number of adsorbed atoms. In Figures 5.7, 5.8 such data are plotted. The underlying surface is a double-Al terminated Al_2O_3 (0001) surface, which is the basis for the oxygen layer in the Al_2O_3 crystal structure. This surface contains excess aluminium, and thus its surface energy can not be determined by subtracting the bulk. The oxygen is symmetrically placed on top of this layer on both ends of the slab. The slab unit cell means the two (0001) surfaces of a single Al_2O_3 unit cell, i.e. an hexagonal lattice of 4.8 Å lattice parameter. This means that in case the two surfaces are covered with 3/2 oxygens each, the slab would be neutral (0 on the x axis). This would need a larger supercell (1x2) to describe the structure. The energy difference is calculated by subtracting the number of bulk units N_{bulk} and dividing by the number of slab unit N_{slab} cells in the respective supercell, then subtracting the DFT atomic total energy (see Table 5.6) for the 2 excess Al atoms and the for the number N_{ad} of adsorbed oxygen (equals x axis plus three).

The Table 5.4 holds the results for the approximate adsorption energy compared to the binding energy of Al_2O_3. Using these values, one can obtain binding energies of the surface of an adsorbed atom. A atomic binding energies to the surface results in the surface energies shown in Table 5.3.

However, the problem here is that the surface formation is a process in two steps: first a surface is created from the bulk with bulk composition, then a reaction occurs which changes the surface composition.

The Figures 5.7, 5.8 show calculated values for the adsorption energy for different surface covering. The adsorption of Al on the single-Al surface and of O on the double-Al surface

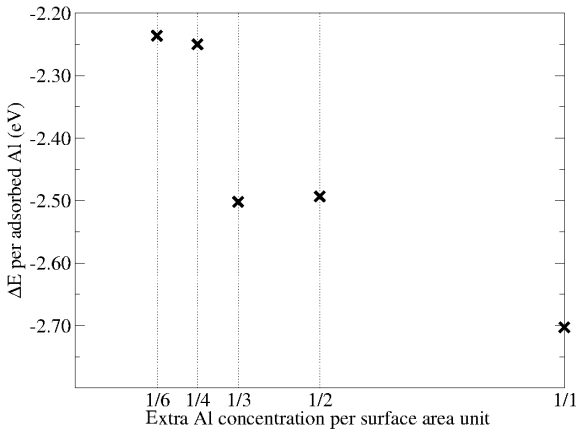

Figure 5.7: Adsorption energy for Al on Al terminated α - Al_2O_3.

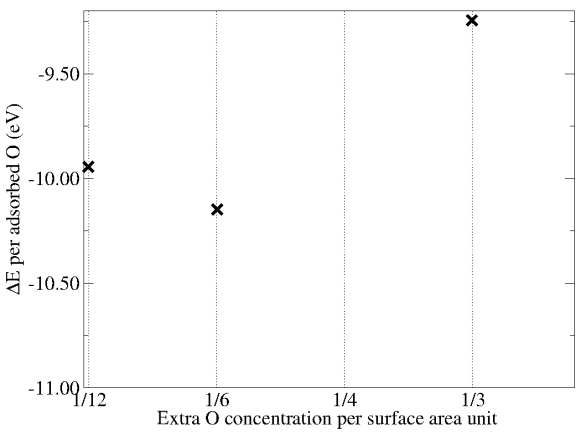

Figure 5.8: Adsorption energy for O on Al terminated α - Al_2O_3.

are considered. The adsorption energy is calculated as the difference of the partly covered and the uncovered slab total energies. This energy can be considered to be the sum of the surface energy of the underlying surface, the binding energy of the adsorbed atoms and the surface energy of the complete surface. For both cases on top of the surface, Al or O has created the bond length with lower layers equal to 1.97 Å, which corresponds to a covalent bond.

The adsorption energy was considered as:

$$\Delta E = E_{slab} - \frac{E_{bulk}}{N} - N_{Al}E_0(Al) - N_O E_0(O) \tag{5.14}$$

Where N is the number of unit cells in the slab, N_O and N_{Al} are the number of the oxygen and alumina in the slab, E_0(Al) and E_0(O) correspond to the atomic energies of Al and O.

The difference from the Equation 5.14 is now, of course, the formation energy of the "surface" Al_2O_3, which adds to the calculated "surface energy". Thus we have to think of a different type of reasoning to get the surface energy.

The differences in the calculated bulk energies depend on the slab thickness. These differences are caused by displacements of the atoms in the inner part of the slab, and should disappear for larger slab thicknesses. The slight differences in the relaxed in-plane lattice constants are another indication of this problem. For the values in Table 5.5, this inaccuracy amounts to 1% of the surface energy contribution. In rows 1 - 3 of Table 5.5, the slab composition differs from bulk Al_2O_3, by several Al or O atoms. In these cases, the discussion

of the surface energy becomes more complicated, because the additional atoms contribute to the total energy.

Termination	$d_{slab_{1,2}}$[f.u.]	Vac.[Å]	$a_{1,2}$ [Å]	Δ E[eV]	Bulk En.[eV/f.u.]
Al-Al	12, 18	10	4.83, 4.82	3.82	-2783.769
Al2-Al2	12, 15	15	4.80, 4,80	-1.61	-2783.772
O3-O3	11, 17	15	4.80, 4.80	-4.17	-2783.766
Al_2O_3 *bulk*	—	—	4.80	—	-2783.773

Table 5.5: Studied energies of Al_2O_3 (0001) with different terminations and slab thickness. The d_{slab} is the thickness of slab within different termination, Vac. the thickness of a vacuum, a length size of the surface, ΔE is the energy different between two thickness slabs in [eV], and Bulk En. represents the energy of a bulk along of given termination.

Therefore, the energy of the free atom relating to the pseudopotential (see Table 5.6) was subtracted.

pp	E (eV)
Al PBE	-533.7188
O PBE	-559.6057

Table 5.6: Atomic energy for selected PAW pseudopotentials for a free atom.

To calculate the surface energy, the binding energy of the surface atoms must be subtracted from this value.

The last term approximately vanishes for a single adsorbed atom on a very large surface. For oxygen, the fully covered surface contains three atoms per surface unit, while for Al it is only one atom per unit surface. The Figures 5.7, 5.8 show that there is a significant change at least for Al with decreasing surface coverage. It was observed that the underlying surface relaxation tends to react to the presence of Al on top, which could be thee cause for the change in energy. If on the other hand, oxygen is added in excess to the surface, the whole stack reacts during the relaxation, most probably because the charge redistribution takes place over a large volume.

In conclusion, it seems that none of the quantities related to the surface shown here determine the surface energy alone. A combination of several ingredients is needed. The character of the polyhedra distortions, their density on the surface and the possible relaxation. The elastic modulus seems to be inappropriate because of the high symmetry of the crystal compared to the surface structures.

Chapter 6

Interface energy investigation

Knowledge of the better interface structure and its energies are essential for the filtration process, where it is important to control the kinetics, material growth, roughness, stability and dissolution of substances. Due to the application, the strong bonding at the surfaces may be required for ceramic-metal interfaces. The formation of a ceramic-metal interface calls for lattice adjustments by the bulk materials, and notable progress is being made in defining the atomic structure of interfaces. However, the number of systems studied so far is rather limited. A large research effort is needed for the development of suitable theoretical models to simulate the interfaces caused by thermodynamic or mechanical driving forces. Interfaces can be pictured theoretically in different ways [180], depending on the desired level of resolution. One of the approaches can make a macroscopic model of interfaces. The thermodynamic phases can be treated separately, and the interface defines suitable boundary conditions for their development. Coatings as thermal barriers or corrosion protection are used by the manufacturers, where the lifetime and efficiency are important. Understanding of the geometric and electronic properties of the interfaces is substantial in advance to get a better coating process and material properties. Over the last half century, researchers strived to gain the necessary understanding and optimise the mechanisms needed to study mechanical, electrical and chemical properties of the interfaces [181–185]. However, experimental complications have been linked to the investigation of immersed interfaces. The theoretical difficulties arising from complex interfacial bonding interactions have hindered the development of general, analytic models capable of accurately predicting the fundamental interfacial quantities.

The filtration effect depends on interactions at the interface of the ceramic filter material. Interestingly, various ceramic materials show different filtration efficiencies. Therefore, a detailed understanding of the processes at the interface is of interest. Besides, experimenters

observed that different solid - solid interfaces arise due to the filtration process inside the filter.

This chapter described a first-principles calculation of the interface energy calculation for the stable phase α - Al_2O_3 (0001) and Al (111) interface. In order to investigate the effect of oxygen or aluminium termination, the calculation on Al_2O_3 with these two terminations was carried out.

Furthermore, the solid-solid state reactions of the formation of interfaces between $MgTiO_3$(geikielite) $\parallel$ TiO_2 (rutile) and α - Al_2O_3 (corundum) $\parallel$ TiO_2 (rutile) was studied. The crystallographic relations were investigated by X-ray diffractometry (XRD) [186, 18, 19]. The crystallographic orientations of the mentioned substances solid-solid interfaces via scanning electron microscopy with energy dispersive X-ray spectroscopy (SEM/EDX), electron probe microanalysis including wavelength dispersive X-ray spectroscopy (EPMA/WDX) and by electron back-scatter diffraction (EBSD) were studied under the CRC 920 project.

Besides α - Al_2O_3 (0001) $\parallel$ Al(111) interface, this chapter gives an investigation of the $MgTiO_3$(geikielite) $\parallel$ TiO_2 (rutile) and α - Al_2O_3 (corundum) $\parallel$ TiO_2 (rutile) literature crystallographic orientations relationship versus the obtained crystallographic orientations from CRC 920, subproject A06.

6.1 Interface energy of Al_2O_3 (0001) $\parallel$ Al (111)

Provisionally, the Al (111) plane has been found to be the favoured interfacial plane for epitaxial growth of Al on α-Al_2O_3 (0001) [187, 188]. The interface of Al_2O_3 with Al is interesting since they are found practically at opposite ends of the range of oxide formation temperature [189]. Transmission electron microscopy (TEM) [190] of the Cu $\parallel$ Al_2O_3 interface has shown that Cu (111) is the preferred orientation [191]. However, no such TEM data exists for the Al $\parallel$ A_2O_3 interface. In both cases, the interface arises between an fcc metal and Al_2O_3, hinting that Al will have the same crystallography orientation as Cu. It is known that the stoichiometry of Al_2O_3 structure is a sandwich of aluminium and oxygen atoms (see Figure 5.4) and that Al_2O_3 structure can be denoted within different terminations in the (0001) plane. Here two terminations of Al_2O_3 structure were considered, a single Al termination and an O termination. It is known [192, 168] that for an Al_2O_3 (0001) clean plane, the stoichiometric surface termination is Al.

The slabs were obtained by defining a surface area which has the initial Al_2O_3 structure (a = b = 4.75 Å, $\gamma = 120^o$). The distance between the two substances is 1.8 Å in the case of $(Al_2O_3)_{Al}$ and 2 Å when there is $(Al_2O_3)_O$. After optimising the lattice parameters and atomic positions, there is a slight shift of the atomic positions. After full optimisation of cell

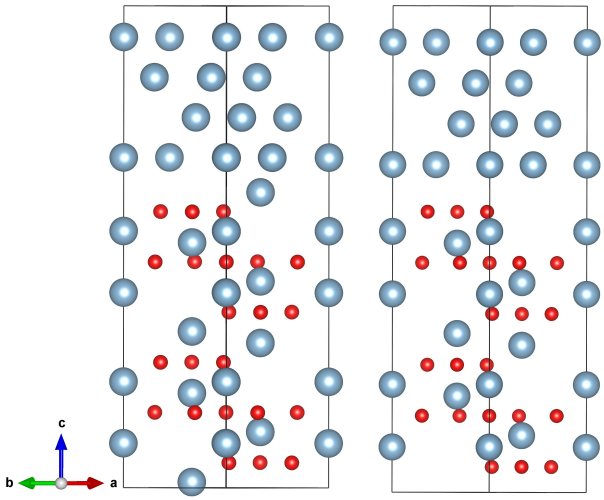

Figure 6.1: The illustration of the created interface of Al_2O_3 (0001) || Al (111) with different terminations of α - Al_2O_3 (0001).

parameters and atomic positions, the distance between Al_2O_3 within O-terminated sublattice and Al (111) becomes 1.85 Å after. Nevertheless, in the case of Al_2O_3 with Al termination, the optimisation was achieved in a way that one of the Al atom moved toward the O atom, which lies down under the Al atom (the distance became 1.94 Å). Moreover, the other Al atom of Al (111) moved a little further away from Al_2O_3 Al atom (in the distance 2.5 Å).

To get a more profound understanding of the matter of created interface was done a calculation of the charge density distribution at the interfaces for those two different terminated slabs.

For the α - Al_2O_3 (0001) || Al (111) slab interface calculation, the Quantum ESPRESSO code using PAW pseudopotentials was used with the exchange-correlation functional generalised gradient approximation (GGA). A cutoff energy of 90 Ry was obtained as a reasonable setting after convergence test, and the effective potential was expanded in reciprocal space on a grid with a cutoff frequency equivalent to 360 Ry along with the k-points grid of $5\times5\times2$. The charge density calculations were carried out with same settings.

6.2 Interface energy of $MgTiO_3$ || TiO_2 and Al_2O_3 || TiO_2

TiO_2 can arise through three different polymorphisms which are called brookite, rutile and anatase. Nanoparticles often established a brookite - TiO_2 [193, 194]. TiO_2 - rutile is a high-temperature stable phase. It is stable above 850 K and the transition to the low- temperature anatase phase can be suppressed [195]. The TiO_2 - rutile has the highest dielectric constants of the all binary oxides [196] which performs TiO_2 - rutile as a dielectric in different applications.

Numerous investigations have studied TiO_2 on perovskite substrates, such as $LaAlO_3$ and $SrTiO_3$ [197, 198], and homoepitaxial growth on TiO_2 - rutile single crystals [199]. TiO_2 - rutile has also been grown on (Al)GaN [200]. The common growth is found to be independent of the oxygen pressure that all substances were grown in. The oxygen - rich regime and Ti flux limit the growth [18]. Several epitexial orientation relationships are reported in literature, for instance TiO_2 $[\bar{1}11]$ ‖ Al_2O_3 $[42\bar{1}]$ [201, 202] and TiO_2 [101] ‖ Al_2O_3 [012] [18].

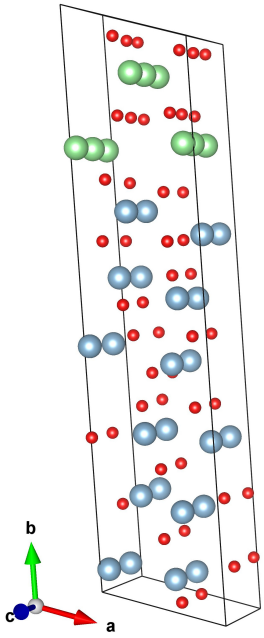

Figure 6.2: The orientation relationship of the interface found by X-ray diffractomatry XRD [18]. The picture illustrates the Al_2O_3 {012}[100] and TiO_2 {101}[010] interface.The green colour represents Ti atoms, blue is Al, and the red are O.

In particular, TiO_2 and Al_2O_3 structures show similarities in the arrangements of the oxygen octahedra.

It is know by MgO ‖ TiO_2 bulk phase diagram that various compounds may arise, like Mg_2TiO_4, $Mg_2Ti_2O_5$, $MgTiO_3$ [203–205]. The first formed phase in a thin-film solid state reaction [19] was reported. It was shown that only $MgTiO_3$ phase was grown of TiO_2 - rutile and the different surface orientations between the two substances were studied. The crystallography relations were investigated by X-ray diffractometry (XRD) and transmission electron microscopy [19]. It was found that $MgTiO_3$ $[1\bar{1}0]$ and TiO_2 - rutile [100] planes are parallel to each other and create a solid - solid interface [19].

When TiO_2 - rutile was exposed to molten aluminium, acid chemical interactions arise at the interface driving the formation of a layer of thermodynamically stable corundum. In the case of exposure to molten aluminium alloy, corundum formation was headed by a layer of the transitional phase $MgTiO_3$. Al_2O_3 and $MgTiO_3$ with determined orientation relationships to the TiO_2 - rutile properties acted as a barrier among TiO_2 and the respective melt.

TiO_2 accumulated on corundum (α - Al_2O_3) substrate is used in the manufacture of ceramic filters for aluminium alloy melt filtration. Ceramic foam filters coated with TiO_2 show the reasonable filtration efficiency. Meanwhile, it yields to the high melt flow rates

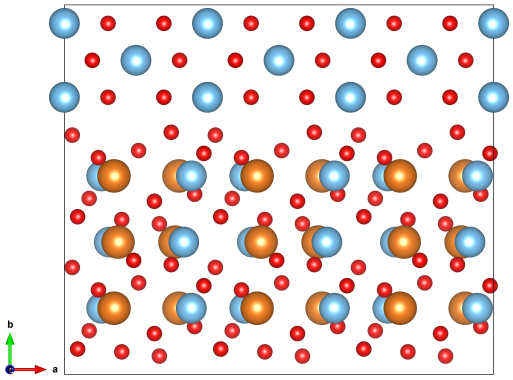

Figure 6.3: The orientation relationship of the interface found by X-ray diffractomatry XRD [19]. The picture illustrates the $MgTiO_3$ $\{110\}[1\bar{1}0]$ and TiO_2 $\{100\}[001]$ interface. The orange colour corresponds to Mg, the blue ones are Ti, and the red balls are O.

[206]. Recently, it was revealed for TiO_2 coated ceramic foam filters that it reach out as a "reactive" filter surface [207, 208]. The formation of α - Al_2O_3 was found to be caused by the chemical reaction with the TiO_2 coated filter surfaces during a filtration process [208]. Supplementary phases of α - Al_2O_3 appear after long process times [208]. The TiO_2 is a reactive coated filter surface decreasing the oxygen access to the molten metal accompanying it via the formation of the $MgTiO_3$ and Al_2O_3 solid states [206].

By the references [18], TiO_2 can be grown substance on Al_2O_3 surfaces via molecular beam epitaxy method. It was noted that the surface morphology changes due to the change of oxygen flux to the surface.

Under the CRC-920 project within subproject A06, experiments using a Spark Plasma Sintering (SPS) device were performed to reflect the heat treatment as a standard aluminium casting besides the melt flow. It is admitted that the low-indexed crystallographic orientated substance interfaces should form preferentially the orientations given in the literature. The obtained products were analysed via scanning electron microscopy with energy dispersive X-ray spectroscopy (SEM/EDX), electron probe microanalysis including wavelength dispersive X-ray spectroscopy (EPMA/WDX) and by electron back-scatter diffraction (EBSD). The local orientation relationship between the formed α - Al_2O_3 crystal growing onto the TiO_2 - rutile matrix occurs according to the relationship $\{100\}[010]$ α- Al_2O_3 || $\{001\}[100]$ TiO_2. This orientation relationship has already been described in the literature [209].

The subproject A06 - CRC 920 found that $MgTiO_3$ formed after short annealing between alloy and TiO_2. The $MgTiO_3$ prevents the contact of the molten aluminium alloy with the TiO_2 - rutile coating, thereby inhibiting the further interaction between the ceramic filter surface and the metal melt. Nevertheless, $MgTiO_3$ is not a stable phase at the high-temperature range [210]. So far, it is the only solid phase found outside of Al, Si (in the Al alloy) and TiO_2 (disregarding the corundum substrate). Consequently, can be considered the TiO_2 - rutile coating on ceramic filter material as a precursor since it impacts for the formation of $MgTiO_3$, which, as the originally formed interim phase, is persistent enough to encompass

the direct reduction of TiO_2 and prevent the formation of thermodynamically stable corundum. $MgTiO_3$ behaves as a diffusion barrier not only limiting the corrosion of TiO_2 - rutile but also preventing the undesired impurity of the alloy melt. A determined orientation relationship between $MgTiO_3$ and TiO_2 crystal growth as $\{001\}[010]$ TiO_2 $\parallel$ $\{100\}[001]$ $MgTiO_3$. However, this particular crystallographic orientation between those two phases has not been reported in the literature.

TiO_2 has a tetragonal unit cell in P42/mnm space group (#136) with cell parameters a=b=4.65 Å and c=2.95 Å . The Ti cations surrounded by six O atoms which build an octahedra, and O anions have a coordination number of three, which corresponds to a trigonal site.

$MgTiO_3$ is in the trigonal crystal system in space group $R\overline{3}$ (# 166) with lattice parameters a = b = 5.05 Å , c = 13.9 Å , $\alpha = \beta = 90^o$, $\gamma = 120^o$.

For $MgTiO_3$ $\parallel$ TiO_2 and Al_2O_3 $\parallel$ TiO_2 slab interfacal calculation the Quantum ESPRESSO code using PAW pseudopotentials with the exchange-correlation functional generalised gradient approximation (GGA) was used.

6.3 Results and Discussion

6.3.1 Methods of calculations the interface energy

DFT calculations were used to gain an understanding the presented interface orientations and to find out which one will be favourable. Knowledge of the interface energy of each given orientation's relationship can yield the comprehension of presented crystallographic orientations.

The interface energy calculation was done with respect to the slab and bulks calculations. The slab is a box, which contains several atomic layers cleaved from the corresponding materials, which form the interface. The interface is created according to the crystallographic orientation suggested by experiment. Moreover, the bulk estimates as a box of substance, which is included in the slab calculation. For obtaining the interface in the given orientations, the bulk structure of each substance in found crystallographic orientation was created. Afterwards, the slab was built, which is two given bulk structures one on top on other. At this stage, one should pay attention to the fact that the lattice parameter of the bulk structures should be nearly equal. For obtaining the interface energy of the built slab several calculations should be done, and the total energy from each of created bulk structure and slab were taken into account.

$$\sigma = \frac{E_{slab} - E_{bulk_1} - E_{bulk_2}}{2A} \tag{6.1}$$

where σ is an interface energy, E_{slab}, E_{bulk_1} and E_{bulk_2} are total energies of the slab and bulks from the ab-intio DFT calculation, and A represents the interface area.

6.3.2 Results of Al_2O_3(0001) || Al (111) interface energy

First, the accuracy of the computational approaches is confirmed by calculating the bulk properties of Al(111) and α-Al_2O_3 (0001) of the corresponded structure.

For Al_2O_3 (0001) and fcc Al (111), the obtained slab in the two formula unit bulk from Al_2O_3 and Al bulk within four layers is considered. The Al(111) have been stretched a little to obtain the interface between two substances since the α - Al_2O_3 (0001) surface is on the lattice plane with parameters a = b = 4.74 Å, but Al (111) plane has a = b = 4.049 Å lattice parameters. The created slabs had a = b= 4.75 Å, c = 27.80 Å (Al - termination) or c = 21.99 Å (O - termination), $\alpha = \beta = 90^o$ and $\gamma = 120^o$. After full relaxation of lattice parameters and atomic positions were obtained the following cell - parameters a = 4.84 Å, b = 4.93 Å, $\alpha = 91.90^o$, $\beta = 93.01^o$, $\gamma = 119.90^o$ and the slab thickness was 27.80 Å in the case of α - Al_2O_3 (0001) Al - terminated interface slab. On the other hand, in the case of Al_2O_3 (0001), O - terminated interface slab after full optimisation of lattice parameters and atomic positions resulted in a cell with a = 5.3 Å, b = 5.21 Å, $\alpha = 86.93^o$, $\beta = 93.91^o$, $\gamma = 94.38^o$ within a slab thickness c = 21.99 Å.

Initially, the bond length between two surface atoms which lay on the interface was considered d = 2.7 Å in the both cases of the slab where α - Al_2O_3 (0001) surface is O-terminated or Al - terminated. After optimisation of the lattice parameters with the atomic position the Al (111) bulk went into α - Al_2O_3 (0001) surface and the bond lengths became as initiated in the α - Al_2O_3 structure, d = 1.87 Å or 1.93 Å.

Structure	Termination	N_{atom}	E_{total}[eV]
Al_2O_3	Al	30	-16735.96
Al_2O_3	O	28	-15609.36
Al	-	16	-7524.57
$Al_2O_3^{Al}$/Al		46	-24271.12
$Al_2O_3^{O}$/Al		44	-24267.79

Table 6.1: The number of the atoms in the particular created structure with its total energy calculated via DFT.

Results for interface energies in the case of different terminated Al_2O_3 || Al can be found in table 6.2. From these values, it is clear that the O-terminated surface is favourable but also Al-terminated surface can be considered since it is preferred one compare with the separate bulk structures. It was reported by Zhang and Smith [211] that the Al_2O_3 || Al interface

is likely preferred in an oxygen - rich interface formation. In addition, it was established that $Al_2O_3^O$ || Al interface is more stable then $Al_2O_3^{Al}$ || Al. Nevertheless, it is acknowledged [192, 168] that for a clean Al_2O_3 surface, the stoichiometric surface $Al_2O_3^{Al}$ is the stable.

Interface	Contact area A(Å)	σ [J/m^2]
$Al_2O_3^{Al}$/Al	23.86	-2.43
$Al_2O_3^{O}$/Al	27.61	-3.07

Table 6.2: The calculated interface energies in the case of different orientated α - Al_2O_3 (0001) || Al (111). A is the interface contact area.

D. J. Siegel et al. [212] $Al_2O_3^O$ || Al with the interface energy equal -1.28 [J/m^2] found as a favourite termination. Moreover, for the $Al_2O_3^{Al}$ || Al interface energy was reported to be equal to 1.34 [J/m^2]. Experimentally, adhesion data for $Al_2O_3^{Al}$ || Al scaled to 0 K is estimated as 1.13 [J/m^2] [213]. In addition, Merlin and Eusthopoulos found an interface energy equal to 1.07 [J/m^2] at T = 1750 K. And interface energies given by Zhang and Smith [211] are: $Al_2O_3^{Al}$ || Al has 1.078 [J/m^2], $Al_2O_3^{O}$ || Al has 10.095 [J/m^2] and for $Al_2O_3^{Al2}$ || Al interface the interface energy was obtained 1.433 [J/m^2].

With those diverse interface energy values given in the references and particularly obtained from DFT-calculation, it is difficult to make a comparison and build fundamental conclusions.

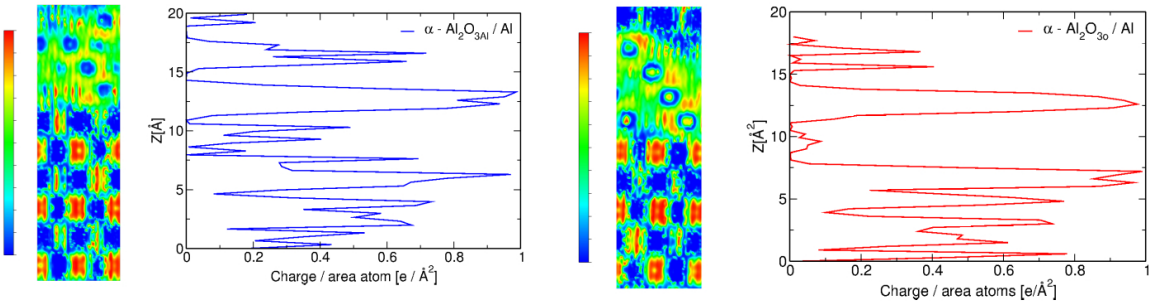

Figure 6.4: The charge density of α - Al_2O_3 (0001) || Al (111) interface, within a different terminated Al_2O_3 analysed via electron localisation function (ELF). The blue colour represents the negative charge and red colour corresponds to positive charge.

Apart from analysing the atomic structure and interface energies of Al_2O_3 (0001) || Al (111), it has used the Effective Screening Medium Method [175] as implemented in the Quantum Espresso code to characterise the nature of the interface's electronic structure and its bonding in respect to charge distribution.

The description of the charge density of Al_2O_3 || Al slab (in different terminated Al_2O_3) is illustrated in figure 6.4, which is analysed via electron localisation function (ELF). ELF

subtracts to identify the regions of space that holds a high concentration of paired and unpaired electrons, which can afterwards be defined as bonds, lone pairs and dangling bonds.

As shown in the figure 6.4, the slab the part, which represents Al_2O_3 has a clear distribution of changes and one can see the ordered bonds. In the case of the Al part of the slab, a particular colour cannot be clearly distinguished. Figure 6.4 also presented the charge pro - atom area versus slab thickness, where one can see that in that part of interface the charge distributions are different for different terminated Al_2O_3. For O - terminated the case it is $\approx$ 0.08 and in the Al - terminated one $\approx$ 0.48. This differences can be explained by the bonding effect, in regards to the process that Al (111) bulk is getting more into the Al_2O_3 bulk when there is O - termination then Al - termination.

6.3.3 Results of of $MgTiO_3$ || TiO_2 and Al_2O_3 || TiO_2 interface energy

The method of creating $MgTiO_3$ || TiO_2 and Al_2O_3 || TiO_2 interface slabs was done as it was explained in section 6.3.2.

The $MgTiO_3$ {100}[001] || TiO_2 {001}[010] [19] interface slab was made by stretching the TiO_2 bulk structure from one side in $\approx$ 1 Å. Following the full optimisation of the slab structure the cell parameters a = 16.78 Å, b = 15.32 Å, c = 7.53 Å and α= 88.81^o β = 83.53^o γ = 96.1^o were obtained. The optimised parameters were achieved within settings with the generalised gradient approximation (GGA). Single-electron Kohn-Sham states were calculated on a k-point grid of $3 \times 3 \times 3$ points, and the valence electron wave functions were extended in a plane wave basis, with a cutoff energy of 80 Ry and the effective potential was reached in reciprocal space on a grid with a cutoff frequency equivalent to 320 Ry.

Structure	Orientation	N_{atom}	N(f.u.)	E_{total}[eV]
$MgTiO_3$	{001}[1$\bar{1}$0]	105	21	-32533.14
TiO_2	{100}[001]	54	18	-17444.84
$MgTiO_3$ || TiO_2		159	–	-49976.43
Al_2O_3	{012}[100]	60	12	-5094.78
TiO_2	{101}[010]	18	6	-33408.01
Al_2O_3 || TiO_2		78	–	-38517.19

Table 6.3: Crystallographic relationship found in the literature. In the table, given the number of the atoms in the particular created structure with its total energy calculated via DFT are given.

The Al_2O_3 {012}[100] || TiO_2 {101}[010] [18] was obtained by stretching TiO_2 in a way that lattice parameters stay the same and only the angle γ was changed from 90^o to 120^o. The optimised cell parameters of Al_2O_3{012}[100] || TiO_2{101}[010] slab was accomplished as

a = 6.3 Å, b = 28.32 Å, c = 6.6 Å, $\alpha = 86.43^o$, $\beta = 91.26^o$ and $\gamma = 106.83^o$. Slab optimisation was done within a generalised gradient approximation (GGA) and a k-point grid was set as a $8 \times 2 \times 9$, cutoff energy set to 70 Ry, and the effective potential was reached in reciprocal space on a grid with a cutoff frequency equivalent 280 Ry.

The calculated total energy of each of bulk structure and slab are given in the table 6.3. The results relating to equation 6.1 are given in table 6.5.

The established orientation relationship between TiO_2 - rutile and corundum, {001}[100] TiO_2 || {100}[010] α - Al_2O_3, has been described by Chen et al. [209] for the deposition of TiO_2 - rutile in a single crystal of {100} - oriented α - Al_2O_3 (sapphire). In the reference, the oriented growth is explained by a similar arrangement of the oxygen sublattices in the given orientation, resulting in small lattice misfits of -3.6% along [010] α - Al_2O_3 and +5.8% along [001] α - Al_2O_3. The associated residual stresses are minimised by the mobility of the Ti atoms c-axis directional growth [209].

The structure with its orientation and total energies calculated via DFT for bulk and slab are presented in table 6.4.

After optimization, the $MgTiO_3$ {100}[001] || TiO_2 {001}[010] slab lattice parameters and atomic positions became a = 5.66 Å, b = 18.63 Å, c = 5.63 Å, $\alpha = 88.37^o$, $\beta = 91.89^o$, $\gamma = 94.49^o$. A a cutoff energy of 95 Ry was used, and the effective potential was expanded in reciprocal space on a grid with a cutoff frequency equivalent to 380 Ry along with the k-points grid of $12 \times 3 \times 14$.

Structure	Orientation	N_{atom}	N(f.u.)	E_{total}[eV]
$MgTiO_3$	{100}[001]	30	5	-8677.73
TiO_2	{001}[010]	15	5	-4048.97
$MgTiO_3$ || TiO_2		45	–	-12748.42
Al_2O_3	{100}[010]	90	18	-44605.64
TiO_2	{001}[100]	51	17	-25346.46
Al_2O_3 || TiO_2		141	–	-70027.39

Table 6.4: Crystallographic relationship found from subproject A06 - CRC 920 examining the samples of corundum, which were coated by rutile and brought in contact with molten aluminium powder or molten aluminium alĺoy. In the table, the number of the atoms in the particular created structure with its total energy as calculated via DFT are given.

After optimization, the Al_2O_3 {100}[010] || TiO_2 {001}[100] interfaceal slab got cell parameters like: a = 16.88 Å, b = 12.93 Å, c = 8.5 Å and $\alpha = 89.49^o$ $\beta = 88.62^o$ $\gamma = 88.82^o$ within a settings of the cutoff energy 60 Ry. The effective potential was expanded in reciprocal space on a grid with a cutoff frequency equivalent to 240 Ry along with the k-points grid of $8 \times 2 \times 9$.

In the table (6.5) the first two lines are the interface crystallography orientation found in the literature. The third and fourth lines are the interface orientation determined from subproject A06 - CRC 920. The interface energy values calculated from DFT show that an interface crystallography orientation estimated from subproject A06 - CRC 920 are the more convenient in contrast with ones discovered in the literature. The minus sign indicates that the formation of the particular interface is more favourable than the separate state of the two bulk structures.

Interfaces	Orientation	Contact surface A[Å^2]	σ[J/Å^2]
$MgTiO_3$ ‖ TiO_2	$\{001\}[1\bar{1}0]$ ‖ $\{100\}[001]$	126.35	0.14
Al_2O_3 ‖ TiO_2	$\{012\}[100]$ ‖ $\{101\}[010]$	41.58	-4.15
$MgTiO_3$ ‖ TiO_2	$\{100\}[001]$ ‖ $\{001\}[010]$	32.12	-4.95
Al_2O_3 ‖ TiO_2	$\{100\}[010]$ ‖ $\{001\}[100]$	105.43	-6.78

Table 6.5: The interface energy of the discussed crystallographic orientations calculated via DFT.

The calculated interfacial energies indicate that the found orientation relationships are energetically preferred in comparison to the reference orientation relationships that have been taken from the literature.

The chemical reactions, TiO_2 is reduced to Ti which is released into liquid aluminium or aluminium alloy melt. The reduction of TiO_2 by aluminium directly leads to the formation of thermodynamically stable α - Al_2O_3 and for a formation of $MgTiO_3$ necessitates the release of O and metallic Ti as a result of the TiO_2 reduction and verifiable consumes all Mg from the melt:

$$3TiO_2(s) + 4Al(l)(750^oC) \rightarrow 2Al_2O_3(s) + 3Ti(l) \tag{6.2}$$

$$3TiO_2(s) + 2Mg(l)(750^oC) \rightarrow 2MgTiO_3(s) + Ti(l) \tag{6.3}$$

The study by subproject A06 revealed from the examinations on the long-time annealed samples that the release of Ti, which is certainly affiliated with the formation of α - Al_2O_3 in agreement with a thermodynamic equation 6.2 did not govern to the presumed precipitation of Al_3Ti. Furthermore, in the final solidified aluminium, the amount of Ti increase is not discernible. This rare appearance of Ti was associated with the very thin layer of corundum formed at the interface Al ‖ TiO_2 and, consequently, the overall small reaction volume resulting in a small amount of metallic Ti being released. Additionally, the α - Al_2O_3

interlayer was shown to inhibit further TiO_2 - Al and Mg interaction attending to a halt in the reduction process, self-limiting the product formation of equations 6.2, 6.3.

Chapter 7

Summary and outlook

7.1 Summary

This dissertation has seven chapter including summary and outlook chapter. In each chapter, a short introduction to the chapter is given where the main investigation questions are discussed. Then a review of the structures and their behaviour. Moreover, each chapter is completed with methods and results.

The key aspects of this dissertation were to reproduce the open pore ceramic filter materials, their coated interfaces and inclusions materials without any input from experimental data. The aim is to provide a basis for the improvement of realistic data, which may be used for the future development of filter materials and improvement of the filtration process since the interest in removing inclusions in metal making and usage is growing. The essential part of the dissertation is the study of the thermodynamic data and the phase formations that are of concern due to the casting process of aluminum - based light alloys. In the aluminum - rich alloys, even a small amounts of Fe causes the formation of intermetallic compounds. Therefore the knowledge of aluminum - based binary and ternary intermetallic phase systems are remarkably constrained. Nevertheless, the thermodynamic experimental data for some intermetallic phases are abstaining. However, the empirically calculated data (e.g. specific heat capacity, thermal expansion coefficient), for instance, using the Neumann - Kopp rule does not always give a reasonable result. Accordingly, on the thermodynamic properties different Al-Fe intermetallics were investigated. Moreover, the focus of this study was on η - Fe_2Al_5, ε - Fe_5Al_8 and τ_4 - Al_3FeSi_2 intermetallic phases.

For prediction of the thermodynamical properties, the density functional theory (DFT) as implemented in the Quantum Espresso code was used. It is a theoretical calculation which does not require experimental input data. The inputs of this method are the crystallographic

information file (CIF) of the systems. Furthermore, from the calculated DFT total energy as a function of volume, the pressure can be obtained, so then the Gibbs energy as a function of pressure and temperature can be presented. Then the Gibbs energy as a function of pressure and temperature brings the possibility to derive all the thermodynamic quantities. In addition, the DFT calculation provides the quantum mechanical forces between the atoms. Thus forces can be used for the calculation of the elastic properties of the crystals.

As it is discussed in Chapter 3, usually the intermetallics have a large unit cell or with partially occupied sites of atomic positions. Consequently, for DFT calculations one needs to have certain given atomic positions. Therefore, the η - Fe_2Al_5 structure was provided as an approximate structure, and as a result, from the orthorhombic with space group (SG #63, Cmcm) it became monoclinic with space group (SG #12, c2/m). Hence, the SG #12 requires 13 independent elastic constants which are shown in equation 3.1 in GPa using the Voigt notation for the elastic force constant tensor. According to Voigt notation, the bulk modulus is B_V = 125.7 GPa, and the shear modulus is G_V = 85.0 GPa at T = 0 K. Afterwards, the pwtools package was employed [109] to obtain the complete thermodynamical calculations by creating nine $2 \times 2 \times 2$ supercells. The full relaxation mechanism was repeated for a different volume in the range of -1 to 5% compared to the relaxed volume, since, as a result of this volume change, the atoms were not located in their equilibrium positions. Then, the slight displacement of the single atomic position of each supercell was created by the phonopy code. Overall, 14 displacement structures were sufficient, if there was no broken symmetry.The predicted heat capacity of the η - Fe_2Al_5 is given in figure 3.10. From this result it can be concluded that the approximated structure works very well at the low temperatures down to 460 K. The high temperatures stabilise the disordered structure as a result of partial occupancy. As a result, it can be explain the slightly smaller result of the specific heat capacity as calculated by DFT in comparison to the experimental values measured using differential scanning calorimetry (DSC). However, the calculation of thermophysical properties was performed up to 2000 K. This is above the 1431 K melting point of η-Fe_2Al_5.

The next binary system under investigation was ε - Fe_5Al_8, which is the high-temperature phase and it is stable between 1368 - 1504 K. This structure has been found as a full occupied structure. The unit cell parameters are a = b = c = 8.97 Å, $\alpha = \beta = \gamma = 90^o$ and there are 52 atoms in a unit cell. With this amount of atoms, the creation of a $2 \times 2 \times 2$ supercell structure would give a large cell with 432 atoms in it. With this vast atomic numbers, the calculation via DFT is not reasonable due to it the high cost. Therefore, in the case of the ε-Fe_5Al_8 phase, the thermodynamical calculations were accomplished by creating $1 \times 1 \times 1$

so-called supercells, which were used for the phonon calculations at the *gamma* points. Ten displacement structures have been set up for ten different volumes with the corresponding space group. The change of the cell volume was in the range of -15 to 5 %. The obtained energy - volume curve and the phonon density of state is shown in figures 3.11, 3.12. It is shown that the ε-Fe_5Al_8 phase with the given structure has an tendency to be under pressure. This kind of behaviour can be explained due to the fact, that the ε - Al_8Fe_5 structure is a high - temperature existing structure. Nonetheless, the DFT calculation is done at T = 0 K. An obtained bulk modulus is B_0 = 152.46 GPa, and the optimised volume is V_0 = 668.93 Å^3. According to the space group #217, there are three independent elastic constants which are given in equation 3.2, in Voigt notation. The unit of the matrix entries is GPa. The specific heat capacity achieved by DFT calculations is presented in figure 3.10. The experimental results from differential scanning calorimetry (DSC), which is the blue line in the figure, is very high and has sharply increasing behaviour. This prototype of conduct corresponds to the point when one sees the phase transition, or it reaches the melting point. The estimated result of Neumann-Kopp is between two results from DFT and DSC. The green line presented in the figure is a predicted thermodynamic calculation by the code from T. Zienert (subproject A03). There was no data available for ε - Fe_5Al_8 phases to have a comparison.

The ternary Al-Fe-Si system and its thermodynamic properties were considered under this study. There are eleven ternary phases of Al-Fe-Si system. The investigation was gone on τ_4 - Al_3FeSi_2, which is orthorhombic with a space group *Pbcn* and has the lattice parameters a = b = 6.061 Å, c = 9.525 Å and $\alpha = \beta = \gamma = 90^o$. After full optimisation of the structure cell parameters and atomic positions, the obtained structure had cell parameters a = 6.06112 Å, b = 6.05789 Å, and c = 9.46554 Å, with $\alpha = \beta = \gamma = 90^o$ in the space group *Pbcn* (SG #60). The energy-volume curve and the phonon density of state for τ_4 - Al_3FeSi_2 structure is obtained by the volume change in a range of 10% compared to the relaxed volume. In total, ten structures were considered. The calculated Al_3FeSi_2 elasticity tensor is shown in the table 3.3 in GPa, in Voigt notation. The obtained shear modulus is $G = 82$ GPa, Poisson ratio is $\nu = 0.22$ and a bulk modulus is $B_0 = 120$ GPa. The calculated elasticity tensor is shown in the equation 3.3 in Voigt notation. The estimated numerical error is indicated in parentheses C12, and C21 have some differences, although due to the symmetry they should be equivalent. However, these differences fall well within the given error ranges. The calculated specific heat capacity is shown in figure 3.16, where the DSC measurements of c_P is also given. They are in good agreement at the high temperatures between 900 - 1000 K whereas the predicted specific heat capacity from Neumann-Kopp rule at the low-temperature range, like 300 - 600 K, shows good agreement with DFT calculation. However, at 900 K there are substantial

differences between two curves. The Neumann - Kopp rule cannot successfully completely qualify the specific heat capacity.

These results would help to gain data over a wide temperature range since there are certain difficulties in measuring the specific heat capacity of the different compounds, and the empiric Neumann - Kopp rule does not always yield a reasonable result. Besides, this results can take part in CALPHAD type assessment.

Since the surface chemical composition of the ceramic filters has a significant impact on the filtration efficiency, the investigation of surfaces and interfaces are crucial. The main substance of the ceramic filters is the Al_2O_3. Moreover, the filters are used for a filtration of the metal melts. Therefore, there is a purpose of investigating the possible to occur of interfaces between the several compounds in the system Al-O-Fe. Chapter 4 presented the study of the formation of hercynite ($FeAl_2O_4$) in the selected solid state reactions of corundum (α - Al_2O_3) with iron which may occur at a ceramic filter and metallic melt interface. The enthalpy calculation for different structures like FeO, $FeAl_2O_4$, Fe_2AlO_4 and $FeAlO_3$ was done. In the case of Al_2O_3 three phase structures, such as α, κ and γ were considered. Three of the discussed alumina and Fe-alumina structure types are shown in figure 4.1.2. The DFT calculations were done using the WIEN2k Linear Augmented Plane Wave package[141]. The obtained enthalpy of α, κ, γ at T = 0 K is displayed on the right side of the figure 4.2. The calculated bulk modulus - B in GPa unit compare with the data found in the literature are given in the table 4.2 in the case of all considered structures. The slight differences between DFT calculated and experimentally observed values of the bulk modulus may occur respect to the lattices defects, temperature and its microstructure's impurity effects on the other hand, and the type of included exchange-correlation approximation with the help of which is obtained the total energy in the DFT calculations. The calculated properties of the alumina phases are collected in table 4.1. The total energy of κ and γ phases have small differences from the α phase: 0.08 eV and 0.22 eV, respectively. The calculated phase transformation between α, κ and γ occur at negative pressure as shown in on the right hand side of figure 4.2. This condition can be achieved through chemical pressure, for instance, caused by vacancies that stretch the surrounding lattice. Identically, thermal expansion stretches the lattice. The significant effects of thermal motion are, however, not included in the calculations. The experimental comments indicate phase formations on the filter surface. Employing the calculated total energies, the energy differences between several possible phases in their ground state are calculated. This difference is determined by the energy gain from chemical bonding only because thermal effects are not included. The considered reactions are shown in table 4.3. The reactions of Al_2O_3 with Fe are in rows 1 - 2, 8, and with FeO are in rows

3 - 4. The energies are calculated per formula unit of Al_2O_3 to make them comparable. An obtained result is definite that only the reaction of Al_2O_3 with FeO gains energy to produce hercynite with the chemical reaction $Al_2O_3 + 5FeO \leftrightarrow Fe_2AlO_4 + Fe$ or $FeAlO_3$ with $Al_2O_3 + 3FeO \leftrightarrow 2FeAlO_3 + Fe$, even though the $FeAlO_3$ compound crystallises only below the melting point of iron. The justification of the energy gain may be related to the FeO instability. However, as know, FeO is not a component of the melt. Instead, FeO can be considered as an approximation the oxygen dissolution in the iron melt. The most unfavourable one is a reaction of $Al_2O_3 + 5Fe \leftrightarrow 3FeO + 2FeAl$. The conclusion here is that for the formation of hercynite needs extra oxygen from external sources. The replacement of the α phase by the κ or γ metastable alumina phases cause the results of the calculated energies in the reactions to slightly shift. So if the filter surfaces are presented as one of the metastable phases still will be the preferred reaction will still be hercynite.

Although the Al_2O_3 surfaces are highly studied metal oxide, it was considered as an object of this study since it is the main component of the ceramic foam filters. The aim was to control the processes that take place during filtration at the Al_2O_3 surfaces and to obtain a quantitatively qualitative understanding of the nature of interaction with adsorbates due to the filtration process. The calculation of the Al_2O_3 surface energy was done concerning the slab, which got the sufficient thickness of bulk and vacuum after convergence tests. The DFT calculations of surface energy were performed for various Al_2O_3 slabs with different surface orientations and terminations. The calculated results which are given in table 5.1 are in good agreement with literature. The energies of Al_2O_3 (0001) with different terminations and slab thickness (see table 5.5) were studied. In the case of Al1-Al1, Al2-Al2 and O3-O3 the slab composition differs from Al_2O_3 by several Al or O atoms. The approximate adsorption energy was compared to the binding energy of Al_2O_3. For an unrelaxed Al_2O_3 (0001) surface comparison of symmetric - Al, double - Al and unsymmetrical Al - O total energies versus the layer distance is shown on the left side of the figure 5.5. In the same figure's right hand side, the stress for the all cases directed perpendicular to the plane are shown. The energy of the free atom in relation to the PAW pseudopotential (see table 5.6) also was subtracted. It was found that the (0001) plane has the lowest surface energy with a value of 1.5[J/m^2], followed by the $(10\bar{1}0)$ plane with 1.6[J/m^2]. The highest value was found for the $(22\bar{4}3)$ plane for α - Al_2O_3. In conclusion, it appears that none of the quantities correlate to the surface as found in Chapter 5 determine the surface energy alone. A combination of several components is needed. The character of the polyhedra distortions, their density on the surface and the possible relaxation. The elastic modulus seems to be inappropriate because of the high symmetry of the crystal compared to the surface structures.

Awareness of the better interface composition and its energies are essential to the filtration process, where it is critical to control the kinetics, material growth, roughen, stability and dissolution of substances. Due to the application, the strong bonding at the surfaces may be required for ceramic-metal interfaces. Coatings as thermal barriers or corrosion protection are used by the manufacturers, where the lifetime and efficiency are important. Understanding in advance the geometric and electronic properties of the interfaces is vital in advance to get a better coating process and material properties. Therefore DFT calculation of the interface energies of α - Al_2O_3 and Al(111) interface was done. Moreover, the solid - solid state reactions of the formation of interfaces between $MgTiO_3$ (geikielite)/TiO_2 (rutile) and Al_2O_3/TiO_2 (rutile) was studied and described in Chapter 6. The interface energy calculation was done with respect to the slab and bulk calculations via DFT calculation. The α - Al_2O_3/Al(111) interface was studied due to different termination of the α - Al_2O_3 surface (Al and O terminated). Although, the Al-terminated α - Al_2O_3 is considered as a stable structure, in the case of an interface, one can claim that the O-terminated α - Al_2O_3 is favourable for the α - Al_2O_3/Al(111) interface due to the interface energies. The interface energies of α - Al_2O_3/Al(111) interface with different termination are given in table 6.2. The TiO_2 (rutile) with $MgTiO_3$ (geikielite) and α - Al_2O_3 were examined. The studied crystallographic orientations have been found in the literature. The samples under study consisted of corundum, which was coated by rutile and then brought in contact with molten aluminium powder or molten aluminium alloy. In table 6.3, the total energies of the crystallographic orientations from literature can be found. From the samples found in subproject A06 - CRC 920 are presented in table 6.4. The results of the DFT calculated interface energies are in table 6.5, which shows that the observed crystallographic orientations in the samples are more favourable than the ones which are given in the literature. It was even found that one of the crystallographic orientation ($MgTiO_3$ $\{001\}[1\bar{1}0]$ / TiO_2 $\{100\}[001]$) should not take a place.

7.2 Outlook

This dissertation presents some reliable results for the specific heat capacity of Al-Fe binary and Al-Fe-Si ternary phases. For a more broad knowledge base of phase diagram and phase transitions, other systems which were not under investigation of this study should also be considered. However, it is not so straightforward, as it was already mentioned, since Al - Fe phases usually have large unit cells in a formula unit. Therefore, DFT is a very time-consuming calculations from one side, and it cost too much to implement this kind of calculations from the other side. For that reason, the ε - Al_8Fe_5 structure was studied within gamma point.

The fundamental interactions, possible chemical reactions on the filter surfaces, filter surface and interface surface energies were under the interest of this study.

The next aspect of the dissertation is phase formation due to the filtration process. Therefore, the Al_2O_3 - Fe interface has been investigated with respect to the various chemical reactions in their solid state. As reported in Chapter 4 at the Al_2O_3 - Fe interface hercynite Fe_2AlO_4 within solid state chemical reaction most likely formed. Besides, it is shown that only Al_2O_3 with FeO reactions are in an energy gain, which can be reformulated since the formation hercynite needs extra oxygen from external sources. As another aspect, the differences like solid - solid chemical reactions and solid - liquid chemical reactions which take place in the filtration process should also be considered.

The different planes of Al_2O_3 surfaces were modelled as a main substance of the ceramic foam filter material. The main focus was to find the relation between surface energy and other quantities which may lead to an easier and less time - consuming method of calculating the surface energy. As a result, the binding energies of oxygen, alumina, and corundum were considered. However, other methods for determining the binding energy to the surface should be considered, for example, the use of interatomic forces.

Due to the application, the control of the kinetics, material growth and stability is important at ceramic - metal interfaces. The filtration effect depends on interactions at the interface of the ceramic filter material. So a coating may appear as a thermal barrier or corrosion protection. Understanding of the geometric and electronic properties of the interfaces is important to obtaining a better coating process and material properties. The filtration effect depends on interactions at the interface of the ceramic filter material. Interestingly, various ceramic materials show different filtration efficiencies. Although an investigation of the Al_2O_3(0001) /Al(111) interface energy was done for two different terminated Al_2O_3 surface,

it remains a question about the dependence of interface energy versus distance between two substances. This concept was not investigated by this study. The same worries can be expressed for other interface calculations which are presented in Chapter 6.

Bibliography

[1] Giuseppe Grosso and Giuseppe Pastori Parravicini. Chapter 9 - lattice dynamics of crystals. In Giuseppe Grosso and Giuseppe Pastori Parravicini, editors, *Solid State Physics (Second Edition)*, pages 391 – 436. Academic Press, Amsterdam, second edition edition, 2014.

[2] Martin T. Dove. *Structure and Dynamics an atomic view of materials*. Oxford University Press Inc., New York, 2002.

[3] Philip Hofmann. *Solid State Physics: An Introduction*. Wiley-VCH, 2 edition, 2015.

[4] Bo Sundman, Ohnuma Ikuo, Dupin Nathalie, R. Kattner Ursula, and G. Fries Suzana. An assessment of the entire Al–Fe system including {D03} ordering. *Acta Materialia*, 57(10):2896 – 2908, 2009.

[5] Burkhardt U., Grin Yu., Ellner M., and Peters K. Structure refinement of the iron-aluminium phase with the approximate composition Fe_2Al_5. *Acta Crystallographica Section B*, 50(3):313–316, Jun 1994.

[6] Fiz-karlsruhe, inorganic crystal structure database. https://icsd.fiz-karlsruhe.de/.

[7] René Wirnata. An ab-initio study on phphonon and electronic contributions to the heat capacity of Al_5Fe_2. Master's thesis, TU Bergakademie Freiberg, 2014.

[8] F. Stein, S.C. Vogel, M. Eumann, and M. Palm. Determination of the crystal structure of the ε phase in the Fe–Al system by high-temperature neutron diffraction. *Intermetallics*, 18(1):150 – 156, 2010.

[9] Vogel Sven C., Stein Frank, and Palm Martin. Investigation of the ε phase in the Fe–Al system by high-temperature neutron diffraction. *Applied Physics A*, 99(3):607–611, 2010.

[10] Koichi Momma and Fujio Izumi. *VESTA3* for three-dimensional visualization of crystal, volumetric and morphology data. *Journal of Applied Crystallography*, 44(6):1272–1276, Dec 2011.

[11] Nataliya Krendelsberger, Franz Weitzer, Julius Schuster, and Ponte C. On the reaction scheme and liquidus surface in the ternary system Al-Fe-Si. *Metallurgical and Materials Transactions A*, 38(8):1681–1691, 2007.

[12] Amirkhanyan Lilit, Weissbach Torsten, Gruber Thomas, Zienert Tilo, Fabrichnaya Olga, and Kortus Jens. Thermodynamic investigation of the τ_4-Al–Fe–Si intermetallic ternary phase: A density-functional theory study. *Journal of Alloys and Compounds*, 598(0):137 – 141, 2014.

[13] Zienert Tilo, Amirkhanyan Lilit, Seidel Jürgen, Wirnata René, Weissbach Torsten, Gruber Thomas, Fabrichnaya Olga, and Kortus Jens. Heat capacity of η-AlFe (Fe_2Al_5). *Intermetallics*, 77:14 – 22, 2016.

[14] Ji Chi, Zheng Xiang, Rodriguez Sergio Y., Li Yang, Gou Weiping, Goruganti V., Rathnayaka K.D.D., and Ross Joseph H. Dilute magnetism and vibrational entropy in Fe_2Al_5. *Phys. Rev. B*, 82, Nov 2010.

[15] Amirkhanyan Lilit, Weissbach Torsten, Kortus Jens, and Christos G. Aneziris. On the possibility of hercynite formation in a solid state reaction at the Al_2O_3–iron interface: A density-functional theory study. *Ceramics International*, 40(1, Part A):257 – 262, 2014.

[16] Jian-Min Zhang, Dou-Dou Wang, and Ke-Wei Xu. Calculation of the surface energy of hcp metals by using the modified embedded atom method. *Applied Surface Science*, 253(4):2018 – 2024, 2006.

[17] Mohammad Jellur Rahman. Crystal planes and miller indices.

[18] Roman Engel-Herbert, Bharat Jalan, Joël Cagnon, and Susanne Stemmer. Microstructure of epitaxial rutile TiO_2 films grown by molecular beam epitaxy on r-plane Al_2O_3. *Journal of Crystal Growth*, 312(1):149 – 153, 2009.

[19] Lotnyk A., Senz S., and Hesse D. Orientation relationships of $SrTiO_3$ and $MgTiO_3$ thin films grown by vapor-solid reactions on (100) and (110) TiO_2(rutile) single crystals. *The Journal of Physical Chemistry C*, 111(17):6372–6379, 2007.

[20] Wasai K., Mukai K., and Miyanaga A. Observation of inclusion in aluminum deoxidized iron. *ISIJ International*, 42(5):459–466, 2002.

[21] Sebastian Henschel, Dominik Krewerth, Felix Ballani, Anja Weidner, Lutz Krüger, Horst Biermann, Marcus Emmel, and Aneziris Christos G. Effect of filter coating on the quasi-static and cyclic mechanical properties of a $G42CrMo_4$ casting. *Advanced Engineering Materials*, 15(12):1216–1223, 2013.

[22] Shenoy M.M., Kumar R.S., and McDowell D.L. Modeling effects of nonmetallic inclusions on {LCF} in {DS} nickel-base superalloys. *International Journal of Fatigue*, 27(2):113 – 127, 2005.

[23] Ali S., Mutharasan R., and Apelian D. Physical refining of steel melts by filtration. *Metallurgical Transactions B*, (4):725–742, 1985.

[24] T.B. Braun, J.F. Elliott, and M.C. Flemings. The clustering of alumina inclusions. *Metallurgical Transactions B*, 10(2):171–184, 1979.

[25] Roland Kiessling. *Non-Metallic Inclusions in Steel*, volume part III. 1968.

[26] Gauckler, M.M. Waeber, C. Conti, and Jacob-Duliére M. Industrial application of open pore ceramic foam for molten metal filtration. *Light Metals*, 3:251–262, 1985.

[27] Zhang Lifeng and G. Thomas Brian. State of the art in evaluation and control of steel cleanliness. *ISIJ International*, 43(3):271–291, 2003.

[28] Marcus E., Aneziris Christos G., G. Schmidt, D. Krewerth, and Biermann H. Influence of the chemistry of surface functionalized ceramic foam filters on the filtration of alumina inclusions in steel melts. *Advanced Engineering Materials*, 15(12):1188–1196, 2013.

[29] Aneziris Christos G., Dudczig Steffen, Hubálková Jana, Emmel Marcus, and Gert Schmidt. Alumina coatings on carbon bonded alumina nozzles for active filtration of steel melts. *Ceramics International*, 39(3):2835 – 2843, 2013.

[30] Zhang L. and G. Thomas Brian. Inclusions in continous casting steel. *XXIV National Steelmaking Symposium, Morelia*, pages 138–183, Nov 2003.

[31] O. Dávila-Maldonado, A. Adams, L. Oliveira, B. Alquist, and R.D. Morales. Simulation of fluid and inclusions dynamics during filtration operations of ductile iron melts using foam filters. *Metallurgical and Materials Transactions B*, 39(6):818–839, 2008.

[32] Wang H., Shi C.M., Li J., Shi C.B., and Qi Y.F. Evolution of $CaO–MgO–Al_2O_3–CaS–(SiO_2)$ inclusions in h13 die steel during electroslag remelting process. *Ironmaking and Steelmaking*, 0(0):1–11, 0.

[33] R. Ying, Zh. Lifeng, and F. Wen. Effect of addition of al-based slag deoxidizer on $MgO\text{-}Al_2O_3$ inclusions in 3Si-Fe steels. *Metall. Res. Technol.*, 114(1):108, 2017.

[34] BAO Sarina, Tang Kai, Kvithyld Anne, Engh Thorvald, and Tangstad Merete. Wetting of pure aluminium on graphite, SiC and Al_2O_3 in aluminium filtration. *Transactions of Nonferrous Metals Society of China*, 22(8):1930 – 1938, 2012.

[35] Claudia Voigt, Beate Fankhänel, Eva Jäckel, Christos G. Aneziris, Michael Stelter, and Jana Hubálková. Effect of the filter surface chemistry on the filtration of aluminum. *Metallurgical and Materials Transactions B*, 46(2):1066–1072, 2015.

[36] Robert B. Tuttle, Jeffrey D. Smith, and Kent D. Peaslee. Casting simulation of calcium titanate and calcium zirconate nozzles for continuous casting of aluminium-killed steels. *Metallurgical and Materials Transactions B*, 38:101–108, 2007.

[37] Apelian Mutharasan, R. and Chris Diran, Romanowski. A laboratory investigation of aluminum filtration through deep-bed and ceramic open-pore filters. *JOM*, 33(12):12–18, 1981.

[38] Wen Y., Haojian D., Lifeng Zh., and Ying R. Nucleation, growth, and aggregation of alumina inclusions in steel. *JOM*, 65(9):1173–1180, 2013.

[39] Yogeshwar Sahai and Toshihiko Emi. *Tundish Technology For Clean Steel Production*. World Scientific Publishing Company, 2007.

[40] R. Dekkers, B. Blanpain, P. Wollants, F. Haers, C. Vercruyssen, and B. Gommers. Non-metallic inclusions in aluminium killed steels. *Ironmaking & Steelmaking*, 29(6):437–444, 2002.

[41] Duckworth W.E. and Ineson E. The effects of externally introduced alumina particles on the fatigue life of en24 steel. *Clean Steel, Iron Steel Inst. Spec. Rep.*, (77):87–103, 1963.

[42] Somers Arthur V. Karl, Schwartzwalder. Method of making porous ceramic articles. May 1963.

[43] Antsiferov Vladimir N. Foam ceramic filters for molten metals: Reality and prospects. *Powder Metallurgy and Metal Ceramics*, 42(9):474–476, 2003.

[44] U.R. Kattner and B.P. Burton. Al-Fe (aluminum-iron), phase diagrams of binary iron alloys. *ASM International*, pages 12–28, 1993.

[45] Leitner J., Voňka P., Sedmidubský D., and Svoboda P. Application of neumann–kopp rule for the estimation of heat capacity of mixed oxides. *Thermochimica Acta*, 497(1–2):7 – 13, 2010.

[46] Giannozzi Paolo, Baroni Stefano, Bonini Nicola, Calandra Matteo, Car Roberto, Ceresoli Carlo, Cavazzoni ad Davide, L. Chiarotti Guido, Cococcioni Matteo, Dabo Ismaila, Dal Corso Andrea, de Gironcoli Stefano, Fabris Stefano, Fratesi Guido, Gebauer Ralph, Gerstmann Uwe, Christos Gougoussis, Kokalj Anton, Lazzeri Michele, Martin-Samos Layla, Marzari Nicola, Mauri Francesco, Mazzarello Riccardo, Paolini Stefano, Pasquarello Alfredo, Paulatto Lorenzo, Sbraccia Carlo, Scandolo Sandro, Sclauzero Gabriele, P. Seitsonen Ari, Smogunov Alexander, Paolo Umari, and M. Wentzcovitch Renata. Quantum espresso: a modular and open-source software project for quantum simulations of materials. *J. Phys. Condens. Matter*, 21(39):395–502, 2009.

[47] Sundman Bo, Ohnuma Ikuo, Dupin Nathalie, Kattner Ursula R., and Fries Suzana G. An assessment of the entire Al–Fe system including d03 ordering. *Acta Materialia*, 57(10):2896–2908, 2009.

[48] Professor Dr. Dmitriy M. Gitman and Professor Dr. Igor V. Tyutin (auth.). *Quantization of Fields with Constraints*. Springer Series in Nuclear and Particle Physics. Springer-Verlag Berlin Heidelberg, 1 edition, 1990.

[49] Eugen Merzbacher. *Quantum mechanics*. J. Wiley, 3d ed edition, 1998.

[50] Piers Coleman. *Introduction to Many-Body Physics*. Cambridge University Press, 1 edition, 2016.

[51] Kenneth Meyer, Glen Hall, and Dan Offin (auth.). *Introduction to Hamiltonian dynamical systems and the N-body problem*. Applied Mathematical Sciences 90. Springer-Verlag New York, 2 edition, 2009.

[52] Pauli W. Über den zusammenhang des abschlusses der elektronengruppen im atom mit der komplexstruktur der spektren. *Zeitschrift für Physik*, 31(1):765–783, 1925.

[53] W. Heisenberg. Mehrkörperproblem und resonanz in der quantenmechanik. *Zeitschrift für Physik*, 38(6):411–426, 1926.

[54] Dirac P.A.M. On the theory of quantum mechanics. *Proceedings of the Royal Society of London A: Mathematical, Physical and Engineering Sciences*, 112(762):661–677, 1926.

[55] P. A. M. Dirac. Note on exchange phenomena in the thomas atom. *Mathematical Proceedings of the Cambridge Philosophical Society*, 26(3):376–385, 07 1930.

[56] Richard M. Martin. *Electronic Structure: Basic Theory and Practical Methods*, volume Vol. 1. Cambridge University Press, 2004.

[57] Hochstenbach Michiel E. and Sleijpen Gerard L.G. Harmonic and refined rayleigh–ritz for the polynomial eigenvalue problem. *Numerical Linear Algebra with Applications*, 15(1):35–54, 2008.

[58] D.R. Hartree. The wave mechanics of an atom with a non-coulomb central field. part i. theory and methods. *Mathematical Proceedings of the Cambridge Philosophical Society*, 24(1):89–110, 001 1928.

[59] V. Fock. Näherungsmethode zur lösung des quantenmechanischen mehrkörperproblems. *Zeitschrift für Physik*, 61(1):126–148, 1930.

[60] Slater J.C. Note on hartree's method. *Phys. Rev.*, 35:210–211, Jan 1930.

[61] Szabo A. and Ostlund N. *Modern quantum chemistry*. 1989.

[62] Koch W. and Holthausen M.C. *A Chemist's Guide to Density Functional Theory*. 2001.

[63] M. Ya. Amusia, A.Z. Msezane, and V.R. Shaginyan. Density functional theory versus the hartree–fock method: Comparative assessment. *Physica Scripta*, 68(6):C133, 2003.

[64] V.A. Dzuba, V.V. Flambaum, and P.G. Silvestrov. Semiclassical long-range behaviour of hartree-fock orbitals. *Journal of Physics B: Atomic and Molecular Physics*, 15(17):L575, 1982.

[65] P. Hohenberg and W. Kohn. Inhomogeneous electron gas. *Phys. Rev.*, 136:B864–B871, Nov 1964.

[66] Kohn W. and Sham L.J. Self-consistent equations including exchange and correlation effects. *Phys. Rev.*, 140:A1133–A1138, Nov 1965.

[67] Robert G. Parr and Weitao Yang. *Density-functional theory of atoms and molecules*. International series of monographs on chemistry, 16. Oxford, 1989.

[68] R.O. Jones and O. Gunnarsson. The density functional formalism, its applications and prospects. *Rev. Mod. Phys.*, 61:689–746, Jul 1989.

[69] Lévy-Leblond and Jean-Marc. Nonrelativistic particles and wave equations. *Communications in Mathematical Physics*, 6(4):286–311, 1967.

[70] Kohn W. Nobel lecture: Electronic structure of matter—wave functions and density functionals. *Rev. Mod. Phys.*, 71:1253–1266, Oct 1999.

[71] John P. Perdew and Mel Levy. Extrema of the density functional for the energy: Excited states from the ground-state theory. *Phys. Rev. B*, 31:6264–6272, May 1985.

[72] G. Kresse and J. Furthmüller. Efficient iterative schemes for ab initio total-energy calculations using a plane-wave basis set. *Phys. Rev. B*, 54:11169–11186, Oct 1996.

[73] H. Dederichs, P. and R. Zeller. Self-consistency iterations in electronic-structure calculations. *Phys. Rev. B*, 28:5462–5472, Nov 1983.

[74] Akai H. and Dederichs P., H. A simple improved iteration scheme for electronic structure calculations. *Journal of Physics C: Solid State Physics*, 18(12):2455, 1985.

[75] Péter Pulay. Convergence acceleration of iterative sequences. the case of scf iteration. *Chemical Physics Letters*, 73(2):393 – 398, 1980.

[76] Kresse G. and Furthmüller J. Efficiency of ab-initio total energy calculations for metals and semiconductors using a plane-wave basis set. *Computational Materials Science*, 6(1):15 – 50, 1996.

[77] C. Langreth, David and P. Perdew, John. Exchange-correlation energy of a metallic surface: Wave-vector analysis. *Phys. Rev. B*, 15:2884–2901, Mar 1977.

[78] Qingsheng Zhao, C. Morrison, Robert, and G. Parr, Robert. From electron densities to kohn-sham kinetic energies, orbital energies, exchange-correlation potentials, and exchange-correlation energies. *Phys. Rev. A*, 50:2138–2142, Sep 1994.

[79] P. Perdew, John and Yue Wang. Accurate and simple analytic representation of the electron-gas correlation energy. *Phys. Rev. B*, 45:13244–13249, Jun 1992.

[80] J.P. Perdew and A. Zunger. Self-interaction correction to density-functional approximations for many-electron systems. *Phys. Rev. B*, 23:5048–5079, May 1981.

[81] D.M. Ceperley and B.J. Alder. Ground state of the electron gas by a stochastic method. *Phys. Rev. Lett.*, 45:566–569, Aug 1980.

[82] M.C. Payne, M.P. Teter, D.C. Allan, T.A. Arias, and J.D. Joannopoulos. Iterative minimization techniques for ab initio total-energy calculations: molecular dynamics and conjugate gradients. *Rev. Mod. Phys.*, 64:1045–1097, Oct 1992.

[83] A.D. Becke. Density-functional exchange-energy approximation with correct asymptotic behaviour. *Phys. Rev. A*, 38:3098–3100, Sep 1988.

[84] P. Perdew, John, Kieron Burke, and Matthias Ernzerhof. Generalized gradient approximation made simple. *Phys. Rev. Lett.*, 77:3865–3868, Oct 1996.

[85] P. Perdew, John, J.A. Chevary, S.H. Vosko, A. Jackson, Koblar, R. Pederson, Mark, D.J. Singh, and Carlos Fiolhais. Erratum: Atoms, molecules, solids, and surfaces: Applications of the generalized gradient approximation for exchange and correlation. *Phys. Rev. B*, 48:4978–4978, Aug 1993.

[86] Rushton and Peter Philip. Towards a non-local density functional description of exchange and correlation. *Durham University*, Doctoral thesis, 2002.

[87] Conyers Herring. A new method for calculating wave functions in crystals. *Phys. Rev.*, 57:1169–1177, Jun 1940.

[88] I.E. Tamm. Über die quantentheorie der molekularen lichtzerstreuung in festen körpern. *Z. Phys.*, 22:345 – 363, 1930.

[89] Max Born and Kün Huang. *Dynamical theory of crystal lattices*. International series of monographs on physics. Oxford, Clarendon Press, 1954.

[90] Mittal R., Chaplot S.L., and Choudhury N. Modeling of anomalous thermodynamic properties using lattice dynamics and inelastic neutron scattering. *Progress in Materials Science*, 51(2):211 – 286, 2006.

[91] Martin T. Dove. *Introduction to Lattice Dynamics*. Cambridge University Press, 1993.

[92] Debye P. Zur theorie der spezifischen wärmen. *Annalen der Physik*, 344(14):789–839, 1912.

[93] Charles Kittel. *Introduction to Solid State Physics*. Wiley, 8th ed edition, 2005.

[94] Duane C. Wallace. *Thermodynamics of Crystals*. Wiley, 1 edition, 1972.

[95] Rostam Golesorkhtabar, Pasquale Pavone, Jürgen Spitaler, Peter Puschnig, and Claudia Draxl. Elastic: A tool for calculating second-order elastic constants from first principles. *Computer Physics Communications*, 184(8):1861 – 1873, 2013.

[96] Gerhard Sauthoff. *Intermetallics*. Wiley-VCH, 1995.

[97] J. Westbrook and R. Fleischer. *Intermetallic Compounds - Principles and Practice [Vol 3 - Progress]*. Wiley, 2002.

[98] J.H. Westbrook. Intermetallic compounds. *John Wiley & Sons, Inc.*, 1967.

[99] J.H. Westbrook. Intermetallic compounds: Their past and promise. *Metallurgical Transactions A*, 8(9):1327–1360, 1977.

[100] W.J. Keep. Trans aime. *New York, American Institute of Mining, Metallurgical, and Petroleum Engineers*, 18:102, 1980.

[101] K. Natesan and P.F. Tortorelli. Int. symp. on nickel and iron alumintdes: Processing. properties arid application. *ASM International, Materials Park, OH*, page p.249, Oct 1996. Cinciniiati.

[102] D. A. Contreras-Solorio, F. Mejía-Lira, J.L. Morán-López, and J.M. Sanchez. Modeling of the Fe-Al phase diagram. *Phys. Rev. B*, 38:11481–11485, Dec 1988.

[103] Seiersten M. Sintef report stf-28f93051. *Oslo, Norway*, 1993.

[104] W. Gąsior, A. Dębski, and Z. Moser. Formation enthalpy of intermetallic phases from Al–Fe system measured with solution calorimetric method. *Intermetallics*, 24:99 – 105, 2012.

[105] Martin C.J. Marker, Barbara Skolyszewska-Kühberger, Herta S. Effenberger, Clemens Schmetterer, and Klaus W. Richter. Phase equilibria and structural investigations in the system Al–Fe–Si. *Intermetallics*, 19(12):1919 – 1929, 2011.

[106] Schubert Konrad, Rösler Ulrich, Kluge Manfred, Anderko Kurt, and Härle Ludwig. Kristallographische ergebnisse an phasen mit durchdringungsbindung. *Naturwissenschaften*, 40(16):437–437, 1953.

[107] David J. Singh. *Planewaves, Pseudopotentials and the LAPW Method*. Springer US, 1994.

[108] Quantum espresso - homepage and pseudopotential database. http://www.quantum-espresso.org/pseudopotentials/, 2014.

[109] Steve Schmerler. pwtools -. *project homepage*, 09 2014.

[110] Mutuzaki K. Takeda, H.P. The equilibrium diagram of the iron-aluminium-silicon system. *Tetsu to Hagane*, 26:335–361, 1940. in Japanese.

[111] Lichtenberg H. Koerber F., Oelsen W. On the thermochemistry of alloys. ii. direct determination of the heat of formation of ternary alloys of the system iron-nickel-aluminium-silicon, as well as certain alloys of the copper - manganese - aluminium system. *Mitt. K.-W.-Inst. Eisenforschung*, 19:131–159, 1937. Experimental, Thermodyn., 50.

[112] Oelsen W. The heats of formation of binary and ternary alloys and their importance in metallurgical reactions. *Z. Electrochem.*, 43:530–535, 1937. Experimental, Thermodyn., 15.

[113] Sommer F. Vybornov M., Rogl P. The thermodynamic stability and solid solution behavior of the phases τ_5-$Fe_2Al_{7.4}$ and $\tau_6 - Fe_2Al_9Si_2$. *J. Alloys Compd*, 247:154–157, 1997. Crys. Structure, Equi. Diagram, Experimental, Review, 7.

[114] Quivy A. Telolahy P. Legendre B. Li Y., Ochin P. Enthalpy of formation of Al-Fe-Si alloys ($\tau_5, \tau_10, \tau_1, \tau_9$). *J. Alloys Compd.*, 298:198–202, 2000. Experimental, Thermodyn., 20.

[115] Li Y. and Legendre B. Enthalpy of formation of Al-Fe-Si alloys ii ($\tau_6, \tau_2, \tau_3, \tau_8, \tau_4$). *J. Alloys Compd.*, 302:187–191, 2000. Experimental, Thermodyn., 21.

[116] Anglezio J.C., Servant C., and Ansara I. Contribution to the experimental and thermodynamic assessment of the Al-Ca-Fe-Si system - i. Al-Ca-Fe, Al-Ca-Si, Al-Fe-Si and Ca-Fe-Si systems. *Calphad*, 18(3):373–383, 1994. Calculation, Equi. Diagram, Magn. Prop., 18.

[117] Gueneau C., Servant C., and Ansara I. Experimental and thermodynamic assessments of substitutions in the AlFeSi, FeMnSi, FeSiZr and AlCaFeSi systems. *Appl. Thermodyn. Synth. Procee. Mater.*, pages 303–317, 1995. Proc. Symp., Nash, P., Sundman, B. (Eds.), The Minerals, Metals and Materials Society, Warrendale.

[118] Kolby P. System Al-Fe-Si in cost 507, thermochemical database for light metal alloys. *Office for official publications of the European Communities, Luxembourg*, Vol. 2:319–321, 1998. Assessment, Thermodyn.

[119] Liu Z.K. and Chang A. Thermodynamic assessment of the Al-Fe-Si system. *Metall. Mater. Trans. A.*, 30A(7):1081–1095, 1999. Calculation, Thermodyn., 56).

[120] Du Yong, Schuster Julius, Clemens, Liu Zi-Kui, Hu Rongxiang, Nash Philip, Sun Weihua, Zhang Weiwei, Wang Jiong, Zhang Lijun, Tang Chengying, Zhu Zhijun, Liu Shuhong, Ouyang Yifang, Zhang Wenqing, and Krendelsberger Nataliya. A thermodynamic description of the Al–Fe–Si system over the whole composition and temperature ranges via a hybrid approach of CALPHAD and key experiments. *Intermetallics*, 16(4):554 – 570, 2008.

[121] Panday P.K. and Schubert K. Strukturuntersuchungen in einigen mischungen T-B3-B4 (T= Mn,Fe,Co,Ir,Ni,Pd; B3 = Al,Ga,Tl; B4=Si,Ge). *Journal of the Less Common Metals*, 18(3):175 – 202, 1969.

[122] C. Gueneau, C. Servant, F. D'Yvoire, and N. Rodier. $FeAl_3Si_2$. *Acta Crystallographica Section C*, 51(2):177–179, Feb 1995.

[123] G. Kresse and D. Joubert. From ultrasoft pseudopotentials to the projector augmented-wave method. *Phys. Rev. B*, 59:1758–1775, Jan 1999.

[124] John P. Perdew, Kieron Burke, and Matthias Ernzerhof. Generalized gradient approximation made simple. *Phys. Rev. Lett.*, 77:3865–3868, Oct 1996.

[125] Stefano Baroni, Stefano de Gironcoli, Andrea Dal Corso, and Paolo Giannozzi. Phonons and related crystal properties from density-functional perturbation theory. *Rev. Mod. Phys.*, 73:515–562, Jul 2001.

[126] Nolting Wolfgang. *Grundkurs Theoretische Physik*, volume 1-7. Berlin; Heidelberg; New York; Barcelona; Hongkong; London; Mailand; Paris; Tokio : Springer, 2002.

[127] P. Hohenberg and W. Kohn. Inhomogeneous electron gas. *Phys. Rev.*, 136:B864–B871, Nov 1964.

[128] Félix Mouhat and François-Xavier Coudert. Necessary and sufficient elastic stability conditions in various crystal systems. *Phys. Rev. B*, 90:224104, Dec 2014.

[129] A. Reuss. Berechnung der fließgrenze von mischkristallen auf grund der plastizitätsbedingung für einkristalle . *ZAMM - Journal of Applied Mathematics and Mechanics / Zeitschrift für Angewandte Mathematik und Mechanik*, 9(1):49–58, 1929.

[130] A Paesano Jr., C.K Matsuda, J.B.M da Cunha, M.A.Z Vasconcellos, B. Hallouche, and S.L Silva. Synthesis and characterization of Fe-Al_2O_3 composites. *Journal of Magnetism and Magnetic Materials*, 264(2-3):264 – 274, 2003.

[131] Benoist Ollivier, Richard Retoux, Philippe Lacorre, Dominique Massiot, and Gerard Ferey. Crystal structure of κ-alumina: an x-ray powder diffraction, tem and nmr study. *J. Mater. Chem.*, pages 1049–1056, 1997.

[132] Gutiérrez Gonzalo, Taga Adrian, and Johansson Börje. Theoretical structure determination of γ-Al_2O_3. *Phys. Rev. B*, 65:012101, 2001.

[133] Helmer Fjellvrag, Fredrik Gronvold, Svein Stolen, and Bjorn Hauback. On the crystallographic and magnetic structures of nearly stoichiometric iron monoxide. *Journal of Solid State Chemistry*, 124:52 – 57, 1996.

[134] Christos G. Aneziris, Steffen Dudczig, Jana Hubálková, Marcus Emmel, and Gert Schmidt. Alumina coatings on carbon bonded alumina nozzles for active filtration of steel melts. *Ceramics International*, 39(3):2835 – 2843, 2013.

[135] Roderick J. Hill. X-ray powder diffraction profile refinement of sythetic hercynite. *American Mineralogist*, 69:937–942, 1984.

[136] Walsh Aron, Wei Su-Huai, Yan Yanfa, Al-Jassim M.M., Turner John A., Woodhouse Michael, and Parkinson B.A. Structural, magnetic, and electronic properties of the Co-Fe-Al oxide spinel system: Density-functional theory calculations. *Phys. Rev. B*, 76:165119, Oct 2007.

[137] E.J.W. Verwey and E.L. Heilmann. Physical properties and cation arrangement of oxides with spinel structures i. cation arrangement in spinels. *The Journal of Chemical Physics*, 15(4):174–180, 1947.

[138] Bouree F., Baudour J.L., Elbadraoui E., Musso J., Laurent C., and Rousset A. Crystal and magnetic structure of piezoelectric, ferrimagnetic and magnetoelectric aluminium iron oxide $FeAlO_3$ from neutron powder diffraction. *Acta Crystallographica Section B*, 52:217–222, 1996.

[139] Kumar Pradeep, Bera Achintya, Muthu D.V.S., Shirodkar Sharmila N., Saha Rana, Shireen Ajmala, Sundaresan A., Waghmare U.V., Sood A.K., and Rao C.N.R. Coupled phonons, magnetic excitations, and ferroelectricity in $AlFeO_3$:raman and first-principles studies. *Phys. Rev. B*, 85:134449, Apr 2012.

[140] Salah A. Makhlouf, Tetsuya Nakamura, and Masayuki Shiga. Structure and magnetic properties of $FeAl_{1-x}Rh_x$ alloys. *Journal of Magnetism and Magnetic Materials*, 135:257 – 264, 1994.

[141] P. Blaha, K. Schwarz, G.K.H. Madsen, D. Kvasnicka, and J. Luitz. *WIEN2k, An Augmented Plane Wave+Local Orbitals Program for Calculating Crystal Properties*. Technische Universität Wien, Austria, 2001. Version 9.2.

[142] Francis Birch. Finite elastic strain of cubic crystals. *Phys. Rev.*, 71:809–824, 1947.

[143] S.J. Mousavi, M.R. Abolhassani, S.M. Hosseini, and S.A. Sebt. Comparison of electronic and optical properties of the α and κ phases of alumina using density functional theory. *Chinese Journal of Physics*, 47(6):862–873, 2009.

[144] Dubrovinsky Leonid S., Saxena Surendra K., and Lazor Peter. High-pressure and high-temperature in situ X-ray diffraction study of iron and corundum to 68 Gpa using an internally heated diamond anvil cell. *Physics and Chemistry of Minerals*, 25:434–441, 1998.

[145] Bouree F., Baudour J.L., Elbadraoui E., Musso J., Laurent C., and Rousset A. Crystal and magnetic structure of piezoelectric, ferrimagnetic and magnetoelectric aluminium iron oxide $FeAlO_3$ from neutron powder diffraction. *Acta Crystallographica Section B*, 52:217–222, 1996.

[146] Davide Levy, Alessandro Pavese, and Michael Hanfland. Synthetic $MgAl_2O_4$ (spinel) at high-pressure conditions (0.0001–30 Gpa): A synchrotron X-ray powder diffraction study. *American Mineralogist*, 88(1):93–98, 2003.

[147] Wei-Bing Zhang, Yong-He Deng, Yu-Lin Hu, Ke-Li Han, and Bi-Yu Tang. Structural distortion of -structured MnO and FeO. *Solid State Communications*, 142(1–2):6 – 9, 2007.

[148] Ming Liu and Lingun Liu. Bulk moduli of wüstite and periclase: a comparative study. *Physics of the Earth and Planetary Interiors*, 45(3):273 – 279, 1987.

[149] Mathias Ekman, Babak Sadigh, Kristin Einarsdotter, and Peter Blaha. Ab initio study of the martensitic bcc-hcp transformation in iron. *Phys. Rev. B*, 58:5296–5304, Sep 1998.

[150] H. M. Ledbetter and R. P. Reed. Elastic properties of metals and alloys: Iron, Nickel, and Iron-Nickel alloys. *Journal of Physical and Chemical Reference Data*, 2(3):531–618, 1973.

[151] P. Novák, J. Kuneš, L. Chaput, and W.E. Pickett. Exact exchange for correlated electrons. *physica status solidi (b)*, 243(3):563–572, 2006.

[152] P.G. Perkins, D.R. Armstrong, and A. Breeze. On the electronic structure of some metal hexaborides. *Journal of Physics C: Solid State Physics*, 8(21):3558, 1975.

[153] N. Lindulf, M. Halvarsson, H. Nordén, and S. Vuorinen. Microstructural investigation of the $\kappa - Al_2O_3 \leftarrow \alpha - Al_2O_3$ transformation in multilayer coatings of chemically vapour deposited κ-Al_2O_3. *Thin Solid Films*, 253(1):311 – 317, 1994.

[154] Dr. J.K.Goswamy. Physics of crystals.

[155] Peter J. Feibelman. First-principles calculations of stress induced by gas adsorption on Pt(111). *Phys. Rev. B*, 56:2175–2182, Jul 1997.

[156] David Vanderbilt. Absence of large compressive stress on Si(111). *Phys. Rev. Lett.*, 59:1456–1459, Sep 1987.

[157] Robert D. Meade and David Vanderbilt. Origins of stress on elemental and chemisorbed semiconductor surfaces. *Phys. Rev. Lett.*, 63:1404–1407, Sep 1989.

[158] Richard J. Needs. Calculations of the surface stress tensor at aluminum (111) and (110) surfaces. *Phys. Rev. Lett.*, 58:53–56, Jan 1987.

[159] R.J. Needs and M.J. Godfrey. Surface stress of aluminum and jellium. *Phys. Rev. B*, 42:10933–10939, Dec 1990.

[160] M.C. Desjonqueres and D. Spanjaard. *Concepts in Surface Physics*. Springer Series in Surface, 1993.

[161] W. Haiss. Surface stress of clean and adsorbate-covered solids. *Reports on Progress in Physics*, 64(5):591, 2001.

[162] Q. Jiang, H.M. Lu, and M. Zhao. Modelling of surface energies of elemental crystals. *Journal of Physics: Condensed Matter*, 16(4):521, 2004.

[163] Piet Hartman and WG Perdok. On the relations between structure and morphology of crystals. i. *Acta Crystallographica*, 8(1):49–52, 1955.

[164] P Hartman and P Bennema. The attachment energy as a habit controlling factor: I. theoretical considerations. *Journal of Crystal Growth*, 49(1):145–156, 1980.

[165] R.J. Needs and M.J. Godfrey. The origin and possible implications of surface stress on metals. *Physica Scripta*, 1987(T19B):391, 1987.

[166] Yang Liu and Xiao-Shan Ning. Termination, stability and electronic structures of α-Al_2O_3 (0 $\overline{1}$ 1 4) surface: An ab initio study. *Applied Surface Science*, 303(0):210 – 216, 2014.

[167] Wang Junfeng, Xiong Rui, Yin Di, Li Changzhen, Tang Zheng, Wang Ququan, Shi Jing, Wang Yue, and Wen Haihu. Low-temperature specific heat of the quasi-two-dimensional charge-density wave compound KMo_6O_{17}. *Phys. Rev. B*, 73:193102, May 2006.

[168] Wang Xiao-Gang, Chaka Anne, and Scheffler Matthias. Effect of the environment on $\alpha - Al_2O_3$ (0001) surface structures. *Phys. Rev. Lett.*, 84:3650–3653, Apr 2000.

[169] French Roger H. Electronic band structure of Al_2O_3, with comparison to alon and ain. *Journal of the American Ceramic Society*, 73(3):477–489, 3 1990.

[170] Ciraci S. and Batra Inder P. Electronic structure of α-alumina and its defect states. *Phys. Rev. B*, 28:982–992, Jul 1983.

[171] J Toofan and P.R Watson. The termination of the α-Al_2O_3 (0001) surface: a {LEED} crystallography determination. *Surface Science*, 401(2):162 – 172, 1998.

[172] Batyrev Iskander G., Alavi Ali, and Finnis Michael W. Equilibrium and adhesion of nb/sapphire: The effect of oxygen partial pressure. *Phys. Rev. B*, 62:4698–4706, Aug 2000.

[173] C.F. Walters, K.F. McCarty, E.A. Soares, and M.A. Van Hove. The surface structure of α-Al_2O_3 determined by low-energy electron diffraction: aluminum termination and evidence for anomolously large thermal vibrations. *Surface Science*, 464(2–3):L732 – L738, 2000.

[174] Emily A.A. Jarvis and Emily A. Carter. Metallic character of the Al_2O_3(0001)-($\sqrt{31} \times \sqrt{31}$)r $\pm$ 9° surface reconstruction†. *The Journal of Physical Chemistry B*, 105(18):4045–4052, 2001.

[175] Otani M. and O. Sugino. First-principles calculations of charged surfaces and interfaces: A plane-wave nonrepeated slab approach. *Phys. Rev. B*, 73:115407, Mar 2006.

[176] Manassidis Ioannis and Gillan Michael J. Structure and energetics of alumina surfaces calculated from first principles. *Journal of the American Ceramic Society*, 77(2):335–338, 1994.

[177] Donald J. Siegel, Louis G. Hector, and James B. Adams. Adhesion, atomic structure, and bonding at the $Al(111)/\alpha - al_2o_3(0001)$ interface: A first principles study. *Phys. Rev. B*, 65:085415, Feb 2002.

[178] Marmier Arnaud and Parker Stephen C. Ab initio. *Phys. Rev. B*, 69:115409, Mar 2004.

[179] C. Ruberto, Y. Yourdshahyan, and B. I. Lundqvist. Stability of a flexible polar ionic crystal surface: Metastable alumina and one-dimensional surface metallicity. *Phys. Rev. Lett.*, 88:226101, May 2002.

[180] Peter Fratzl, Oliver Penrose, and Joel L. Lebowitz. Modeling of phase separation in alloys with coherent elastic misfit. *Journal of Statistical Physics*, 95(5-6):1429–1503, 6 1999.

[181] Michael Humenik and William D. Kingery. Metal-ceramic interactions: Iii, surface tension and wettability of metal-ceramic systems. *Journal of the American Ceramic Society*, 37(1):18–23, 1954.

[182] Ju V. Naidich. The wettability of solids by liquid metals. *Progress in surface and membrane science*, 14:353–484, 1981.

[183] Jian-Guo Li. Wetting and interfacial bonding of metals with ionocovalent oxides. *Journal of the American Ceramic Society*, 75(11):3118–3126, 1992.

[184] James M. Howe. Bonding, structure and properties of metal/ceramic interfaces. *MRS Proceedings*, 314, 1993.

[185] M.W. Finnis. The theory of metal - ceramic interfaces. *Journal of Physics: Condensed Matter*, 8(32):5811, 1996.

[186] Chen C. A., Korotcov A., Huang Ying-Sheng, Chung W.H., Tsai D.S., and Tiong K.K. Growth and characterization of well-aligned rutile TiO_2 nanocrystals on sapphire substrates via metal organic vapour deposition. *Journal of Materials Science: Materials in Electronics*, 20(1):332–335, 2009.

[187] DL Medlin, KF McCarty, RQ Hwang, SE Guthrie, and MI Baskes. Orientation relationships in heteroepitaxial aluminum films on sapphire. *Thin Solid Films*, 299(1):110–114, 1997.

[188] M Vermeersch, F Malengreau, R Sporken, and R Caudano. The aluminium/sapphire interface formation at high temperature: an aes and leed study. *Surface science*, 323(1-2):175–187, 1995.

[189] David R. Lide. *CRC Handbook of chemistry and physics*. CRC Press, 84th edition, 2003.

[190] G. Dehm, M. Rühle, G. Ding, and R. Raj. Growth and structure of copper thin films deposited on (0001) sapphire by molecular beam epitaxy. *Philosophical Magazine Part B*, 71(6):1111–1124, 1995.

[191] Iskander G. Batyrev and Leonard Kleinman. In-plane relaxation of cu (111) and al (111)/α- Al_2O_3 (0001) interfaces. *Physical Review B*, 64(3):033410, 2001.

[192] Rosa Di Felice and John E. Northrup. Theory of the clean and hydrogenated $al_2o_3(0001) - (1 \times 1)$ surfaces. *Phys. Rev. B*, 60:R16287 – R16290, Dec 1999.

[193] Matsumoto Yuji, Murakami Makoto, Shono Tomoji, Hasegawa Tetsuya, Fukumura Tomoteru, Kawasaki Masashi, Ahmet Parhat, Chikyow Toyohiro, Koshihara Shin-ya, and Koinuma Hideomi. Room-temperature ferromagnetism in transparent transition metal-doped titanium dioxide. *Science*, 291(5505):854–856, 2001.

[194] Zhang Hengzhong and Banfield Jillian F. Understanding polymorphic phase transformation behavior during growth of nanocrystalline aggregates: Insights from TiO_2. *The Journal of Physical Chemistry B*, 104(15):3481–3487, 2000.

[195] David Andeen and F. F. Lange. Crystal chemistry of interfaces formed between two different non-metallic, inorganic structures. *International Journal of Materials Research*, 98(12):1862–5282, 12 2007.

[196] Robert D Shannon. Dielectric polarizabilities of ions in oxides and fluorides. *Journal of Applied physics*, 73(1):348–366, 1993.

[197] Scott A Chambers, Chong M Wang, Suntharampillai Thevuthasan, T Droubay, David E McCready, Alan S Lea, V Shutthanandan, and CF Windisch Jr. Epitaxial growth and properties of mbe-grown ferromagnetic co-doped TiO_2 anatase films on $SrTiO_3(001)$ and $LaAlO_3(001)$. *Thin Solid Films*, 418(2):197–210, 2002.

[198] X. Weng, P. Fisher, M. Skowronski, P.A. Salvador, and O. Maksimov. Structural characterization of TiO_2 films grown on $LaAlO_3$ and $SrTiO_3$ substrates using reactive molecular beam epitaxy. *Journal of Crystal Growth*, 310(3):545–550, 2008.

[199] S.A. Chambers, Y. Gao, S. Thevuthasan, Y. Liang, N.R. Shivaparan, and R.J. Smith. Molecular beam epitaxial growth and characterization of mixed (Ti, Nb) O_2 rutile films on $TiO_2(100)$. *Journal of Vacuum Science & Technology A: Vacuum, Surfaces, and Films*, 14(3):1387–1394, 1996.

[200] P.J. Hansen, V. Vaithyanathan, Y. Wu, T. Mates, S. Heikman, U.K. Mishra, R.A. York, D.G. Schlom, and J.S. Speck. Rutile films grown by molecular beam epitaxy on gan and al ga n/ ga n. *Journal of Vacuum Science & Technology B: Microelectronics and Nanometer Structures Processing, Measurement, and Phenomena*, 23(2):499–506, 2005.

[201] Mikael Schuisky, Anders Hårsta, Aleks Aidla, Kaupo Kukli, Alma-Asta Kiisler, and Jaan Aarik. Atomic layer chemical vapor deposition of tio2 low temperature epitaxy of rutile and anatase. *Journal of the Electrochemical Society*, 147(9):3319–3325, 2000.

[202] J.Y. Huang, B.H. Park, David Jan, X.Q. Pan, Yuntian T. Zhuk, and Q.X. Jia. High-resolution transmission electron microscopy study of defects and interfaces in epitaxial TiO_2 films on sapphire and $LaAlO_3$. *Philosophical Magazine A*, 82(4):735–749, 2002.

[203] Gunnar Eriksson and Arthur D. Pelton. Critical evaluation and optimization of the thermodynamic properties and phase diagrams of the $mno-tio_2$, $mgo-tio_2$, $feo-tio_2$, $ti_2o_3-tio_2$, na_2o-tio_2, and k_2o-tio_2 systems. *Metallurgical Transactions B*, 24(5):795–805, Oct 1993.

[204] Barry A Wechsler and Alexandra Navrotsky. Thermodynamics and structural chemistry of compounds in the system $mgo-tio_2$. *Journal of Solid State Chemistry*, 55(2):165–180, 1984.

[205] LW Coughanour and VA DeProsse. Phase equilibria in the system $mgo-tio_2$. *Journal of Research of the National Bureau of Standards*, 51(2):85, 1953.

[206] Claudia Voigt, Eva Jäckel, Fabio Taina, Tilo Zienert, Anton Salomon, Gotthard Wolf, Aneziris Christos G., and Pierre Le, Brun. Filtration efficiency of functionalized ceramic foam filters for aluminum melt filtration. *Metallurgical and Materials Transactions B*, pages 1–9, 2016.

[207] Vitezslav Stranak, Ann-Pierra Herrendorf, Harm Wulff, Steffen Drache, Martin Cada, Zdenek Hubicka, Milan Tichy, and Rainer Hippler. Deposition of rutile (TiO_2) with preferred orientation by assisted high power impulse magnetron sputtering. *Surface and Coatings Technology*, 222:112 – 117, 2013.

[208] Salomon Anton, Voigt Claudia, Olga Fabrichnaya, Aneziris Christos G., and David Rafaja. Formation of corundum, magnesium titanate, and titanium(iii) oxide at the interface between rutile and molten Al or AlSi7Mg0.6 alloy. *Advanced Engineering Materials*, pages 1700106(1)–1700106(8), 2017. 1700106.

[209] CA Chen, A Korotcov, Ying-Sheng Huang, WH Chung, DS Tsai, and KK Tiong. Growth and characterization of well-aligned rutile TiO_2 nanocrystals on sapphire substrates via metal organic vapour deposition. *Journal of Materials Science: Materials in Electronics*, 20(1):332–335, 2009.

[210] Ruslan P. Liferovich and Roger H. Mitchell. The pyrophanite–geikielite solid-solution series: crystal structures of the Mn1- xMgxTiO$_3$ series (0< x< 0.7). *The Canadian Mineralogist*, 44(5):1099–1107, 2006.

[211] W. Zhang and J. R. Smith. Nonstoichiometric interfaces and al_2O_3 adhesion with al and ag. *Phys. Rev. Lett.*, 85:3225–3228, Oct 2000.

[212] Donald J. Siegel, Louis G. Hector, and James B. Adams. Ab initio. *Phys. Rev. B*, 67:092105, Mar 2003.

[213] Don M. Lipkin, Jacob N. Israelachvili, and David R. Clarke. Estimating the metal-ceramic van der waals adhesion energy. *Philosophical Magazine A*, 76(4):715–728, 1997.

[214] J. Monkhorst, Hendrik and D. Pack, James. Special points for brillouin-zone integrations. *Phys. Rev. B*, 13:5188–5192, Jun 1976.

Appendix A

QUANTUM ESPRESSO settings test

k-points

The Brillouin zone is sampled in reciprocal space set of points (k-space). For all calculations, a automatically generated uniform Monkhorst-Pack grid was used [214]. The greater the number of points for each dimension, i.e. the more dense the grid, the greater the numerical cost, since most of the steps in the program code has to be done for each point.

ecut

It is given for wave functions the kinetic energy cutoff. These wave functions can be expressed by Foueier series in 3D $\sum_k \tilde{u}_{\mathbf{k}} e^{\mathbf{kr}}$ which is built from the basic functions $e^{\mathbf{kr}}$ that represent the travelling plane waves. For a given cutoff, the basis includes only waves with energies less than $E_{cut} = \hbar^2/(2m)|k|^2$.

degauss This setting is needed when calculating metals. It describes the gaussian spreading for the Brillioun zone integration. In other words, it smears out the Fermi level such that more k-points will be on the fermi surface. Smearing is a crucial setting for metals. Without having set this, it is possible, that none of the calculations will converge within a reasonable time or accuracy.

ecutrho is an energy cutoff like ecut, but this parameter to describe the charge density instead of the wave function. Usually, a good guess for its value is four times the ecut parameter, but should be checked regardless of this suggestion.

A.1 Convergence tests for k-points and cutoff

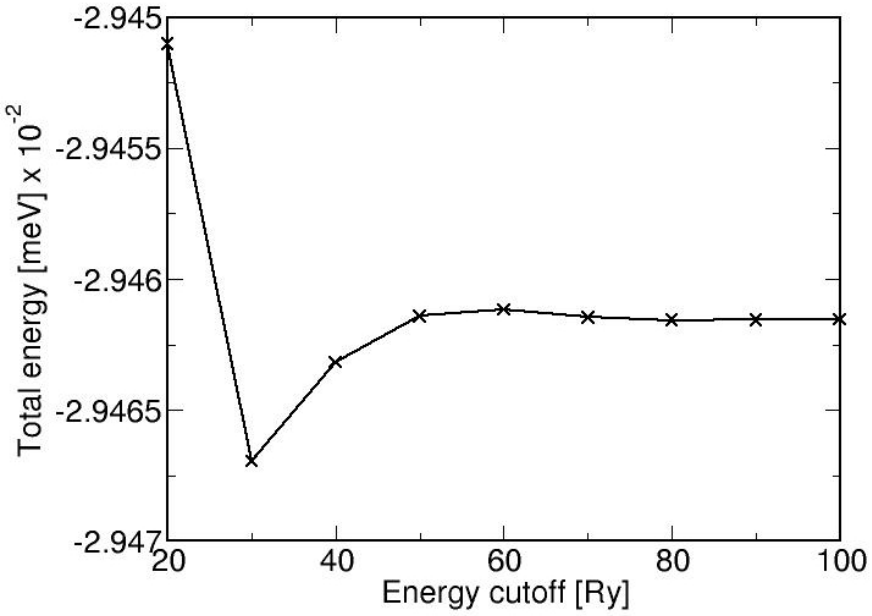

Figure A.1: Convergence test for GGA pseudopotentials **cutoff** for τ_4 - Al_3FeSi_2 structure. As shown in figure convergence achieves at 80 Ry.

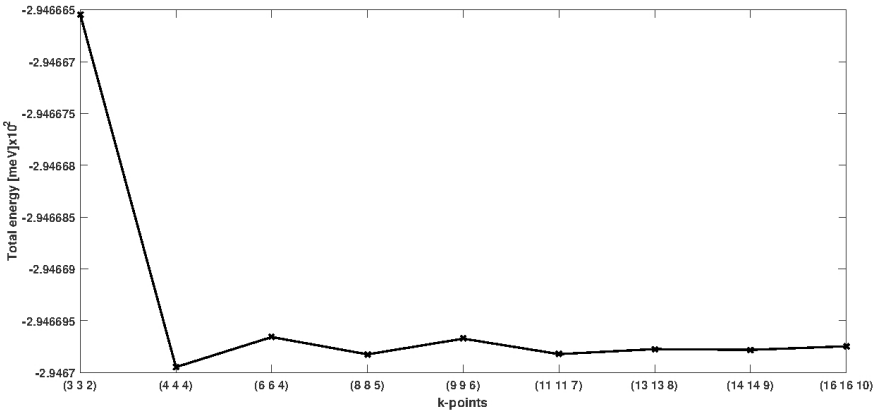

Figure A.2: Convergence test for GGA pseudopotentials **k-points** for τ_4 - Al_3FeSi_2 structure. As shown in figure convergence achieves at $(11 \times 11 \times 7)$.

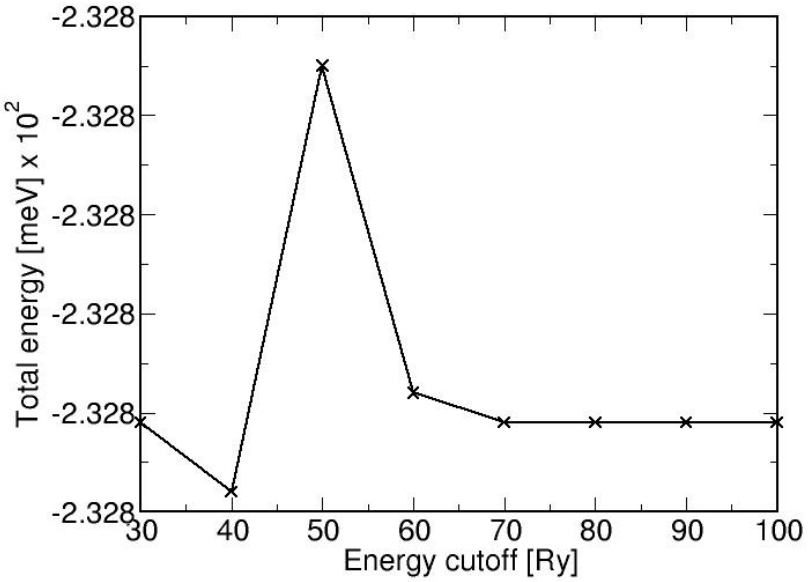

Figure A.3: Convergence test for GGA pseudopotentials **cutoff** for Al_5Fe_2 structure. As shown in figure convergence achieves at 70 Ry.

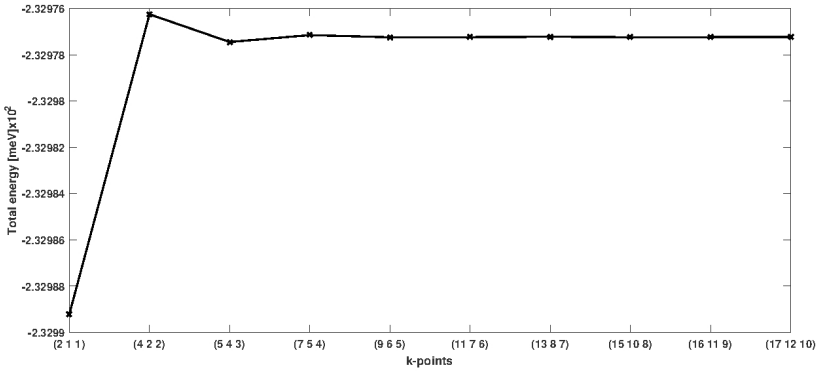

Figure A.4: Convergence test for GGA pseudopotentials **k-points** for Al_5Fe_2 structure. As shown in figure convergence achieves at $(9 \times 6 \times 5)$.

A.2 Convergence tests of slab thickness

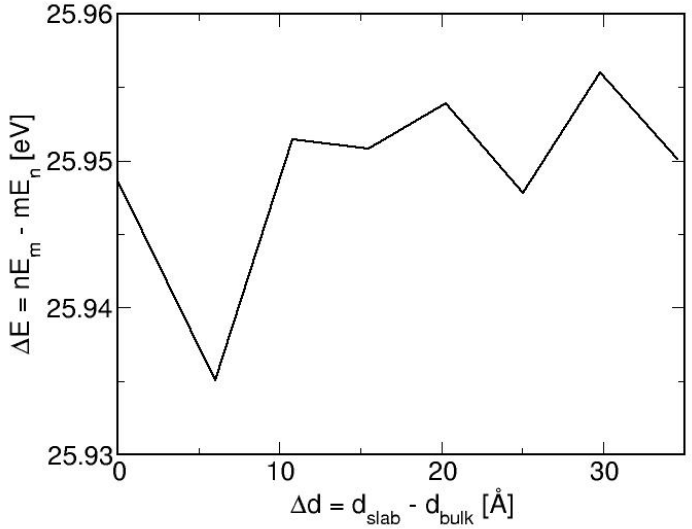

Figure A.5: Convergence tests for the bulk - vacuum thickness in the slab of (0001) plane of the Al_2O_3.

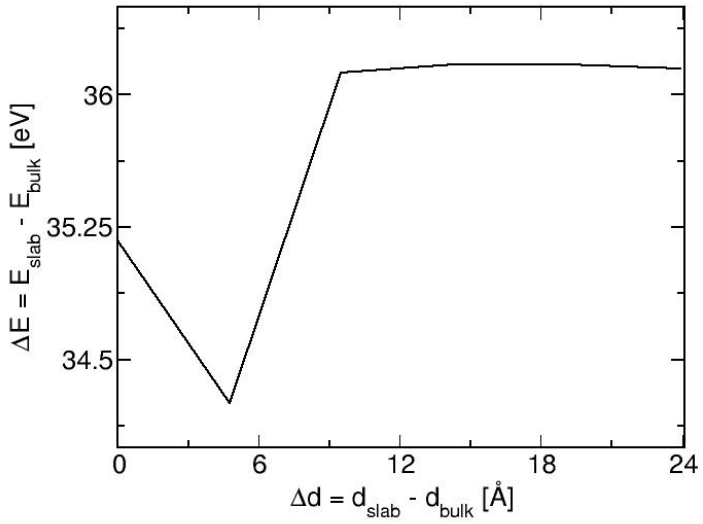

Figure A.6: Convergence tests for the bulk - vacuum thickness in the slab of (11-10) plane of the Al_2O_3.

Appendix B

Input files for a bulk scf calculation

B.1 Al_2O_3 structure input

```
&CONTROL
    calculation  = 'scf',
    restart_mode = 'from_scratch',
    prefix       = 'alpha',
    pseudo_dir   = '/home/amirkhan/QE/pseudo/',
    outdir = '/scratch/amirkhan/alpha'
    disk_io = 'low',
    etot_conv_thr = 1.0E-5,
    tstress = .true.,
    tprnfor = .true.,
    wf_collect = .TRUE.
/
&SYSTEM
    ibrav     = 0
    A         = 1,
    nat       = 30,
    ntyp      = 2,
    ecutwfc   = 90,
    occupations = 'smearing',
    degauss   = 1.0E-5
/
&ELECTRONS
    conv_thr        = 1.0d-9,
/
&IONS
    ion_dynamics    = 'bfgs',
    refold_pos      = .true.
/
&CELL
    cell_dynamics   = 'bfgs',
    press           = 0.0,
/
ATOMIC_SPECIES
    Al  26.982   Al.pbe-n-kjpaw_psl.0.1.UPF
     O  15.999   O.pbe-n-kjpaw_psl.0.1.UPF
ATOMIC_POSITIONS (crystal)
Al      -0.000000038   0.000000221   0.352184559
Al       0.000000038  -0.000000221   0.647815441
Al       0.000000121  -0.000000214   0.147815443
Al      -0.000000121   0.000000214   0.852184557
Al       0.666666866   0.333333326   0.685517714
Al       0.666666576   0.333333247   0.981148601
Al       0.666666646   0.333333239   0.481148599
Al       0.666666793   0.333333322   0.185517715
Al       0.333333424   0.666666753   0.018851399
Al       0.333333134   0.666666674   0.314482286
Al       0.333333207   0.666666678   0.814482285
```

```
Al       0.333333354   0.666666761   0.518851401
O        0.306275663   0.000000028   0.249999988
O        0.693724337  -0.000000028   0.750000012
O        0.000000021   0.306275607   0.250000020
O       -0.000000021   0.693724393   0.749999980
O        0.693724354   0.693724385   0.249999992
O        0.306275646   0.306275615   0.750000008
O        0.972942273   0.333332946   0.583333230
O        0.360391220   0.333332997   0.083333224
O        0.666666990   0.639608728   0.583333230
O        0.666667071   0.027057766   0.083333219
O        0.360391237   0.027057796   0.583333272
O        0.972942227   0.639608729   0.083333295
O        0.639608780   0.666667003   0.916666776
O        0.027057727   0.666667054   0.416666770
O        0.333332929   0.972942234   0.916666781
O        0.333333010   0.360391272   0.416666770
O        0.027057773   0.360391271   0.916666705
O        0.639608763   0.972942204   0.416666728
CELL_PARAMETERS
 4.784703605000 0.000000095616 0.000000008964
-2.392351720000 4.143676511000 0.000000195216
 0.000000023904 0.000000630468 13.05826306000
```

B.2 τ_4 - Al_3FeSi_2 structure input

```
&CONTROL
    calculation = 'vc-relax'
    restart_mode='from_scratch'
    prefix = 'Al3FeSi2'
    tstress = .TRUE.
    tprnfor = .TRUE.
    pseudo_dir = '/pseudo'
    outdir = '/scratch/Al3FeSi2'
/
&SYSTEM
    ibrav= 0
    A=1
    nat=  24
    ntyp= 3
    ecutwfc = 70
/
&ELECTRONS
    conv_thr =  1.0d-8
/
 ATOMIC_SPECIES
 Al  26.981539  Al.pbe-n-kjpaw_psl.0.1.UPF
 Fe  55.845000  Fe.pbe-spn-kjpaw_psl.0.2.1.UPF
 Si  28.085500  Si.pbe-n-kjpaw_psl.0.1.UPF

ATOMIC_POSITIONS (crystal)
Fe       0.000000000   0.012052267   0.250000000
Fe       0.000000000   0.987947733   0.750000000
Fe       0.500000000   0.487947733   0.750000000
Fe       0.500000000   0.512052267   0.250000000
Al       0.000000000   0.000000000   0.000000000
Al       0.500000000   0.500000000   0.500000000
Al       0.000000000   0.000000000   0.500000000
Al       0.500000000   0.500000000   0.000000000
Al       0.139156578   0.631952730   0.864522754
Al       0.860843422   0.368047270   0.135477246
Al       0.360843422   0.868047270   0.364522754
Al       0.639156578   0.131952730   0.635477246
Al       0.860843422   0.631952730   0.635477246
Al       0.139156578   0.368047270   0.364522754
Al       0.639156578   0.868047270   0.135477246
Al       0.360843422   0.131952730   0.864522754
Si       0.163822553   0.672320825   0.154833179
Si       0.836177447   0.327679175   0.845166821
Si       0.336177447   0.827679175   0.654833179
Si       0.663822553   0.172320825   0.345166821
Si       0.836177447   0.672320825   0.345166821
Si       0.163822553   0.327679175   0.654833179
Si       0.663822553   0.827679175   0.845166821
Si       0.336177447   0.172320825   0.154833179

 K_POINTS automatic
  5 5 3 0 0 0

CELL_PARAMETERS
   6.061122507   0.000000000   0.000000000
   0.000000000   6.057894523   0.000000000
   0.000000000   0.000000000   9.465541570
```

Appendix C

Inputs of surface energy, surface charge and interface calculations

C.1 Al_2O_3 [1102] surface structure input

```
&CONTROL
    calculation  = 'scf',
    restart_mode = 'from_scratch'
    prefix       = 'corund1_12'
    pseudo_dir   = '/pseudo'
    outdir = '/scratch/corund1_12'
    disk_io = 'low'
    etot_conv_thr = 1.0E-5
    tstress = .TRUE.
    tprnfor = .TRUE.
/
&SYSTEM
    ibrav     = 0
    A         = 1
    nat       = 150
    ntyp      = 2
    ecutwfc   = 90
    occupations = 'smearing'
    degauss   = 1.0E-5
/
&ELECTRONS
    conv_thr  = 1.0d-9
/
&IONS
    ion_dynamics = 'bfgs',
    refold_pos   = .TRUE.
/
&CELL
    cell_dynamics   = 'bfgs'
    press           = 0.0
/
ATOMIC_SPECIES
    Al  26.982   Al.pbe-n-kjpaw_psl.0.1.UPF
    O  15.999   O.pbe-n-kjpaw_psl.0.1.UPF

ATOMIC_POSITIONS (crystal)
O        0.616508731   0.664658813   0.028490332
O        0.449867861   0.841369109   0.028502290
O        0.116572216   0.841278651   0.028463088
O        0.949934061   0.664206427   0.028435097
O        0.283242331   0.665096676   0.028479975
O        0.783225784   0.840530818   0.028445044
Al       0.891584442  -0.027460419   0.043940099
Al       0.391542966   0.533031920   0.043983380
```

```
Al       0.558207645  -0.026850708   0.043973225
Al       0.058298729   0.532744468   0.043945065
Al       0.224891668  -0.026588797   0.043950602
Al       0.724855257   0.532238672   0.043948867
O        0.654190194   0.199120348   0.062696623
O        0.487485747   0.306664398   0.062764599
O        0.987519803   0.198885814   0.062743900
O        0.154207218   0.306694567   0.062713836
O        0.320825812   0.199699050   0.062757610
O        0.820855890   0.305923973   0.062714894
Al       0.247650633   0.499353985   0.091918800
Al       0.747659868   0.006316940   0.091866741
Al       0.914350706   0.498349773   0.091867013
Al       0.414283546   0.007025484   0.091926192
Al       0.580968433   0.499146142   0.091907996
Al       0.080990361   0.006695577   0.091903640
O        0.533537242   0.848456117   0.109233970
O        0.700165690   0.656993430   0.109210833
O        0.033541426   0.657235754   0.109203833
O        0.200179149   0.848539639   0.109213941
O        0.366820606   0.657640407   0.109247403
O        0.866861452   0.847695031   0.109187393
O        0.753341175   0.156589804   0.157052390
O        0.586674392   0.348346802   0.157077977
O        0.253333017   0.348630979   0.157098130
O        0.086687398   0.157090170   0.157062137
O        0.420009021   0.157165165   0.157104666
O        0.920011180   0.347965441   0.157059452
Al       0.036895441   0.501891195   0.172047472
Al       0.536892344   0.003410357   0.172082006
Al       0.703542915   0.501504235   0.172047103
Al       0.203560525   0.003624316   0.172074169
Al       0.370218757   0.502063562   0.172080957
Al       0.870218026   0.002913690   0.172032054
O        0.797057889   0.696532617   0.199012836
O        0.630392205   0.808073993   0.199041836
O        0.130399109   0.697116273   0.199008174
O        0.297066397   0.808404202   0.199050085
O        0.463739201   0.697059769   0.199048504
O        0.963734521   0.807953706   0.199009655
Al       0.390887236   0.001395693   0.225098296
Al       0.890845964   0.503287995   0.225043164
Al       0.057511119   0.001247537   0.225044921
Al       0.557546357   0.503757048   0.225077742
Al       0.724206687   0.001000662   0.225068299
Al       0.224194028   0.503917894   0.225068879
O        0.674269888   0.347836707   0.238409216
O        0.840919651   0.156430756   0.238403041
O        0.174246854   0.156974452   0.238408319
O        0.340941494   0.348178751   0.238417814
O        0.507603603   0.156928015   0.238443508
O        0.007587293   0.347961794   0.238391263
O        0.896652983   0.654737365   0.289616419
O        0.730013880   0.849143997   0.289630138
O        0.396690214   0.849289843   0.289634614
O        0.230006919   0.655103890   0.289618882
O        0.563362695   0.655078361   0.289633193
O        0.063332080   0.849205249   0.289600901
Al       0.180106228   0.001906138   0.302950889
Al       0.680141062   0.502088710   0.302990825
Al       0.846794704   0.001708059   0.302976137
Al       0.346787570   0.502218897   0.302982226
Al       0.513473491   0.002004911   0.302995667
Al       0.013460907   0.502124508   0.302965161
O        0.940611746   0.195479586   0.329769523
O        0.773931474   0.308169565   0.329821716
O        0.273912793   0.195640430   0.329758149
O        0.440584196   0.308326322   0.329815097
O        0.607268660   0.195664900   0.329816541
O        0.107258727   0.308153452   0.329774895
Al       0.534393173   0.502074351   0.356619622
Al       0.034383783   0.001494932   0.356603232
Al       0.201031270   0.501863973   0.356602937
Al       0.701077048   0.001633605   0.356626226
Al       0.867752830   0.501922706   0.356614924
```

Publikations

[1] C. G. Aneziris, C. Schroeder, U. Fischer, H. Berek, M. Emmel, J. Kortus, L. Amirkhanyan, T. Weißbach. Interactions between exogenous spinel inclusions with endogenous inclusions in a steel melt. *Advanced Engineering Materials*, 15(12):1168 – 1176, 2013.

[2] L. Amirkhanyan, T. Weissbach, J. Kortus, C. G. Aneziris. On the possibility of hercynite formation in a solid state reaction at the Al_2O_3-iron interface: A density-functional theory study. *Ceramics International*, 40(1, Part A):257 – 262, 2014.

[3] L. Amirkhanyan, T. Weissbach, T. Gruber, T. Zienert, O. Fabrichnaya, J. Kortus. Thermodynamic investigation of the τ_4-Al-Fe-Si intermetallic ternary phase: A density-functional theory study. *Journal of Alloys and Compounds*, 598(0):137 – 141, 2014.

[4] T. Zienert, L. Amirkhanyan, J. Seidel, R. Wirnata, T. Weissbach, T. Gruber, O. Fabrichnaya, J. Kortus. Heat capacity of η-AlFe (Fe_2Al_5). *Intermetallics*, 77:14 – 22, 2016.

[5] M. Rudolph, A. Salomon, A. Schmidt, M. Motylenko, T. Zienert, H. Stöcker, C. Himcinschi, L. Amirkhanyan, J. Kortus, Ch. G. Aneziris, D. Rafaja. Thermally induced formation of transition aluminas from boehmite. *Advanced Engineering Materials*, DOI:10.1002/adem.201700141, 2017.

[6] H. Becker, L. Amirkhanyan, J. Kortus, A. Leineweber. Powder-x-ray diffraction analysis of the crystal structure of the η'-Al_8Fe_3 (η'-$Al_{2.67}Fe$) phase. *Journal of Alloys and Compounds*, 721:691 – 696, 2017.

Versicherung

Hiermit versichere ich, dass ich die vorliegende Arbeit ohne unzulässige Hilfe Dritter und ohne Benutzung anderer als der angegebenen Hilfsmittel angefertigt habe; die aus fremden Quellen direkt oder indirekt übernommenen Gedanken sind als solche kenntlich gemacht.

Bei der Auswahl und Auswertung des Materials sowie bei der Herstellung des Manuskripts habe ich Unterstützungsleistungen von folgenden Personen erhalten:

Prof. Dr. Jens Kortus (Betreuer)

Dr. Catherine Alexandrakis (Sprachliches Lektorat)

Weitere Personen waren an der Abfassung der vorliegenden Arbeit nicht beteiligt. Die Hilfe eines Promotionsberaters habe ich nicht in Anspruch genommen. Weitere Personen haben von mir keine geldwerten Leistungen für Arbeiten erhalten, die nicht als solche kenntlich gemacht worden sind.

Die Arbeit wurde bisher weder im Inland noch im Ausland in gleicher oder ähnlicher Form einer anderen Prüfungsbehörde vorgelegt.

Freiberg, 08. August 2017

M.Sc. Lilit Amirkhanyan